EXAMINATION OF LITHIUM-ION BATTERY PERFORMANCE DEGRADATION UNDER DYNAMIC ENVIRONMENT AND EARLY DETECTION OF THERMAL RUNAWAY WITH INTERNAL SENSOR MEASUREMENT

by

Bing Li

A Dissertation

Submitted to the Faculty of Purdue University

In Partial Fulfillment of the Requirements for the degree of

Doctor of Philosophy

School of Aeronautics and Astronautics

West Lafayette, Indiana

December 2020

THE PURDUE UNIVERSITY GRADUATE SCHOOL

STATEMENT OF COMMITTEE APPROVAL

Dr. Vikas Tomar, Chair

School of Aeronautics and Astronautics

Dr. Partha P. Mukherjee

School of Mechanical Engineering

Dr. Kejie Zhao

School of Mechanical Engineering

Dr. Thomas E. Adams

Naval Surface Warfare Center, Crane Division

Dr. Corey T. Love

U.S. Naval Research Laboratory

Approved by:

Dr. Gregory A. Blaisdell

Dedicated to my family and friends.

ACKNOWLEDGMENTS

First of all, I would like to thank Dr. Vikas Tomar for his continuous guidance and support through this research. It has been an honor for me to work in Interfacial Multiphysics Lab as a Ph.D. student. I have always been inspired by Dr. Tomar and the other lab members. Their intelligence and support help me to grow and prosper in the future.

I greatly appreciate the help and encouragement from the fellow graduate students, including the previous lab members who have departure for their brilliant future: Abhijeet Dhiman, Ayotomi Olokun, Casey Jones, Luis Buades, Ayush Rai, Leonardo Fachhini, Nolan Lewis, Tyler Dilliard, Chandra Prakash, Hao Wang, Sudipta Biswas, Yang Zhang, and Devendra Verma. They have been my colleagues, mentors, and friends. It is my pleasure to work with everyone in the lab. The time spent with everyone has made this journey unique and full of memory.

I would like to sincerely thank Dr. Partha P. Mukherjee, Dr. Kejie Zhao, Dr. Thomas E. Adams, and Dr. Corey T. Love to generously serve as my committee members. I have learned more about the research itself thanks to my dedicated committee members. I also appreciate the help from everyone in the Purdue NEPTUNE research team, especially Dr. Vilas G. Pol, Ryan Adams, and Mihit Parekh.

The financial support from the Office of Naval Research under the grant N00014-18-1-2397 (Program Manager: Dr. Michele Anderson) is greatly acknowledged.

I would like to dedicate the last paragraph to my family and friends, including my hamsters. Their understanding, love, and support have always been there for me. This list would go endless and same for my gratefulness to everyone who has helped me in this journey.

TABLE OF CONTENTS

LIST OF TABLES 7
LIST OF FIGURES 8
ABSTRACT 11
1. INTRODUCTION 12
1.1 Operating Principle of Li-ion Batteries 13
1.2 Aging and Capacity Decay Mechanisms of Li-ion Batteries 14
1.3 Heat Generation Mechanism of Li-ion Batteries 14
1.4 Deformation and Stress Accumulation Mechanisms of Li-ion Batteries 15
1.5 Thermal Runaway of Li-ion Batteries 16
1.6 Review on Existing Battery Safety Testing Standards 17
1.7 Research Scope and Outline 20
2. INVESTIGATION OF $LICOO_2$ CATHODE RESPONSE TO DYNAMIC IMPACT USING RAMAN IMAGING BASED ANALYSES 22
2.1 Introduction 23
2.2 Dynamic Testing Setup 24
2.3 Raman Spectroscopy and Scanning Electron Microscopy Analysis 25
2.4 Dynamic Impact Test Result 27
2.5 Results from Raman Spectroscopy and Li-ion Battery Cycling Analysis 28
2.6 Conclusion 31
3. LITHIUM-ION BATTERY THERMAL SAFETY BY EARLY INTERNAL DETECTION, PREDICTION AND PREVENTION 32
3.1 Introduction 33
3.2 RTD Sensor Embedded Li-ion Coin Cell for Electrode Temperature Measurement 34
3.3 External Short Circuit Test and Real-time Electrode Temperature Monitoring 40
3.4 Conclusion 48
4. IN-SITU DETECTION OF ELECTRODE TEMPERATURE DURING OVERCHARGE AND THERMAL RUNWAY OF HIGH CAPACITY POUCH CELLS 49
4.1 Introduction 51
4.2 Fabrication of RTD Embedded Li-ion Pouch Cells 52

4.3 Overcharge Test and Temperature Measurement 56
4.4 Comparison of Battery Surface Temperature and Electrode Temperature 57
4.5 Comparison of Battery Surface Temperature Measured at Different Locations 64
4.6 Conclusion 65
5. SENSOR BASED IN-OPERANDO LITHIUM-ION BATTERY MONITORING IN DYNAMIC SERVICE ENVIRONMENT 67
5.1 Introduction 68
5.2 Design of Dynamic Aging Test 69
5.3 Design of Dynamic Aging Test 76
5.4 Sensor-based Analysis of Li-ion Battery Performance under in-operando Dynamic Loading 80
5.5 Comparison of Sensor Measurement Reliability for Indirect Battery Performance Evaluation 94
5.6 Electrochemical Impedance Spectroscopy Analysis of Li-ion Battery Performance Degradation 95
5.7 Supplementary Tests with the Dynamic Aging Testing Platform and Sensor Network 97
5.8 Conclusion 101
6. FUTURE WORK 104
REFERENCES 105

LIST OF TABLES

Table 1.1. Summary of safety tests proposed in common LIB safety testing standards 18
Table 2.1. Impact depth, velocity and Raman shift summary 26
Table 4.1. Electrode composition and properties..... 54
Table 4.2.Specification of formation cycle and preparation cycle for overcharge test. 55
Table 5.1. Mechanical vibration tests in safety testing standards for Lithium-ion batteries. 70
Table 5.2.Specification of tested Lithium-ion battery. 72
Table 5.3. Mechanical impact tests in Lithium-ion battery safety testing standards. 74
Table 5.4. Summary of proposed dynamic aging testing conditions. 76
Table 5.5. Average cell capacity fading rate over continuous cycling. 79
Table 5.6. Specification of Lithium-ion batteries used in the supplementary tests. 97
Table 5.7. Summary of proposed dynamic aging testing conditions in the supplementary tests. 98
Table 5.8. Comparison of sensor network measurements on cell 3 and cell S3. 101

LIST OF FIGURES

Figure 2.1. (a) Nanomechanical impact loading setup. (b) Schematic of loading cell. (c) Sample clamp and impact condition. (d) LiCoO2 cathode Raman spectrum. (e) Data point position matching. (f) Raman imaging point array. 25

Figure 2.2. SEM image of a pristine $LiCoO_2$ electrode. 26

Figure 2.3. (a) Representative impact depth profile. (b) Representative velocity profile. (c) Impact depth history of 1000 cycles impact test. 27

Figure 2.4. (a) A_{1g} peak relative shift imaging for impacted $LiCoO_2$ electrode (a1: 3; a2: 12; and a3: 1000 impact cycles). (b) Equivalent intrinsic stress released from impact (b1: 3; b2: 12; and b3: 1000 impact cycles). (c) First cycle overpotential. (d) First cycle efficiency. 30

Figure 3.1. (a) Schematic of customized RTD embedded LIB coin cell; (b) RTD embedded PLA spacer and CR2032 cell with internal RTD. Dimension of the RTD embedded spacer was comparable to ordinary CR2032 coin cell spacer, allowing for reliable sensor-electrode contact and cell sealing after assembly. 36

Figure 3.2. (a): Portable battery cycling setup for LIB performance analysis during vibration; (b): LIB short circuit testing and temperature monitoring platform. 38

Figure 3.3. (a) Hot stage temperature measurement with RTD embedded spacers; (b) RTD embedded spacer measurement response rate; (c) RTD embedded spacer measurement response time t_{90}; (d) FTIR spectra for electrolyte stability testing; (e) Comparison of charge/discharge curves for sensor embedded cell over vibration; (f) Electrochemical impedance spectroscopy of the constructed cells at OCV (3.1 V vs Li/Li+) with RTD. 39

Figure 3.4. (a) Temperature measurements with internal RTD, external RTD and infrared camera in the short circuit test; (b) Maximum temperature rise detected by internal and external RTDs; (c) RTD detection time $t_{90,\,int}$ and $t_{90,\,ext}$ of internal and external RTDs; (d) Detection time ratio texttint; (e): SEM image of LCO cathode before short circuit test and (f): after short circuit test. 42

Figure 3.5. (a): Two phases of heat transfer in battery short circuit test; (b): Representative comparison of temperature model predictions; (c): Peak temperature prediction error comparison; (d): Peak temperature prediction error ratio; (e): Relation between cathode mass, peak internal temperature and maximum battery surface temperature rising rate 45

Figure 3.6. Strategy for protecting coin cell against short circuit related thermal runaway. 47

Figure 4.1. (a). Pouch cell electrode pack and RTD embedded substrate; (b). Assembly condition of electrode pack and RTD embedded substrate; (c). The layout of RTD embedded pouch cell and (d). Overcharge and temperature measurement system setup. 53

Figure 4.2. Performance of cell #1 and cell #2 in (a): Formation cycle 1; (b): Formation cycle 2; (c): Formation cycle 3 and (d): Preparation cycle for overcharge test. 55

Figure 4.3. External thermocouple and RTD reading Comparison. (a-c): Cell #1 and (d): Cell #2. 56

Figure 4.4. Cell #1: (a). Initiation of explosion: cell leaked and emitted sparks, (b). Development of explosion: sparks and smoke released from the cell, (c). Lateral stage of explosion: continuous smoking. Cell #2: (d). Initiation of explosion: cell leaked and jetted flames, (e). Development of explosion: jet flame developed, (f): Lateral stage of explosion: continuous burning. 57

Figure 4.5. Temperature and voltage of cell #1 during (a). 1C rate overcharge up to 5.4 V, (b). 5C rate overcharge and (c). 5C rate overcharge before thermal runaway event. Temperature changing rate of cell #1 during (d). 1C rate overcharge up to 5.4 V, (e). 5C rate overcharge, and (f). 5C rate overcharge before the thermal runaway event. Comparison of battery surface and electrode temperature during: (g). 1C rate overcharge up to 5.4 V and (h). 5C rate overcharge until the thermal runaway event (V= 1.14 V and 1.18 V: after thermal runaway). 58

Figure 4.6. (a). Battery temperature and voltage of cell #2 under 5C rate charge until explosion, (b). Temperature changing rate of cell #2, and (c). Comparison of surface and electrode temperature of cell #2. 62

Figure 4.7. Voltage and battery surface temperature measured at the battery center and the tab during: (a). 1C rate overcharge of cell #1 up to 5.4 V; (b). 5C rate overcharge of cell #1; (c). 5C rate overcharge of cell #1 before the explosion; (d). 5C rate overcharge of cell #2 until the explosion. 64

Figure 5.1. In-operando testing platform for LIBs, (a): Setup for in-operando vibration test, and (b): Setup for in-operando impact test analysis. 73

Figure 5.2. (a): Capacity of 2-cell pack (cell 1 and 2) under in-service vibration and impact; (b): Capacity of single cell (cell 3) under in-service vibration and impact; (c): Capacity comparison of single cell under different dynamic conditions; (d): Internal resistance of LIBs under in-service vibration and impact; (e): Incremental capacity of cell 3 in cycle 1-100; (f) Peak incremental capacity of cell 3 in cycle 1-100; (g) Incremental capacity of cell 3 in cycle 101-200; (h) Peak incremental capacity of cell 3 in cycle 101-200. 77

Figure 5.3. Voltage, temperature, temperature changing rate, deformation and cell balance parameter I_1/I_2 in two consecutive cycles of (a): 2-cell pack (cell 1 and 2), (b): single cell (cell 3). 82

Figure 5.4. Relation between maximum temperature increase and capacity of (a): cell 1, (b): cell 2 and (c): cell 3. (d): Relation between maximum deformation and capacity of cell 3. 86

Figure 5.5. SEM images of graphite electrode (a1-a4, b1-b4 and c1-c4) and LCO electrode (d1-d4, e1-e4 and f1-f4). (a1-a4 and d1-d4): electrodes from fresh LIB; (b1-b4 and e1-e4): electrodes from LIB after 500 cycles with no vibration (cell 5); (c1-c4 and f1-f4): electrodes from LIB after 500 cycles with vibration and impact (cell 3). Imaging orientation: (a1-f1): 45º, (a2-f2): 90º, (a3-f3 and a4-f4): 0º. 90

Figure 5.6. (a1) G band Raman shift contour of pristine graphite electrode, (a2): D, G band intensity ratio (I_D/I_G) contour of pristine graphite electrode, (a3): representative Raman spectrum of pristine graphite electrode; (b1): G band Raman shift contour of aged graphite electrode, (b2): D, G band intensity ratio (I_D/I_G) contour of aged graphite electrode, (b3): representative Raman spectrum of aged graphite electrode, (c1) A_{1g} band Raman shift contour of pristine LCO electrode, (c2) E_g band Raman shift contour of pristine LCO electrode, (c3): representative Raman spectrum

of pristine LCO electrode; (d1): A_{1g} band Raman shift contour of aged LCO electrode, (d2) E_g band Raman shift contour of pristine LCO electrode, (d3): representative Raman spectrum of aged LCO electrode. 93

Figure 5.7. Comparison of information divergence obtained with battery deformation and peak temperature for capacity fade detection. 95

Figure 5.8. Comparison of electrochemical impedance spectra of lithium ion batteries before and after 500 cycles, (a): cell 1, (b): cell 2, (c): cell 3, (d): cell 4, (e): cell 5. 96

Figure 5.9. (a): Capacity of a two-cell pack (cell S1 and S2) under in-service vibration and impact; (b): Capacity of a single cell (cell S3) under in-service vibration and impact. 99

Figure 5.10. Voltage, temperature, temperature changing rate, deformation and cell balance parameter (I_1/I_2) in two consecutive cycles of (a): 2-cell pack (cell S1 and S2), (b): single cell (cell S3). 99

Figure 5.11. Relation between maximum temperature increase and capacity of (a): cell S1, (b): cell S2 and (c): cell S3. (d): Relation between maximum deformation and capacity of cell S3. 100

Figure 5.12. Comparison of electrochemical impedance spectra of lithium ion batteries in supplementary test before and after 200 cycles, (a): cell S1, (b): cell S2, (c): cell S3. 100

ABSTRACT

Performance degradation of lithium-ion batteries (LIBs) from in-service abuse was analyzed using novel dynamic abuse tests and sensor-based in-situ monitoring of battery state of health (SOH). The relation between dynamic impact and structure changes of $LiCoO_2$ (LCO) electrode was analyzed through a nano-impact test directly applied to the electrode and Raman imaging. After the electrode structure damage induced by the dynamic loading was analyzed, the performance of the LIBs with the abused electrodes was evaluated to establish the relation between the number of impact cycles and LIB performance degradation. The mechanism of impact related LIB capacity decrease was analyzed, and the capacity change can be predicted based on the impact abuse history using this approach. In order to provide more detailed information on the battery performance degradation caused by the in-service dynamic loads, a dynamic aging testing platform was designed to simulate in-service vibration and impact experienced by the LIBs. Based on the lessons learned, a sensor network was constructed to provide a comprehensive in-situ evaluation of the SOH of commercial batteries. Mechanisms of LIB capacity fade, temperature increase, and cell deformation from cycling in representative dynamic environments were analyzed and correlated with theoretical predictions. Difference between the aging of a battery pack and that of a single cell was also investigated, which presented the influence of current imbalance on the SOH decay of battery packs. SEM imaging, Raman imaging, and electrochemical impedance spectroscopy (EIS) analysis were also applied to support the sensor network measurements.

In order to provide an early detection of catastrophic LIB failure such as thermal runaway, an internal resistance temperature detector (RTD) based electrode temperature monitoring approach was developed. By embedding the RTD into LIBs with 3D printing technique, electrode temperature can be collected during ordinary cycling and electrical abuse of LIBs, such as external short circuit and overcharge. The internal RTD presented high measuring efficiency, while there was no interference between the sensor measurement and battery operation. The internal RTD detected the short circuit event and overcharge failure prior of time: the efficiency of the internal RTD was 6-10 times higher than the external RTD in the short circuit test. This provided the chance for early detection and prevention of catastrophic LIB failures. Besides, with the detailed information on electrode temperature evolution during LIB thermal runaway available, the internal RTD also provided the chance to enhance the understanding of the thermal runaway mechanism.

1. INTRODUCTION

Due to the high capacity and efficiency, lithium-ion batteries (LIBs) have a profound impact on the modern industry and they are applied extensively in aircraft, electric vehicles, portable electronic devices, robotics, etc. (J. Lee et al., 2014; C.-Y. Wang et al., 2016; H. Wu, Zhuo, Kong, & Cui, 2014). The growing market has encouraged LIB related research in both industry and academia, and the LIB manufacturing technique has been advancing rapidly. Between 2010 and 2016 the average price of LIBs dropped from ~$1000 /KWh to $273/KWh with an annual decreasing rate of 19% (Amatucci, Tarascon, & Klein, 1996). Besides, the safety of LIBs has been improved with the application of numerous safety devices, including safety vents, special coatings, electrolyte additives, or shut-off separators (Balakrishnan, Ramesh, & Kumar, 2006). With the continuous improvement in LIB manufacturing and safety management, the field of application for LIBs has expanded beyond small electronic devices. The installed LIB manufacturing capacity for electric vehicle was 103 GWh in 2017 and was predicted to reach 400-500 GWh in 2025 (Amatucci et al., 1996). LIBs are also seeing application in commercial aircrafts such as Boeing 787 (Kolly, Panagiotou, & Czech, 2013). Although different applications have posed different requirements on LIBs, the desire on improving the performance, reliability, and safety is common for all LIB users.

Unfortunately, despite continuous efforts on improving the LIB performance, reliability, and safety, unexpected LIB failures and accidents have been reported for years. Numerous devices were involved in those LIB safety accidents, including mobile phones (Birkl, Roberts, McTurk, Bruce, & Howey, 2017), e-cigarettes (Hong, Maleki, Al Hallaj, Redey, & Selman, 1998), electric vehicles (Kumai, Miyashiro, Kobayashi, Takei, & Ishikawa, 1999), and aircraft (Nicholas Williard, He, Hendricks, & Pecht, 2013). These battery accidents cause severe property damage, personal injury, and sometimes even fatality. As a result, it is vital to improve the reliability and safety of LIBs, understand the mechanism of catastrophic LIB failures, and find a feasible solution for in-situ LIB failure monitoring and prevention.

The reason for LIBs being prone to failure can be roughly sorted into three aspects: (1) the high energy density of LIBs. Energy storage devices with high energy density are generally considered “dangerous”, especially in their charged state (Viswanathan et al., 2010). (2) The complex service environment. Dynamic vibration and impact during service and transportation are

inevitable for LIBs, which can damage electrodes and other battery structures (B. Li et al., 2018). (3) The chain reaction known as thermal runaway. Once the heat generation in LIB pushed the temperature above the threshold of thermal runaway, it is impossible for the heat generating reactions to stop spontaneously (Q. Wang et al., 2012). Thus, in order to improve LIB safety effectively, three steps should be taken correspondingly: (1) analyze the capacity change in LIBs over its entire service life and understand the capacity degradation mechanism; (2) investigate the effects of dynamic loading on LIB structure and its capacity; (3) improve the thermal runaway monitoring technique and provide an effective in-situ electrode temperature monitoring technique. This dissertation focuses on these three aspects and aims to provide a practical solution for LIB performance management as well as failure detection and prevention.

1.1 Operating Principle of Li-ion Batteries

A typical LIB consists of the anode, cathode, separator, electrolyte, and battery case. When LIBs are being charged or discharged, they operate by the transfer of Li ions between the cathode and anode. The electrodes are lithium-intercalation compounds, providing accommodation for Li-ions. The separator is a thin polymer substrate, which prevents the internal short circuit between the cathode and anode. The electrolyte promotes the movements of Li ions between the electrodes in charge and discharge.

There are numerous materials for LIB anode and cathode, including lithium metal and graphite (anode material) as well as $LiCoO_2$ (LCO), $LiNi_xMn_yCo_zO_2$ (NMC) and $LiFePO_4$ (LFP) (cathode material), etc. Despite the difference in electrode materials, the principle of operation remains the same: in the charging process the Li ions are deintercalated from the cathode, where the oxidization reaction happens. The Li ions then transfer through the separator and reach the anode, where they are reduced. For LIBs with graphite anode, the Li ions would be intercalated into the graphite lattice, resulting in a lithiated compound Li_xC_6. For a LCO- graphite LIB, the electrode reactions and the full cell reaction can be written as (Forgez, Do, Friedrich, Morcrette, & Delacourt, 2010):

$$\text{Cathode: } LiCoO_2 - xe^- \rightarrow Li_{1-x}CoO_2 + xLi^+ \tag{1.1}$$

$$\text{Anode: } C_6 + xLi^+ + xe^- \rightarrow Li_xC_6 \tag{1.2}$$

$$\text{Full cell: } LiCoO_2 + C_6 \xrightarrow{\text{charge}} Li_xC_6 + Li_{1-x}CoO_2 \tag{1.3}$$

LCO has a theoretical specific energy density of 274 mAh/g (Thomas & Newman, 2003). However, when the value of x reaches 0.5 in $Li_{1-x}CoO_2$, additional extraction of Li ions would cause structural instability of LCO, which is unsafe for battery operation (Amatucci et al., 1996). This limits the specific energy density of LCO as ~140 mAh/g, and the cut-off voltage for the charging of a LCO- graphite cell should not exceed 4.2 V (Y. J. Kim, Cho, Kim, & Park, 2003). This defines the operating voltage range for LCO- graphite cells as 3.0 V- 4.2 V and the nominal voltage of a LCO- graphite cell is approximately 3.7 V.

1.2 Aging and Capacity Decay Mechanisms of Li-ion Batteries

The aging and capacity decay of LIBs is mostly contributed to the loss of lithium inventory, which can come from the formation of solid electrolyte interface (SEI), lithium plating, electrode structural disorder, oxidization of conductive particles, binder decomposition, and loss of contact between electrode particles and binder, micro level cracking in electrodes, etc. Some other factors that can also contribute to the LIB capacity decay, which includes changes in the cell impedance, electrolyte decomposition, gas generation, corrosion of current collector, etc. (Hausbrand et al., 2015). For LIBs operating within the 3.0- 4.2 V range, it is rare to see electrolyte decomposition, gas generation, or corrosion of current collector, as they typically require overcharge or overdischarge condition (Guo, Lu, Ouyang, & Feng, 2016; Kumai et al., 1999). Thus, the aging and capacity change of LIBs under well-defined operating conditions can be evaluated with the analysis of available lithium inventory, electrode surface film formation, contact condition between electrode particles, and electrochemical impedance of the cells.

1.3 Heat Generation Mechanism of Li-ion Batteries

The heat generated during the operation and abuse of LIBs is the key factor that affects the thermal safety of LIBs. One major reason for LIB failure and explosion is the abnormal increase in the battery temperature. A simple equation for description of LIB temperature evolution can be written as:

$$\dot{q} = -hA(T_s - T_e) + MC\frac{dT}{dt} \tag{1.4}$$

where $\dot{q}$ is the rate of heat generation, A is the battery surface area, h is the heat convection/ heat transfer coefficient, T_s is the battery surface temperature, T_e is the environment surrounding

temperature, M is the battery mass, C is the average specific heat capacity and T is the average battery temperature. It can be found with equation (1.4) that when too much heat is generated in a LIB and cannot be dissipated effectively, the temperature of the LIB will rise rapidly. This can further promote the heat generation within the LIB, which often leads to a catastrophic result known as thermal runaway (Feng et al., 2018). Thus, it is essential to understand the heat generation mechanism in LIBs for the prevention of thermal failure.

Heat generation in LIBs can be sorted into two parts: reversible heat generation and irreversible heat generation. The irreversible heat generation in LIBs is mainly contributed to the ohmic heat generation, which is related to the overpotential of the cell (Viswanathan et al., 2010). The reversible heat generation is mostly related to the change in LIB entropy (Hong et al., 1998). It should be pointed out that there is also heat generated from the side reactions and mixing process within the LIBs (G. Liu, Ouyang, Lu, Li, & Han, 2014). However, the LIB aging process is relatively slow in most engineering applications, which represents a limited side reaction rate in the charge- discharge cycles (Forgez et al., 2010). The heat in the mixing process is related to the formation and relaxation of cell concentration gradients, which is not significant under constant current cycling (Thomas & Newman, 2003). Thus for LIBs under constant current cycling mode with moderate rates, their heat generation can be described as:

$$\dot{q} = I(U_{OCV} - U_t) - IT\frac{\partial U_{OCV}}{\partial T} \tag{1.5}$$

where I is the cycling current, U_{OCV} is the open circuit voltage, U_t is the terminal voltage and $T\frac{\partial U_{OCV}}{\partial T}$ is the effective entropic potential. The term $I(U_{OCV}-U_t)$ is the ohmic heat generation term (irreversible) and the term $IT\frac{\partial U_{OCV}}{\partial T}$ is the entropic heat generation term (reversible).

1.4 Deformation and Stress Accumulation Mechanisms of Li-ion Batteries

Another typical reason for LIB failure is the deformation and stress accumulation from charge- discharge cycles. For LIBs in the field applications, especially those in battery packs with large amount of cells, the cells are generally clamped in a battery holder. During the charging of LIBs, the insertion of Li ions into the graphite anode can generate approximately 10% change in the interlayer distance of graphite (Boulet-Roblin et al., 2016). After taking the volume of lithium into account, a total volume expansion of 13.2% was observed when C_6 is fully lithiated into the

compound of LiC_6 (Schweidler et al., 2018). Stress accumulation within the LIBs should be expected if they are tightly clamped or if there is no space within the battery case to accommodate the electrode volume change. When the stress level is too high, the electrode particles may penetrate the separator, causing internal short circuit and explosion of the battery. The unreasonably small battery case has been identified as one of the reasons for the safety accidents related with Samsung Galaxy Note 7 mobile phones (Duh, Lin, & Kao, 2018).

Although the lithium content in the anode has a linear relation with its state of charge (SOC), stress accumulation within the LIBs does not happen at a constant rate. A nonlinear relation between the total volume change of graphite anodes and its SOC has been observed (Schweidler et al., 2018). Thus, it is necessary to monitor the stress accumulation within the LIBs during their operation. However, this task is challenging due to the complex battery structure and electrochemical reactions involved in the battery operation. As an alternative approach, the deformation of a LIB that is free to deform can be used to estimate the stress accumulation within the battery when it is clamped.

Other factors related to the volume change of LIBs include gas generation (S. S. Zhang, 2014) and SEI formation (Ploehn, Ramadass, & White, 2004). The key difference between these types of deformation is that deformation from gas generation and SEI formation is nonreversible. Thus, although the amount of deformation caused by gas generation and SEI formation is generally limited, they should also be investigated for the prevention of LIB explosion.

1.5 Thermal Runaway of Li-ion Batteries

One common and life-threatening failure mode of LIBs is the thermal runaway, where the abnormal temperature increase changes the rate and type of electrochemical reactions in LIBs, which further promotes the temperature increase. This process is a type of uncontrolled positive feedback and typically leads to destructive failures of LIBs.

The process of LIB thermal runaway is complex and there are numerous reactions involved. These include SEI decomposition, the reactions between the anode and the electrolyte, electrolyte decomposition and gas generation, separator melting, internal short circuit, electrolyte burning, etc. Some of these processes are related to the others. For instance, assume the main composition of the SEI is $(CH_2OCO_2Li)_2$, then one of the SEI decomposition reactions can be described as (H. Yang, Bang, Amine, & Prakash, 2004):

$$(CH_2OCO_2Li)_2 \rightarrow LI_2CO_3 + C_2H_4 + CO_2 + 0.5O_2 \quad (1.6)$$

where gas generation is involved in the decomposition of SEI. Despite the complex nature of LIB thermal runaway process, SEI decomposition is typically the first reaction in the chain. The onset temperature for SEI decomposition has been reported to be around 80-85 ℃ (Spotnitz & Franklin, 2003, Rodrigues, Sayed, Gullapalli, & Ajayan, 2018) in literature. Thus it is practical to use LIB temperature as an indicator for the detection of thermal runaway.

1.6 Review on Existing Battery Safety Testing Standards

There are numerous battery safety testing standards that are available for users to choose from based on their applications. Despite the different focuses of those standards, the main purpose of the LIB safety tests can be summarized as: (1) to evaluate the performance degradation of LIBs under different abusing conditions and (2) to examine the risk of catastrophic LIB failure such as thermal runaway and explosion under the abuse. In general, the abusing conditions proposed in LIB safety testing standards can be categorized into three groups: (1) mechanical and dynamical abuse, such as impact and vibration; (2) thermal abuse, such as high temperature storage and cycling; and (3) electrical abuse, such as short circuit and overcharge. A summary of the tests proposed in several commonly used LIB safety testing standards and corresponding testing conditions is provided in Table 1.1 (Doughty, 2010; Europe, 2015; Naval Ordnance Safety and Security Activity, 2010).

Table 1.1. Summary of safety tests proposed in representative LIB safety testing standards.

Category	Test	Testing condition		
		UN 38.3	NAVSEA 9310	SAE J2646
Mechanical / dynamical abuse	Vibration	Sinusoidal vibration, frequency: 7-200 Hz, acceleration: 1-8 g	Sinusoidal vibration, frequency: 7-200 Hz, acceleration: 1-8 g	-
	Impact	Half sinusoidal wave, 6ms duration with 150 g duration	Half sinusoidal wave, 6ms duration with 150 g duration	Half sinusoidal wave, 6ms duration with 150 g duration
	Drop	-	-	Drop from 2 m
	Penetration	-	-	Penetrate through the cell with 8 cm/s velocity using a rod with 3 mm diameter
	Roll-over	-	-	Roll over the pack in slow rolling for 1 min
	Crush	Crush between flat surfaces with initial speed of 1.5 cm/s	Crush between flat surfaces with initial speed of 1.5 cm/s	Crush to 85% of initial dimension, hold for 5mins and crush to 50% of initial dimension
Thermal abuse	High temperature storage	-	Heat with rate of 10 °C/min up to 500 °C, maintain for 1 hour	Heat to 900 °C by radiant heating and hold for 10 mins
	Thermal shock/ cycling	-	-	Heat with 5 °C/min, until reaching 300 °C above the cell operating temperature
	Cycling without thermal management unit	-	-	Cycle at normal operating temp, complete 20 cycles
Electrical abuse	External short circuit	Short circuit with ≤0.1 Ω circuit, last for at least 1 hour after external temperature returns to 55±2°C	Short circuit with ≤0.02 Ω circuit, last for at least 24 hours	Hard short: ≤0.005 Ω, soft short: ≈ cell DC resistance, last for 1 hour

Table 1.1. continued.

Category	Test	Testing condition		
		UN 38.3	NAVSEA 9310	SAE J2646
Electrical abuse	Forced discharge	Discharge with max discharging current	Discharge with max discharging current	-
	Overcharge	Charge with twice the labeled maximum continuous charging current	Charge with max operating current to 125% of max voltage, complete 20 cycles	Charge with 1C/ 3C rate until reaching 200% SOC
	Overdischarge	-	Discharge with max operating current to 125% of max capacity, complete 20 cycles	Discharge with labeled maximum continuous discharging current to -100% SOC
	Separator shutdown	-	-	Heat cell 5 °C above shutdown temp, maintain for 10 mins, then apply 20 V with current limit of 1C, last for 30 mins

Although numerous tests are proposed in the LIB safety testing standards, battery performance degradation in field applications still cannot be well predicted or managed. More importantly, LIB safety accidents and catastrophic failures keep happening to the LIBs that have been certified by these standards (Kolly et al., 2013; National Transportation Safety Board, 2018a, 2018b). This clearly shows that the go/ no go tests in the existing LIB safety standards cannot effectively prevent unexpected catastrophic failures. In order to better address the safety concern of LIBs in field applications, real-time monitoring of LIB state of health (SOH) during the entire battery service life is desired. With a rapid and accurate evaluation of the SOH, early detection and prevention of LIB thermal runaway and other catastrophic failures can be expected.

As for better management of the LIB capacity decay and performance degradation, it is vital to understand the changes in electrode structure and corresponding influences on LIB cycling behavior. It should be noticed that the abuse tests proposed in existing safety testing standards are all at the cell or battery pack level. The electrode structure damage from these abuse tests cannot

be determined due to the complex structures in LIBs. The black box nature of LIBs requires the abuse tests to be modified so that they can be directly applied to the electrodes. This will help to enhance the understanding of abusing condition generated electrode degradation and corresponding effects on battery performance.

1.7 Research Scope and Outline

Based on the discussion above, LIBs are known to experience capacity decay over their service life, which affects the performance of battery powered applications. The capacity fading fate of LIBs depends on their service condition and is hard to predict. Environmental abusing conditions such as vibration are known to accelerate the aging of LIBs (Bruen, Hooper, Marco, Gama, & Chouchelamane, 2016; J. Hooper, Marco, Chouchelamane, & Lyness, 2016). Thus it is desired to investigate the mechanism for LIB performance degradation under representative abusing conditions that are most related to the battery service environment. The information from electrode structure evaluation after the abuse tests can be related to the performance degradation of LIBs with the abused electrodes, which helps to establish the relation between the in-service abusing conditions and corresponding LIB performance decay. This can provide support for the optimization of battery performance management strategy, etc.

Another aspect that is important for reliable and safe application of LIBs is to carry out real-time monitoring of the SOH. Since LIBs are exposed to unexpected changes in the service environment, laboratory safety tests cannot fully prevent catastrophic LIB failures in the field applications. Due to the unpredictable nature of the in-service abusing conditions, it is essential to develop a technique to monitor the SOH of LIBs in a time-effective manner, so that the risk of LIB accidents can be detected timely and prevent it from developing into uncontrollable accidents such as thermal runaway.

Work in this dissertation focuses on providing practical solutions for the two technical challenges described above. The first part of the dissertation focuses on analyzing the LIB electrode structure damage generated by dynamic impact. The relation between dynamic impact cycle, electrode structure damage, and LIB performance degradation is analyzed. This part of the work is described in chapter 2. The second part of the dissertation focuses on using a novel 3D printing based internal temperature sensor measuring technique for the early detection of LIB failure. External short circuit and overcharge tests are selected as the abusing conditions and direct

electrode temperature measurement is used to detect the failure event. The efficiency of LIB safety monitoring with the novel internal RTD and conventional battery surface mounted RTD are compared. This part of the work is described in chapter 3 and 4. The third part of the dissertation focuses on using a sensor network to carry out in-situ monitoring of LIB degradation under dynamic service environment, where vibration and impact are presented. A multidisciplinary examination of the LIB aging condition is carried out. The mechanisms of LIB performance degradation and capacity decay are identified and analyzed with the sensor network. With the comprehensive evaluation of LIBs, critical periods for the prevention of battery failure related to different failure modes are identified. This part of the work is described in chapter 5. Proposed future works are listed in chapter 6.

2. INVESTIGATION OF $LiCoO_2$ CATHODE RESPONSE TO DYNAMIC IMPACT USING RAMAN IMAGING BASED ANALYSES

Bing Li,[1,#] Ryan A. Adams,[2,#] Jafr Kazmi,[3] Abhijeet Dhiman,[1] Thomas E. Adams,[4] Vilas G. Pol, [2] Vikas Tomar[1,*]

[1] School of Aeronautics and Astronautics, Purdue University, West Lafayette, IN 47907, US

[2] Davidson School of Chemical Engineering, Purdue University, West Lafayette, IN 47907, US

[3] United States Military Academy at West Point, West Point, NY 10996, US

[4] Naval Surface Warfare Center, Crane Division, Crane, IN 47522, US

# Equal contribution

*Corresponding Author

Published in JOM 70 (8), 1423-1429.

https://doi.org/10.1007/s11837-018-2941-x

Abstract

This work presents Raman imaging-based evaluation of $LiCoO_2$ cathode of LIBs in response to direct dynamic impact. It was found that impact cycling introduced relatively consistent Raman shifts despite the structural and chemical heterogeneities of the cathode. Electrochemical performance change in impacted electrodes was a result of impact induced stress redistribution. Impact depth profiles, Raman shifts from dynamic loading, and post impact cycling performances employing scanning electron microscopy (SEM) were characterized to determine the impact related dynamic and electrochemical response.

Keywords: Li-ion Battery, Electrode, Dynamic Impact, Raman Spectroscopy, Stress redistribution

2.1 Introduction

Due to the high capacity and efficiency, LIBs are playing an increasing role for mobile applications, where dynamic vibration and shock during service and transportation are inevitable. For most regulations and research on LIBs, dynamic tests are not directly carried out on electrodes, but on the whole battery instead (Baddour-Hadjean & Pereira-Ramos, 2010; Gross, Giebeler, & Hess, 2013). In the work of Brand et al. (Anastassakis, Pinczuk, Burstein, Pollak, & Cardona, 1993), battery was impacted at the tabs, and electrodes bent from the dynamic input; internal resistance and capacity change were observed and contributed to the electrode deflection. However, despite the well-defined testing conditions, electrode dynamic profile was not clear due to resistance of the battery casing to the loads. There is also no chance for researcher to directly investigate electrode structural evolution to explain for the performance change after impact. There is also research on stress evolution during LIB cyclic lithiation including (Kitagawa, Yabuki, & Young, 2001), but the measurement is typically limited to sputtered Si electrode due to easiness of stress evaluation. Similar research on commercialized $LiCoO_2$ electrode is rarely reported, and we expect that direct impact test of $LiCoO_2$ cathode can provide information on the electrode response to dynamic conditions in the first place and assist in electrode optimization. To our best knowledge, there is no existing work on direct impact test of $LiCoO_2$ cathode due to its delicateness. Raman spectroscopy has been widely utilized in battery research to analyze chemical evolution during lithium intercalation (Gan & Tomar, 2014; Prakash, Gunduz, Oskay, & Tomar, 2018). Mechanical Raman analysis (MRA) was first reported by Anastassakis *et al.* (Abraham & Jiang, 1996) and has seen numerous applications due to its localized measuring capability and minor material damage (Doughty, 2010; Europe, 2015; International, 2013). Though prior Raman imaging studies exist for probing the chemical changes during charge-discharge (Mahajan & Rajopadhye, 2013), Raman imaging based analyses dedicated to studying the effects of dynamic loading related electrode behavior remains unexplored in LIBs. This work is designed to emulate shocks originating from transportation and in-service environments, by directly exposing the LIB electrode pack to impact cycling. With our novel Raman assisted nano-impact test, Raman shifts from dynamic loading and post impact cycling performances of $LiCoO_2$ cathode were analyzed to determine the impact related response.

2.2 Dynamic Testing Setup

In naval standard NAVSEA 9310, shock tests are carried out with half sinusoidal wave impacts with 6 μs pulse duration (Gross et al., 2013; Naval Ordnance Safety and Security Activity, 2010). In contrast, this work proposes to employ random shocks for electrode dynamic response analysis. Justification comes from concerns that most environmental shocks arise from bumps or transient changes in air/water flow, whose pattern cannot be described by sinusoidal functions (J. Hooper et al., 2016). After momentary impact the system typically recovers with original boundary conditions subsequently, similar to the condition of random shock. Considering these and for simplification, electrodes were impacted with random impacts orthogonally to the current collector plane, with N impact cycles (N=3, 12 and 1000) applied to imitate various transportation histories.

A nanomechanical impact setup was employed as shown in Fig. 2.1 (a,b). A stainless-steel impactor with 5 mm diameter was assembled on the pendulum and accelerated by a solenoid with a constant load over a defined depth to reach assigned velocity. Objective observation was carried out prior to and after impact test as shown in Fig. 2.1 (e). A compliance function derived with tungsten reference sample was employed for impact depth correction.

To perform impacting under analogous conditions in batteries, a 3D printed half-cell holder was designed. Geometry and sample mounting conditions are detailed in Fig. 2.1 (c). The electrode system was mounted into a clamp with the top spacer removed, to enable direct impacting and Raman analysis of the face up cathode. Below the anode is a stainless-steel spacer. Electrodes were clamped into 16 mm diameter pieces, with a 14 mm inner diameter for the impact window. Before assembly, impacted electrodes were cut to 12 mm diameter to eliminate the effect of the clamping force.

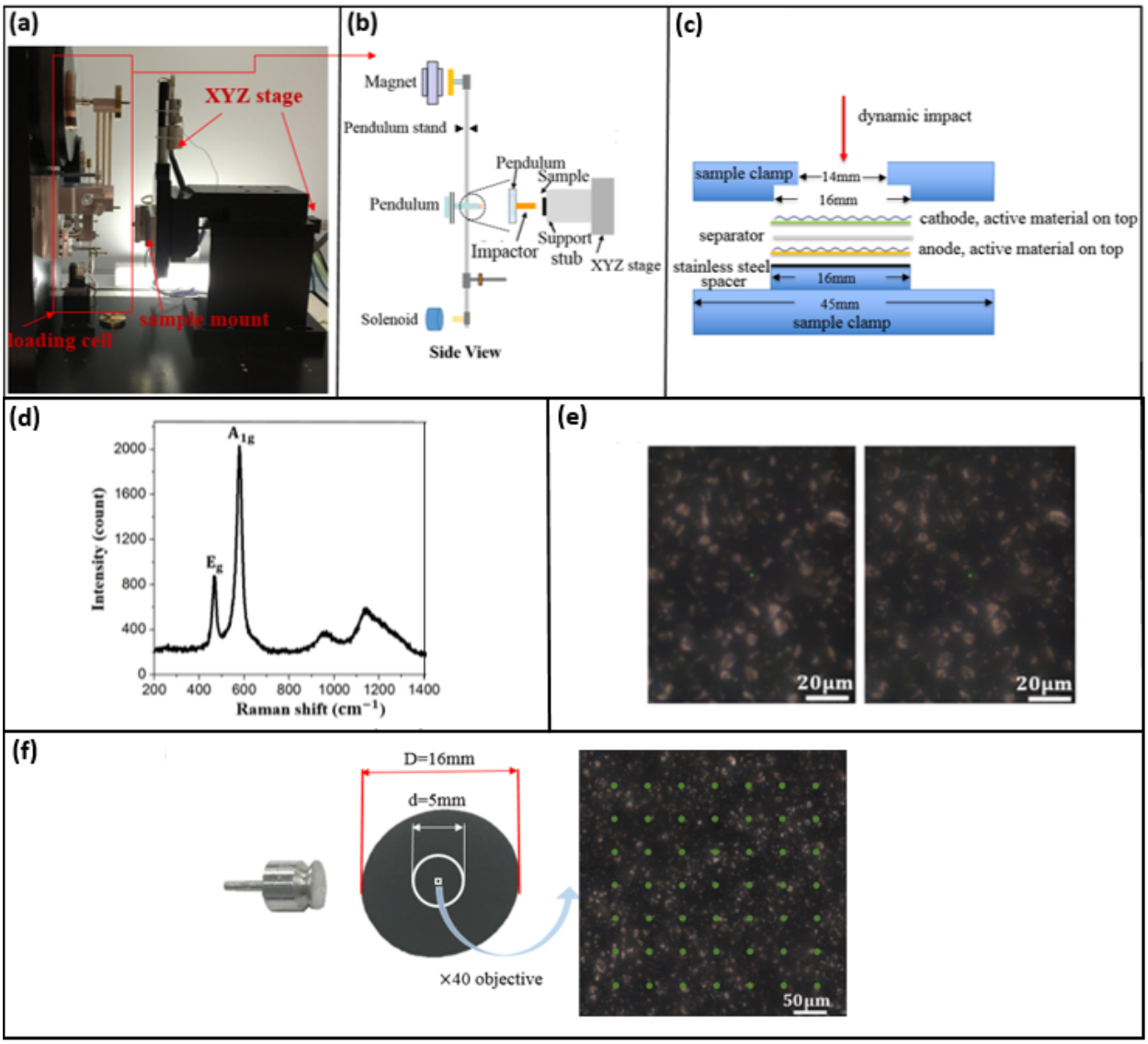

Figure 2.1. (a) Nanomechanical impact loading setup. (b) Schematic of loading cell. (c) Sample clamp and impact condition. (d) LiCoO2 cathode Raman spectrum. (e) Data point position matching. (f) Raman imaging point array.

2.3 Raman Spectroscopy and Scanning Electron Microscopy Analysis

The Raman spectrum analysis of the $LiCoO_2$ cathode was accomplished prior to and after impact. Spectra were collected with a 40x objective, 1 mW 532nm laser, two acquisitions of 15 s, and 5 spectra acquired for each measurement in the 7x7 array with 50μm span shown in Fig. 2.1 (f). The A_{1g} peak of $LiCoO_2$ was used due to its low noise level in adjacent spectrum regions as shown in Fig. 2.1 (d) and was fitted with the Lorentz function. To evaluate the effect of material

heterogeneity on Raman analysis, signal stability was evaluated with two individual mappings over the same area. The average A_{1g} peak position fitted for all measuring points from two individual measurements are 595.951 cm^{-1} and 595.943 cm^{-1}, with 0.009 cm^{-1} difference, which is small when compared with Raman shifts observed in dynamic impact tests. Individually, more than 85% of all data points have limited differences (≤ 0.2 cm^{-1}), which is significantly lower than the shift generated by impacts. Thus, Raman spectrum analysis is a reliable method to evaluate microstructural level changes of $LiCoO_2$ cathode from dynamic impact tests.

The $LiCoO_2$ electrode (A-C010) was obtained from the CAMP Facility at Argonne National Laboratory. The scanning electron microscopy (SEM) image is shown in Fig. 2.2 for the obtained electrode. A porous and heterogeneous structure is observed with micron sized $LiCoO_2$ particles mixed with nanoscale carbon conductive additive. Assembled coin cells were cycled from 3.0 – 4.3 V vs. Li^+/Li at 10 mA g^{-1}, using 1M $LiPF_6$ in ethylene carbonate / dimethyl carbonate = 50/50 (v/v) electrolyte.

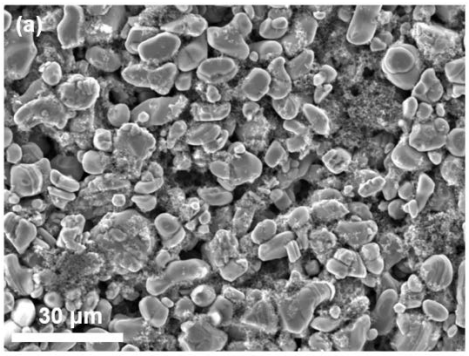

Figure 2.2. SEM image of a pristine $LiCoO_2$ electrode.

Table 2.1. Impact depth, velocity and Raman shift summary.

Impact Cycles	Average Maximum Depth (µm)	Average Maximum Velocity (mm s^{-1})	Average Final Depth (µm)	Average Raman Shift from Impact (cm^{-1})
3	37.839	2.742	35.586	-0.401
12	38.943	2.760	35.423	-0.750
1000	38.876	2.685	36.064	-0.789

2.4 Dynamic Impact Test Result

Representative impact depth history is shown in Fig. 2.3 (a). The impactor with an effective mass of 48 g impacted the sample with an average initial velocity of 2.712 mm s^{-1}, generating an average impact momentum of $1.302*10^{-4}$ kg m/s. The average maximum impact depth was 37.8 μm, as detailed in Table 2.1. From comparison of impact history over impact cycles, no obvious change is observed in peak depth as shown in Fig. 2.3 (c). This reproducible depth over cycling indicates that no significant bowl shaped deflection formed at the impacted region, nor produced significant degradation or change in the mechanical properties of the electrode. The impact depth likely resulted from gap closure between the electrodes and separator considering tensile strain at failure is reported as 12.97% for $LiCoO_2$ (L. Wu & Zhang, 2015). Assuming strain at tensile failure is generated throughout the thickness of the $LiCoO_2$ (49 μm), the resultant 6.36 μm deformation is much lower than the impact depth. In this case, material degradation should be noticeable, as porous structures are subject to more damage than solid materials under the same loading conditions [15]. There was no tendentious change observed in the impact depth profile, indicating limited compressive strain was accumulated.

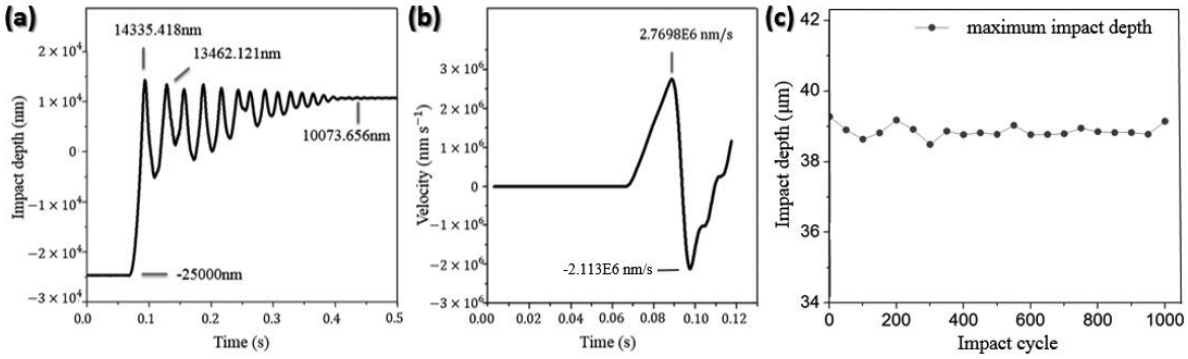

Figure 2.3. (a) Representative impact depth profile. (b) Representative velocity profile. (c) Impact depth history of 1000 cycles impact test.

From objective observation of electrodes prior to and after impact, no electroactive material peel off or microstructure structural changes were noticed. Additionally, SEM images before and after impacting presented no noticeable changes in particle area fraction for electrodes exposed to various impact cycles. This indicates that any degradation in electrochemical performance for cells with impacted electrodes should not be attributed to electroactive material loss in this study.

2.5 Results from Raman Spectroscopy and Li-ion Battery Cycling Analysis

Raman mapping of the A_{1g} peak relative shift for impacted electrodes is shown in Fig. 2.4 (a). As a function of incrementing impact cycle, the Raman shift moves increasingly in negative direction. Mechanical stress induced Raman shift is positive for compression for most materials, and the stress-Raman shift relation can be described typically by a linear function within the material elastic region (Kang, Qiu, Lei, & Hu, 2005; Kitagawa et al., 2001). Wang *et al*. applied pressure to $LiCoO_2$ via nitrogen as a transmitting medium, and a positive Raman shift-pressure relationship was observed with a linear relationship (X. Wang, Loa, Kunc, Syassen, & Amboage, 2005). Despite our rigorous system calibration and data stability analysis, we observed negative shifts after impact, in contradiction with the prior report (X. Wang et al., 2005). For our impact tests, a non-linear relationship between cycles and Raman shift was observed, with no sign of plastic deflection and limited disparity in impact depth profile over cycling.

In order to explain this observation, intrinsic stress should be considered. It was reported that for a $LiCoO_2$ film deposited onto a substrate (e.g. Si and Al) with a thickness at the level of nanometer to micrometer, the intrinsic stress within the $LiCoO_2$ film is introduced during deposition (Ketterer et al., 2009; Tintignac, Baddour-Hadjean, Pereira-Ramos, & Salot, 2012). The stress accumulated is typically compressive and varies in level, and has been reported as high as 1.5 GPa when annealed at 600 ℃, depending on protecting gas pressure (Ketterer et al., 2009). Considering the elevated temperature drying and pressing steps involved in electrode preparation, compressive residual stress is expected within electroactive material layer. Impact cycling, despite generating extra compressive deflection, could redistribute or release the intrinsic compressive stress, possibly leading to negative shifts for the A_{1g} peak due to release of compressive state. Support for this also comes from saturation of the A_{1g} peak relative shift, as there is no qualitative change in Raman shift between 12 and 1000 impact cycles despite the magnitude difference in cycles.

There is a possibility of a crystalline transition between layered and cubic spinel structure as function of applied pressure (W. Li, Reimers, & Dahn, 1994).There is a possibility of a crystalline transition between layered and cubic spinel structure as function of applied pressure (W. Li et al., 1994). For $LiCoO_2$ films with typical layered structure (space group $R\bar{3}m$), the structure is stable up to 26 GPa of pressure (X. Wang et al., 2005). Considering the loading profile of impact, the cathode structure should remain in the original state and impacting should not induce structural

changes in $LiCoO_2$. The observed Raman shifts could originate from changes in local conductive agent saturation conditions and particle contact. The heterogeneities in geometry and electrode material composition add to the complexity of impact generated mechanical effects. Local stress from impact could also originate from particle sheering, sliding, and inserting, and thus stress evolution in electrode may not be consistent with bulk $LiCoO_2$ under compression . For $LiCoO_2$ films with typical layered structure (space group $R\bar{3}m$), the structure is stable up to 26GPa of pressure (X. Wang et al., 2005). Considering the loading profile of impact, the cathode structure should remain in the original state and impacting should not induce structural changes in $LiCoO_2$. The observed Raman shifts could originate from changes in local conductive agent saturation conditions and particle contact. The heterogeneities in geometry and electrode material composition add to the complexity of impact generated mechanical effects. Local stress from impact could also originate from particle sheering, sliding, and inserting, and thus stress evolution in electrode may not be consistent with bulk $LiCoO_2$ under compression (X. Wang et al., 2005).

For direct impacting of $LiCoO_2$ cathode, the observations indicate that compressive stress is not accumulated within the electrode but intrinsic compressive state is released, as the Raman shift analysis contradicts with the pressure generated response of bulk $LiCoO_2$. Wang *et al.* reported that with applied pressure up to 18GPa, the pressure dependence of mode A_{1g} frequency can be described by (W. Li et al., 1994):

$$\omega(P) = 594.7 + 3.15P - 0.006P^2 \tag{2.1}$$

where ω is Raman shift of A_{1g} mode in cm^{-1}, and pressure P is in GPa. From equation (2.1), the estimated equivalent stress released from impact is calculated and presented in Fig. 2.4 (b). However, in this study the load applied was limited, and for high load cases where material degradation and hardening occur, Raman imaging conditions may be different. The observation indicates that for monitoring dynamic impacting effects on $LiCoO_2$ cathode, impact cycling test and Raman analysis should be applied on the electrode directly.

To analyze the effect of impacting on electrochemical performance, LIB half-cells with impacted cathodes were constructed and cycled, with the average first cycle overpotential shown in Fig. 2.4 (c) and first cycle efficiencies in Fig. 2.4 (d). Noticeably, the overpotential increases with impact number describing a rise in cell resistance with impacting.

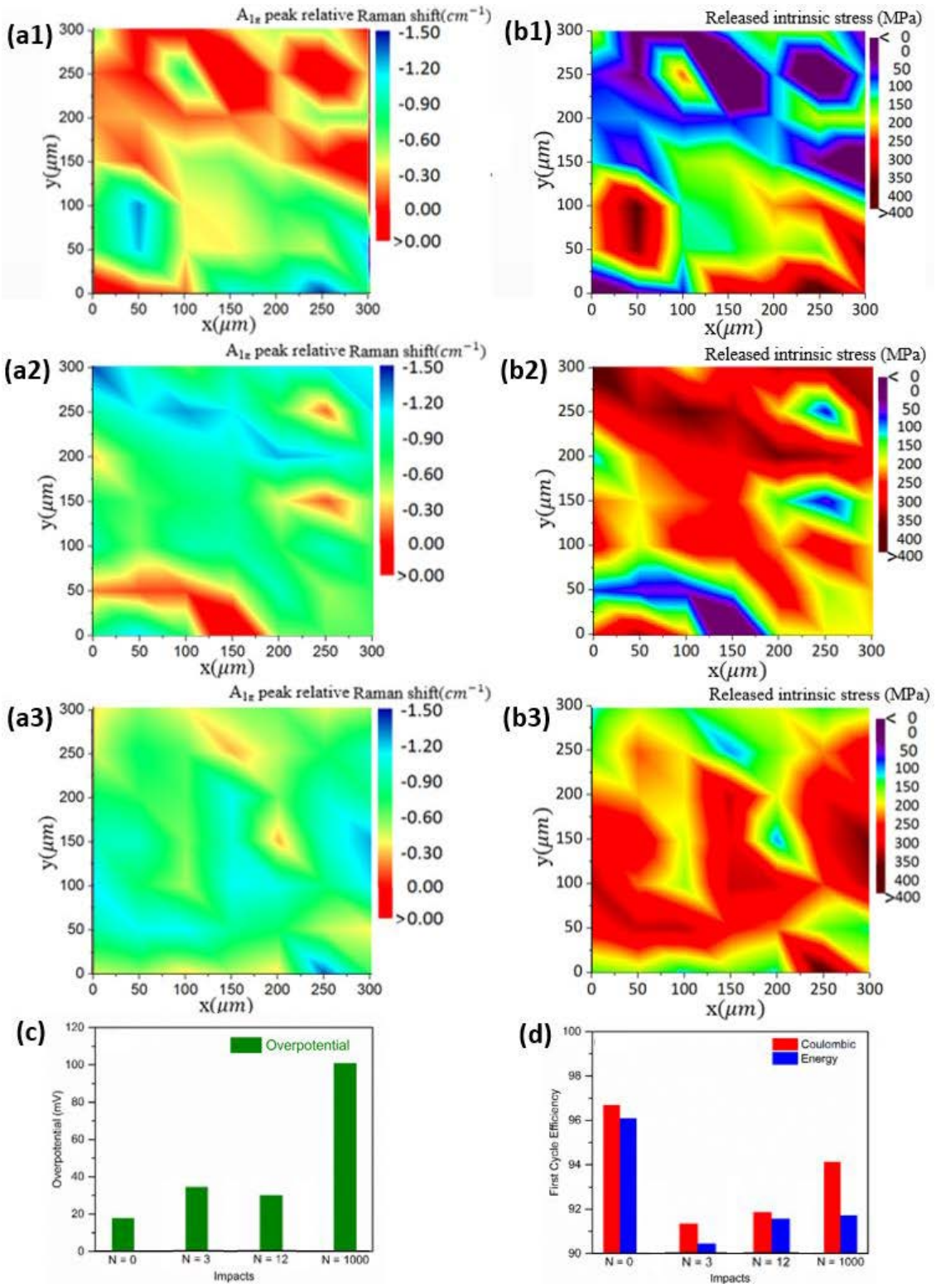

Figure 2.4. (a) A_{1g} peak relative shift imaging for impacted $LiCoO_2$ electrode (a1: 3; a2: 12; and a3: 1000 impact cycles). (b) Equivalent intrinsic stress released from impact (b1: 3; b2: 12; and b3: 1000 impact cycles). (c) First cycle overpotential. (d) First cycle efficiency.

The decrease in first cycle coulombic and energy efficiency indicates that impacting degrades electrochemical performance and accelerates ageing, possibly due to less intense bonding within the electrode material from intrinsic compressive stress relaxation.

2.6 Conclusion

In this study, a novel direct impact test and Raman analysis were utilized to study the influence of mechanical impact cycling on heterogenous LIB cathode. The impact depth profile and unusual negative Raman shift suggest that impacts cause intrinsic compressive stress release; while accumulated compressive strain from impact is limited. Raman imaging indicated release of residual stress in LIB electrodes from impact and resulting change in LIB efficiency. Reduced efficiency and increased overpotential of impacted electrodes are observed in the first cycle and related with bonding condition changes from impact. These findings present the importance of direct evaluation of dynamic loading related effects on LIB electrode for utilization in electric vehicles and other applications with possible dynamic input.

3. LITHIUM-ION BATTERY THERMAL SAFETY BY EARLY INTERNAL DETECTION, PREDICTION AND PREVENTION

Bing Li [1], Mihit H. Parekh [2], Ryan A. Adams [2], Thomas E. Adams [3], Corey Love [4], Vilas G. Pol[2,*], Vikas Tomar [1,*]

[1] School of Aeronautics and Astronautics, Purdue University, West Lafayette, IN 47907, USA

[2] Davidson School of Chemical Engineering, Purdue University, West Lafayette, IN 47907, USA

[3] Naval Surface Warfare Center, Crane Division, Crane, IN 47522, USA

[4] Naval Research Laboratory, Washington, DC 20375, USA

[*] Corresponding Author

Published in Scientific Reports 9 (1), 1-11.

https://doi.org/10.1038/s41598-019-49616-w

Abstract

Temperature rise in LIBs due to solid electrolyte interfaces breakdown, uncontrollable exothermic reactions in electrodes and Joule heating can result in the catastrophic failures such as thermal runaway, which is calling for reliable real-time electrode temperature monitoring. Here, we present a customized LIB setup developed for early detection of electrode temperature rise during simulated thermal runaway tests incorporating a modern additive manufacturing-supported resistance temperature detector (RTD). An advanced RTD is embedded in a 3D printed polymeric substrate and placed behind the electrode current collector of CR2032 coin cells that can sustain harsh electrochemical operational environments (acidic electrolyte without Redox, short-circuiting, leakage etc.) without participating in electrochemical reactions. The internal RTD measured an average 5.8 °C higher temperature inside the cells than the external RTD with almost 10 times faster detection ability, prohibiting thermal runaway events without interfering in the LIBs' operation. A temperature prediction model is developed to forecast battery surface temperature rise stemming from measured internal and external RTD temperature signatures.

3.1 Introduction

LIBs have a profound impact on the modern industry and they are applied extensively in aircraft, electric vehicles, portable electronic devices, robotics, etc. (J. Lee et al., 2014; C.-Y. Wang et al., 2016; H. Wu et al., 2014). However LIBs are prone to failure due to overheating, over-discharging, over potential or short circuiting (Z. Chen, Xiong, Lu, & Li, 2018). During such abusive events chemical energy gets converted to thermal energy rapidly, which can cause heat accumulation resulting in thermal runaway, fire and explosion (Peng & Jiang, 2016). Although there are various safety installations at present such as pressure release valves, shutdown separators, and one-shot fuses, severe battery hazards have been reported repeatedly (Z. Chen et al., 2018). This calls for an in-service thermal monitoring approach. One simple way applied intensively is to measure battery surface temperature (Abaza et al., 2018; M.-S. Wu, Chiang, Lin, & Jan, 2004). Despite the simplicity, external surface temperature monitoring has been shown ineffective due to dissipated heat for LIB safety management (G. Zhang et al., 2015). Temperature difference within LIB during battery failure impairs reliability and efficiency of surface temperature based safety management. Finegan *et al*. analyzed short circuit of 18650 LIB with infrared camera and the temperature rise occurred asynchronously across the cell (Finegan et al., 2017). Liu *et al*. and Zhao *et al*. simulated temperature evolution during short circuit of LIB with finite element method, and they observed significant temperature gradient in both thickness and height direction of shorted Li-ion pouch cells (B. Liu et al., 2018; R. Zhao, Liu, & Gu, 2016). A comparison of electrode and battery surface temperature showed that the external surface-based measurement detected peak temperature with reduced magnitude and time delay, and electrode temperature should be the key for prevention of thermal runaway (G. Zhang et al., 2015). Zhang *et al*. introduced internal short circuit to LIB with memory alloy, and it took 18 s on average for battery surface temperature to reached peak value after short circuit was triggered (M. Zhang et al., 2017). For real-time electrode temperature monitoring, Zhang *et al.* used a T type thermocouple inserted *between* the anode and separator of 18650 cells (G. Zhang et al., 2015). Electrode temperature during battery short circuit was recorded and compared with battery surface temperature. Novais *et al.* inserted a fiber bragg grating sensor between double layer separators of the pouch cell to measure temperature change in-operando (Novais et al., 2016). During cycling, fluctuation in the electrode temperature was reported.

Such internal sensor-based electrode temperature measurements have offered superior temperature measurement efficiency and accuracy. It has also been applied with widely adopted short circuit test for LIB safety analysis, where the shorted battery are subjected to risk of thermal runaway, fire and explosion (B. Liu, Yin, & Xu, 2016; Orendorff, Roth, & Nagasubramanian, 2011). When the examined LIBs were shorted to simulate thermal runaway conditions, temperature differences up to 50 ℃ were observed between the internal and external thermocouples, and the internal thermocouple reported the peak temperature nearly 20 s in advance (G. Zhang et al., 2015). However, it was noted that the sensor embedded between the cathode and anode (Novais et al., 2016; G. Zhang et al., 2015) may impede electrochemical reaction during the battery operation. It is challenging to maintain the contact between porous electrode material and a sensor without damaging the electrode, as microcracks are prone to form in porous structure under compression and lead to material fracture (Tomar, 2009). During battery thermal hazards such as a thermal runaway scenario, violent temperature rise leads to cracking of the electrode material (S.-M. Lee, Kim, & Byeon, 2018) and other particle based structures (Tomar, Gan, & Kim, 2010), which can impair the contact between the sensor and electrode material. Our previous work also showed that direct mechanical load influences the electrochemical performance of $LiCoO_2$ (LCO) cathode significantly (B. Li et al., 2018), implying that inserting a sensor between the electrodes may not be preferable.

In this work, a novel method of incorporating a resistance temperature detector (RTD) behind the cathode current collector of a LIB via additive manufacturing was developed for electrode damage minimization and internal LIB in-operando temperature measurement efficiency improvement. Customized LIBs (CR2032 coin cells) were tested for structural and electrochemical stability in vibrational loading environments. The thermal hazard detecting capability was evaluated using intentional heat rise due to an applied external short circuit (G. Zhang et al., 2015). Internal RTD placement yielded significantly superior measuring efficiency and accuracy in comparison to literature reports.

3.2 RTD Sensor Embedded Li-ion Coin Cell for Electrode Temperature Measurement

For the CR2032 coin cells employed in this work, the RTD was incorporated into a customized polylactic acid (PLA) spacer with additive manufacturing, which was placed beneath the cathode as shown in Fig. 3.1. To develop a feasible approach to detect battery thermal runaway

in-operando and meet requirement on commercial LIBs, the design of a customized RTD embedded LIB cell was dictated by three key factors: (1) to acquire the cathode electrode temperature accurately and effectively; (2) to eliminate sensor induced interference due to LIB operation; and (3) to minimize sensor induced electrode damage. For accurate real-time electrode temperature monitoring, reliable sensor-electrode contact is desired, which requires that the sensor surface pairs well with the electrode. Pt1000 RTD (by Omega Engineering Inc.) with a 4mm × 5mm flat Al_2O_3 sensing surface was selected in this work. Pt1000 RTD has been extensively applied in process temperature monitoring, including LIB electrolyte stability analysis (Keil, Rumpf, & Jossen, 2013; Logan et al., 2018), and LIB cycling (P. Wang et al., 2016). The Pt sensing element employed in this work had a temperature dependent resistance, R, of:

$$R=(1+3.9083\cdot10^{-3}\,℃^{-1}\cdot T-5.775\cdot10^{-7}\,℃^{-2}\cdot T^2-4.183\cdot10^{-12}\,℃^{-4}\cdot a\cdot T^3)\ k\Omega \qquad (3.1)$$

where a = (T-100) ℃ for T<0 ℃ and a = 0 ℃ for T > 0 ℃. The RTD provided an average sensitivity of 3.883 Ω/℃ within the ordinary battery operation temperature of -10 ℃ to 50 ℃ (Aris & Shabani, 2017).

A strip of aluminum current collector was applied across the PLA spacer for cell conductivity. By embedding the customized spacer in the CR2032 cell, a new pattern of measuring electrode temperature from the electrode current collector was achieved, which eliminated sensor induced disturbance to battery operation by removing the sensor from the gap between the electrodes. Thickness variation of the RTD embedded spacer was controlled within 10 μm for contact reliability between the RTD and the electrode. The well-maintained spacer-electrode pairing can improve measurement efficiency and control electrode damage during temperature monitoring.

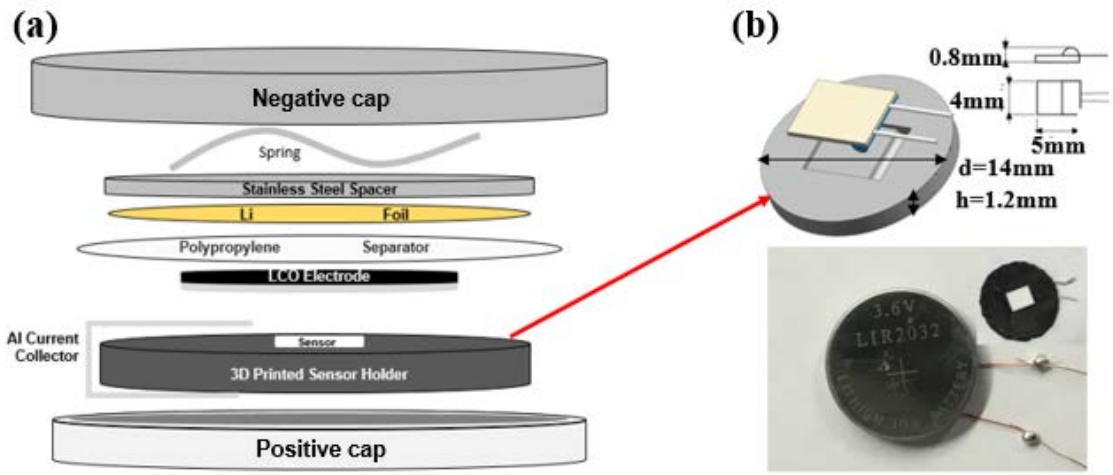

Figure 3.1. (a) Schematic of customized RTD embedded LIB coin cell; (b) RTD embedded PLA spacer and CR2032 cell with internal RTD. Dimension of the RTD embedded spacer was comparable to ordinary CR2032 coin cell spacer, allowing for reliable sensor-electrode contact and cell sealing after assembly.

In order to ensure that the RTD embedded PLA spacer is electrochemically inert and will not introduce side reactions during LIB operation, the spacer was submerged in LIB electrolyte (1M $LiPF_6$ EC/DEC (Sigma-Aldrich)) for 5 days. A fourier-transform infrared (FTIR) spectrum of the electrolyte was acquired and compared with the spectrum of the pristine electrolyte. For temperature measurement efficiency and accuracy evaluation, the RTD embedded spacer was firstly applied on a PID controlled hot stage, which was preset to various temperatures ranging from 30 ℃ to 70 ℃. The spacer was mounted onto the hot stage with a pressure of 1500 psi (same pressure applied in cell crimping), while temperature readings from the RTD were recorded for 3 mins. Then, the CR2032 coin cell with RTD embedded spacer was cycled under vibration loading condition, as described in NAVSEA 9310 (Naval Ordnance Safety and Security Activity, 2010) and depicted in Fig. 3.2 (a). Four electrochemical cycles were completed and the electrochemical performance of the cell was analyzed. The results on electrochemical performance of the internal RTD embedded cell is provided in Fig. 3.3 (e).

The result of hot stage temperature measurement with RTD embedded spacer is presented in Fig. 3.3 (a), where the RTD embedded spacers were clamped onto the hot stage at t = 20 s. As shown, the customized spacer provides temperature readings with an error < 1 ℃ up to 55 ℃, and an average error of 0.82 ℃. The response rate of the spacer is evaluated in Fig. 3.3 (b, c), where

the response time t_{90} is defined as the time required for RTD to capture 90% of the total temperature shift (Lin, Wang, Li, Miao, & Liu, 2017). The average value of t_{90} is 5 s for the RTD embedded spacer, which agrees with the observation for the RTD response rate. The t_{90} also presents no dependency on target temperature within the assessed temperature range. These results indicate that the RTD embedded spacer could detect thermal hazard with high efficiency and has limited measuring error over the temperature range covering room temperature to the onset temperature of LIB thermal runaway (Q. Wang, Sun, Yao, & Chen, 2005).

In FTIR spectral analysis of RTD embedded spacer inertness, there are no changes in band intensity and frequency of electrolyte as shown in Fig. 3.3 (d). The consistent FTIR spectra indicate that there is no transition in electrolyte composition and concentration (Ellis et al., 2018), and the RTD embedded spacer is electrochemically inert, avoiding interference to LIB operation. During cycling of the RTD embedded cell, based on the NAVSEA 9310 vibration test, the LIB cell presents consistent charge/discharge behavior and the cell structure is robust under applied vibrational load.

Customized CR2032 cells with 12.5 mm diameter electrodes were prepared as discussed previously. Cells were cycled between 3 V and 4.3 V with "C/12 rate" as shown in Fig. 3.3 (e). Cells report a discharge capacity of about 120 mAh g^{-1} and a charge capacity of about 140 mAh g^{-1} as shown in Fig. 3.3 (e). First cycle capacity of the cell is slightly lower due to the formation of a passivation layer on the surface of the cathode.(Jurng, Brown, Kim, & Lucht, 2018). Following that, the charge and discharge profiles overlapped well for the next cycles. During charging, delithiation starts at around 3.9 V; while discharging, lithiation of the cathode starts at around 3.7 V without altering the profile of LCO because of the sensor assembly.

Electrochemical impedance spectroscopy (EIS) of the customized CR2032 was conducted at the OCV potential as shown in Fig. 3.3 (f). In the high-medium frequency area, the plot depicts depressed semicircles and in the high-frequency area it shows linear Warburg impedance. Ohmic resistances for all the electrodes were similar to each other, ~ 2.5 Ω. Charge transfer resistance differed from each other. An inverse relationship between charge transfer resistance and the size of the electrodes was observed. For the smallest electrode, charge transfer impedance was 527 Ω, whereas for the largest electrode, it was 65 Ω. The difference in charge transfer resistance between small and large electrodes arose because the effective area became a significant factor in regions of low frequency, as more charge could pass through the large area, causing impedance to decrease

(Ahmed & Reifsnider, 2011). High charge transfer resistance has also been reported in coin cells with electrodes smaller than the spacer (Adams et al., 2017). The impedance of RTD embedded cells was found to be comparable with the other CR2032 coin cells fabricated in a controlled lab environment (Adams et al., 2017; Juarez-Robles, Chen, Barsukov, & Mukherjee, 2017), and the contribution of the customized spacer with an RTD to the cell impedance was limited. Since all four coin cells had limited and comparable ohmic resistance and the effect of 3D printed spacer on cell performance in short circuit test was negligible, the result from internal RTD measurement could be employed for safety management of ordinary coin cells with stainless steel spacer.

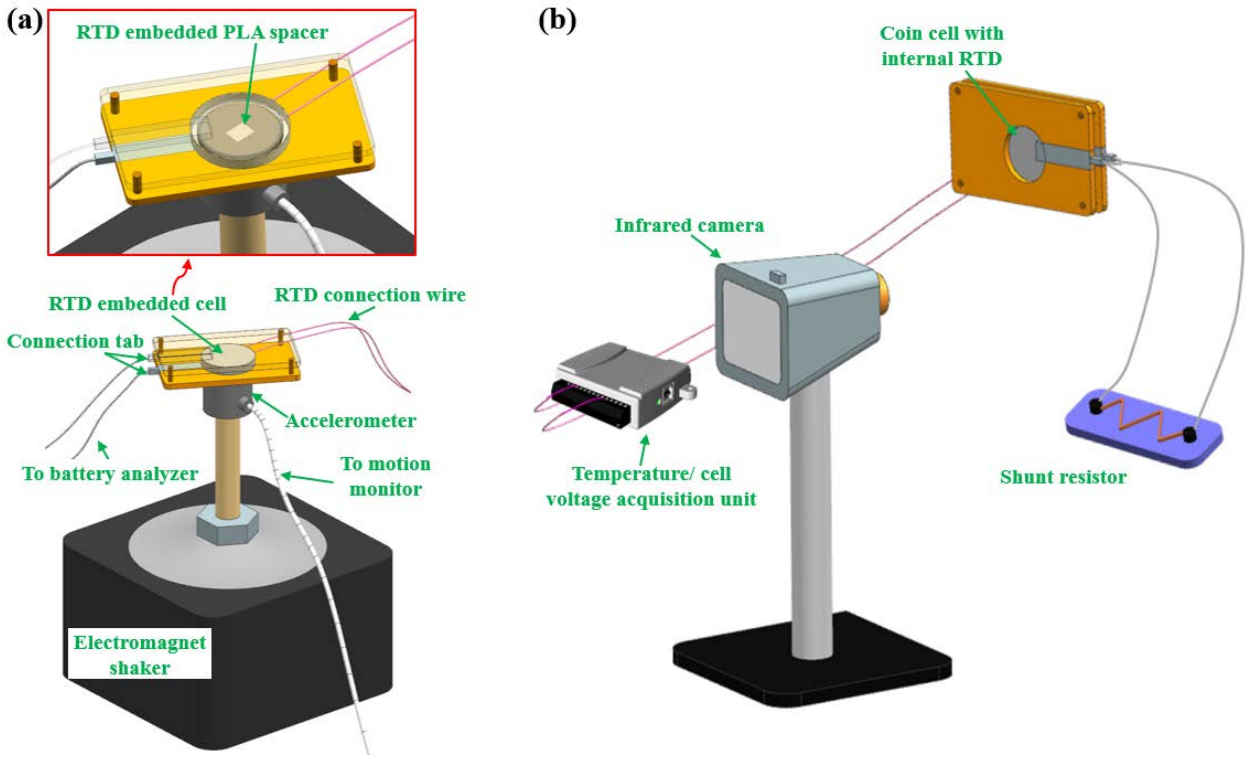

Figure 3.2. (a): Portable battery cycling setup for LIB performance analysis during vibration; (b): LIB short circuit testing and temperature monitoring platform.

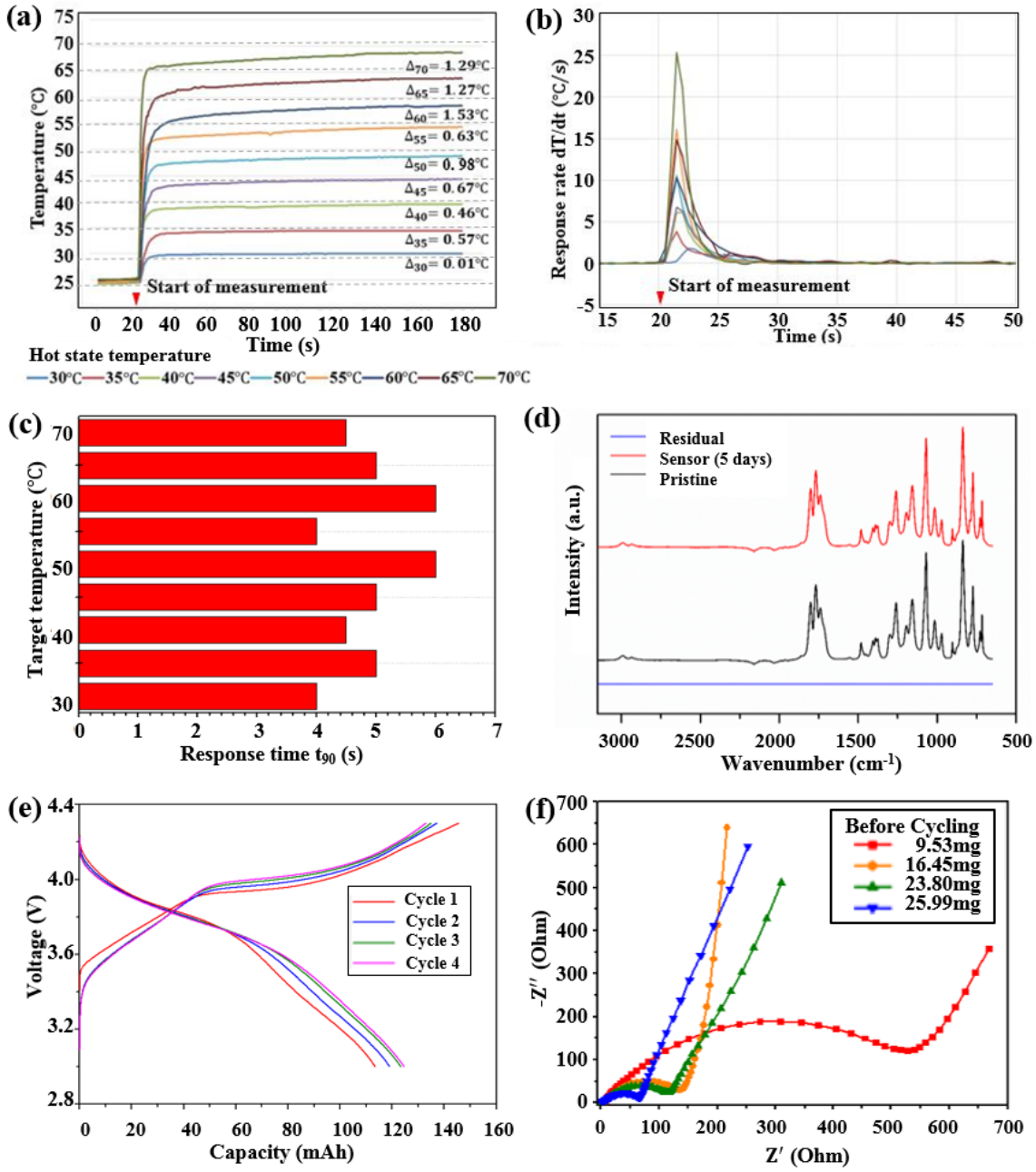

Figure 3.3. (a) Hot stage temperature measurement with RTD embedded spacers; (b) RTD embedded spacer measurement response rate; (c) RTD embedded spacer measurement response time t_{90}; (d) FTIR spectra for electrolyte stability testing; (e) Comparison of charge/discharge curves for sensor embedded cell over vibration; (f) Electrochemical impedance spectroscopy of the constructed cells at OCV (3.1 V vs Li/Li+) with RTD.

3.3 External Short Circuit Test and Real-time Electrode Temperature Monitoring

Short circuits are a common concern for aged batteries due to dendrite formation and separator degradation (F. Han et al., 2019; Lagadec, Zahn, & Wood, 2018; Love, Baturina, & Swider-Lyons, 2015), and it is also common in transportation-related accidents such as electric vehicle crashes (National Transportation Safety Board, 2018a, 2018b). Short circuits can induce dramatic changes in electrode structure and the electrochemical environment of the battery (R. Zhao et al., 2016). An external short circuit test was employed for evaluation of thermal hazard capturing capability of the RTD embedded cells in this work. The platform for external short circuit test and temperature monitoring is shown in Fig. 3.2 (b).

In the short circuit test, a 15 mΩ shunt resistor was used for external shorting, and the total resistance of the external circuit was determined to be 19.8 mΩ. The low resistance external circuit generated a "hard" short circuit condition per NAVSEA 9310 (Naval Ordnance Safety and Security Activity, 2010). Four groups of RTD embedded LIBs with LCO cathode diameters of 9.5 mm, 12.5 mm, 14.9 mm, and 15.6 mm were prepared (LCO loading 14.53mg/cm^2) and analyzed in the short circuit test. Before testing, the cells were cycled between 3.0 V and 4.3 V for cathode electrolyte interface (CEI) formation (Jurng et al., 2018), which would decompose during the short circuit test and introduce further exothermic reaction (Bandhauer, Garimella, & Fuller, 2011). The cells were then fully charged and shorted for 24 hours according to NAVSEA 9310 (Naval Ordnance Safety and Security Activity, 2010). Two RTDs were used for electrode and battery surface temperature measurement: one embedded on the spacer (internal RTD) and one attached on the battery surface (external RTD). The electrode and battery surface temperature were recorded for the first hour as short circuit related electrochemical reactions were observed to be negligible afterward. An infrared camera (FLIR E40) was used for battery surface temperature recording as a comparison tool for the external RTD measurement result.

A comparison of examined LIB temperature profiles obtained with internal RTD, external RTD, and infrared camera over the first 10 mins of the short circuit test (cathode diameter: 12.5mm) is shown in Fig. 3.4 (a). The temperature obtained with the infrared camera is unreliable due to the high-level fluctuation which mainly originates from changes in ambient convection characteristics (Mistry, Palle, & Mukherjee, 2019). In the comparison of RTD measurements, the first difference is in the maximum temperature: T_{max} captured by internal RTD is on average 5.8 ℃ higher than the external RTD measured average as shown in Fig. 3.4 (b). This difference contributes to the

thermal contact resistance, which is most significant at electrode-separator contact surface and battery poles (S. Chen, Wan, & Wang, 2005; Yi, Kim, Shin, Han, & Park, 2013). The internal RTD measurement avoids the high-level temperature gradient, thus providing accurate electrode temperature monitoring for thermal event detection. The second main difference is in the peak temperature detection time: external RTD detects peak temperature when the internal RTD reading is stabilized or starts decreasing. The measuring efficiency difference arises from energy loss in heat conduction: when heat generated in the electrodes is conducted to the battery surface, part of it is consumed by the temperature rise of battery components, and part of it is dissipated to the air. As a result, the external RTD will fail to reflect the actual temperature rising rate, leaving the cell continuously exposed to potential thermal hazards.

For further evaluation of measurement efficiency, detection time t_{90} is compared for internal and external RTDs. As discussed, t_{90} is defined as the time to detect 90% of the maximum temperature rise measured by external RTD (ΔT_{ext}). ΔT_{ext} is compared with the maximum temperature rise measured by the internal RTD (ΔT_{int}) in Fig. 3.4 (b) and with the t_{90} of two RTDs in Fig. 3.4 (c). The internal RTD detects 90% of ΔT_{EMax} in 7.45 s on average, which is 7-10 times faster than the external RTD. The measuring efficiency difference builds up with the increase of cathode mass as shown in Fig. 3.4 (d), indicating that internal sensor based measurement will be more instructive for thermal hazard detection in LIBs with higher capacity. The high measuring efficiency of the internal RTD is attributed to the well maintained sensor-electrode contact. Reliable sensor-electrode contact is maintained by the pressure load applied during cell fabrication, allowing for effective heat conduction from the current collector to internal RTD. In existing work on electrode temperature measurement, the sensors were directly applied onto the porous electrode material (G. Zhang et al., 2015) with limited control of sensor-electrode contact and installation stress. Excessive installation pressure could lead to electrode material damage and impair battery performance (D. Liu et al., 2013). Also, electrode particle cracking and peel-off occurred during LIB thermal runaway, which further impairs the unsecured sensor-electrode contact and can be observed in SEM images acquired on the cathode before and after the short circuit test, as shown in Fig. 3.4 (e, f).

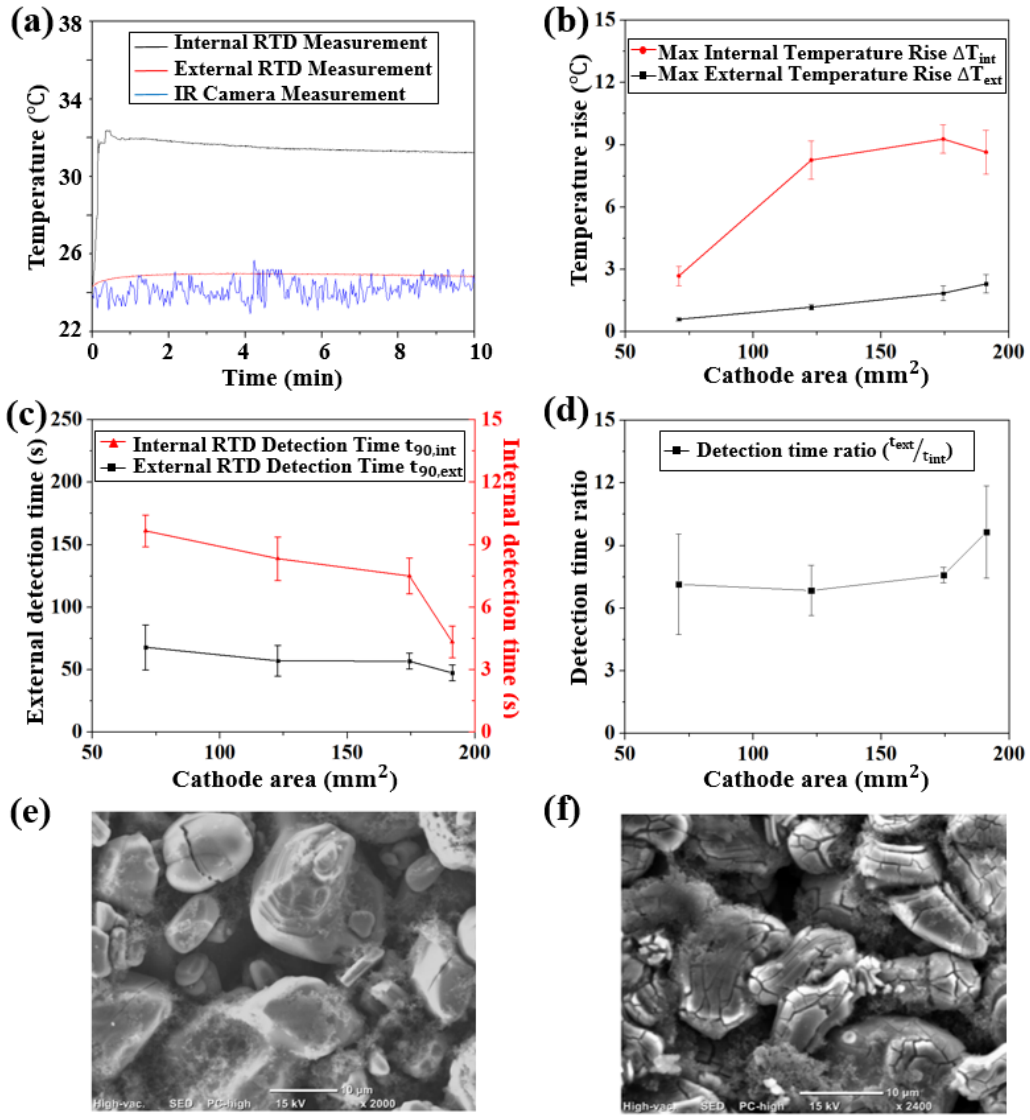

Figure 3.4. (a) Temperature measurements with internal RTD, external RTD and infrared camera in the short circuit test; (b) Maximum temperature rise detected by internal and external RTDs; (c) RTD detection time $t_{90,\,int}$ and $t_{90,\,ext}$ of internal and external RTDs; (d) Detection time ratio t_{ext}/t_{int}; (e): SEM image of LCO cathode before short circuit test and (f): after short circuit test.

Despite electrode temperature monitoring with improved efficiency and accuracy, an internal RTD can also be used for the prediction of cell temperature evolution after the detected thermal hazard. When high temperature is detected in a LIB pack, involved cells will be removed from the circuit (B. H. Lee & Kim, 2002) and the subsequent cooling process is typically accomplished by convection in air (Mistry et al., 2019). As the current drains rapidly in the short

circuit test (within 5 s), the temperature decrease process of CR 2023 cells can be modeled with natural convection, and a general energy balance equation of LIB cells can be written as (Mistry et al., 2019):

$$mC\frac{dT_{ext}}{dt} = \dot{Q} - hA(T_{ext} - T_{\infty}) \tag{3.2}$$

where m is cell mass, C is heat capacity of the cell, h is convective heat transfer coefficient, A is convection area, T_{∞} is ambient temperature, T_{ext} is battery surface temperature and $\dot{Q}$ is the internal heat source term. A simple way to obtain the analytical solution of equation (3.2) is to assume uniform temperature distribution of the cell and neglect the $\dot{Q}$ term during the cooling process, which provides a solution for T_{ext} as (Mistry et al., 2019):

$$(T_{ext} - T_{\infty}) = (T_{e0} - T_{\infty})\exp\left(-\frac{hA}{mc}t\right) = (T_{e0} - T_{\infty})\exp\left(-\frac{t}{\tau}\right) \tag{3.3}$$

with T_{ext}=T_{e0} at the beginning of convective cooling and τ is the convection time constant ($\frac{hA}{mc}$) that can be determined with temperature evolution in natural convection cooling of the cell. However, our previous measurements show that there is a significant temperature gradient within the cell, and the thermal conduction from the electrode to the cell surface is non-negligible at the start of the cooling process. Thus, the model in equation (3.3) will fail to reflect the actual change of battery surface temperature and it is necessary to consider the thermal energy transferred from the electrode for accurate surface temperature prediction. Considering this, the cooling process is separated into two phases: in the first time period the electrode temperature is different from the cell surface temperature, and the electrode system provides the internal heat source term $\dot{Q}$, in the second phase cell temperature is relatively uniform and $\dot{Q}$ can be neglected. Based on the measurement efficiency comparison of internal and external RTD in Fig. 3.4 (d), separation for periods 1 and 2 can be set at $5t_{in}$, where t_{in} is the time for the internal RTD to detect the maximum electrode temperature, as shown in Fig. 3.5 (a).The new energy balance equation for the battery can be written as:

$$\begin{cases} mC\frac{dT_{ext}}{dt} = \dot{Q} - hA(T_{ext} - T_{\infty}) & t_{in} \le t < 5t_{in} \quad (3.4\text{-}1) \\ mC\frac{dT_{ext}}{dt} = -hA(T_{ext} - T_{\infty}) & 5t_{in} \le t \quad (3.4\text{-}2) \end{cases}$$

The internal heat source term $\dot{Q}$ is given as:

$$\dot{Q} = -m_e C_e \frac{dT_{in}}{dt} \tag{3.5}$$

where T_{in} is the temperature obtained with internal RTD, m_e and C_e are the mass and heat capacity of the system that possesses a temperature of T_{in}. It is assumed that for the $LiCoO_2$ cathode, the Li anode and stainless-steel spacer above the anode possess a temperature of T_{in}, considering the tight contact between these layers, and the values of m_e and C_e are calculated, accordingly (Kawaji et al., 2002; Lide, 1995). After reaching the maximum value at t_{in}, T_{in} is modeled to decay exponentially:

$$T_{in} = T_\infty + (T_{i0} - T_\infty) \cdot \exp(-a \cdot t) \tag{3.6}$$

where a is the time coefficient to be determined and the value of T_{in} over $t_{in} \leq t \leq 2t_{in}$ is used for the derivation of a. Then the solution of equation (3.4-1) can be obtained numerically with MATLAB providing the initial value of T_{ext} at $t = t_{in}$, and the solution for equation (3.4-2) is provided by equation (3.3). A comparison of battery surface temperature predictions with and without the contribution of the internal heat source $\dot{Q}$ is shown in Fig. 3.5 (b). The new model reduces error in maximum surface temperature prediction as shown in Fig. 3.5 (c). The ratio of T_{EMax} prediction error remains steady over different cathode sizes and the model can be applied to the cells with higher electrode mass. The proposed model can also predict battery temperature evolution after thermal hazard detection and avoid thermal hazard after removal of the cell.

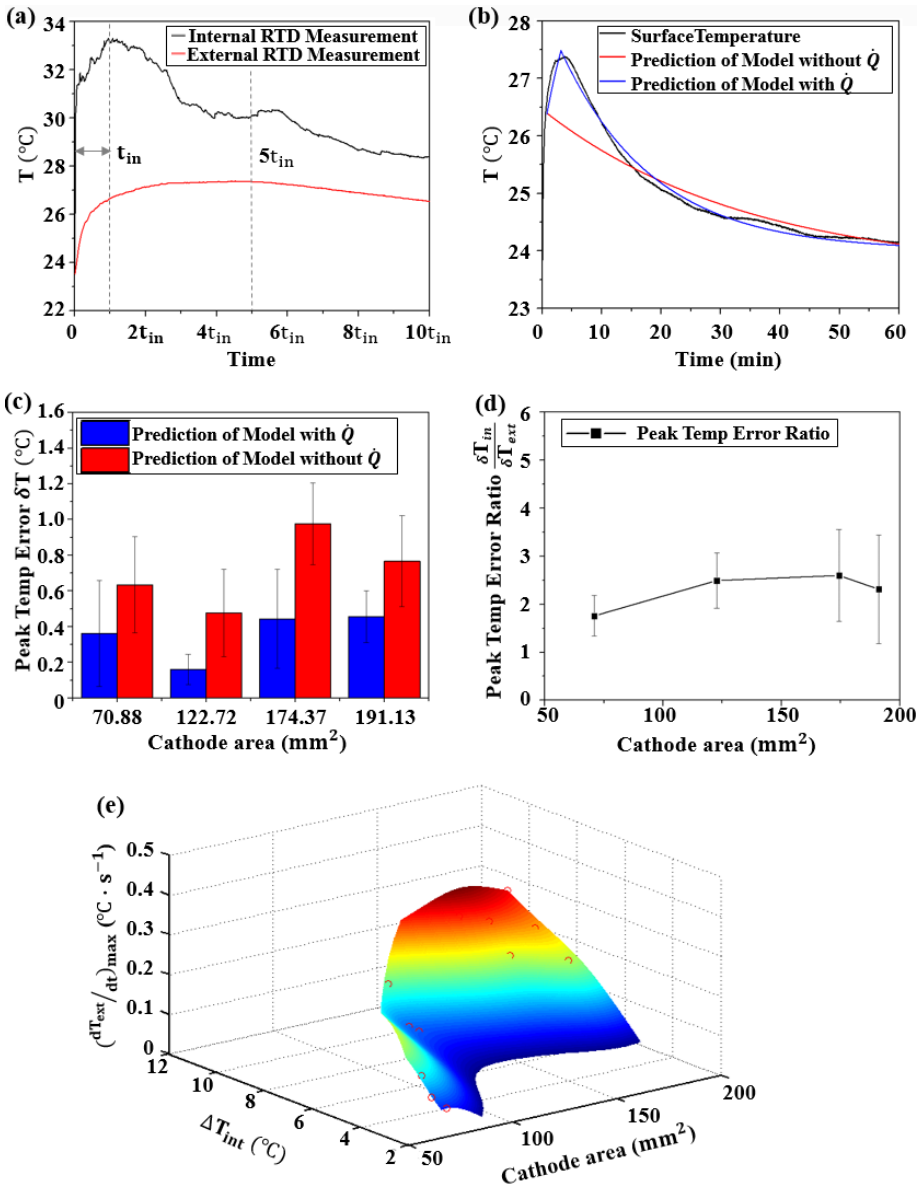

Figure 3.5. (a): Two phases of heat transfer in battery short circuit test; (b): Representative comparison of temperature model predictions; (c): Peak temperature prediction error comparison; (d): Peak temperature prediction error ratio; (e): Relation between cathode mass, peak internal temperature and maximum battery surface temperature rising rate.

The relation between temperatures measured with internal and external RTDs can also be used for improving the efficiency of surface temperature-based battery thermal runaway detection. A curved surface correlating maximum surface temperature increasing rate with cathode area, *A*, and

cathode temperature increase, ΔT_{int}, in short circuit is plotted by biharmonic spline interpolation and 4th order polynomial fitting with MATLAB in Fig. 3.5 (e). The relation can be written as:

$$\begin{aligned}(\frac{dT_{ext}}{dt})_{max} = &-1.83 + 0.060 \cdot A + 0.36 \cdot \Delta T_{int} - 6.88 \cdot 10^{-4} \cdot A^2 - 7.17 \cdot 10^{-3} \\ &\cdot A \cdot \Delta T_{int} - 0.011 \cdot \Delta T_{int}^2 + 3.28 \cdot 10^{-6} \cdot A^3 + 4.50 \cdot 10^{-5} \cdot A^2 \\ &\cdot \Delta T_{int} + 2.14 \cdot 10^{-4} \cdot A \cdot \Delta T_{int}^2 - 5.77 \cdot 10^{-9} \cdot A^4 - 7.84 \cdot 10^{-8} \\ &\cdot A^3 \cdot \Delta T_{int} - 8.83 \cdot 10^{-7} \cdot A^2 \cdot \Delta T_{int}^2\end{aligned} \quad (3.7)$$

The relation between ΔT_{int} and cathode area, *A*, of a coin cell is fitted with a cubic polynomial function:

It is found from equation (3.7) that the increasing rate of battery surface temperature in short circuit related thermal runaway is dependent on both electrode temperature rise and electrode mass. This increase arises because exothermic reaction in short circuit is mainly composed of SEI decomposition, reaction between cathode, anode and electrolyte and electrolyte decomposition at the electrolyte-electrode interface (J. Lee et al., 2014), and these reactions are dependent on electrochemically active mass as shown in equation (3.7). Electrode surface area determines the rate of thermal energy transfer from the electrode to battery surface. Thus, the thermal runaway risk level cannot be simply predicted with the change in surface temperature rise, but the cell capacity also needs to be taken into consideration. For CR 2032 cell with specific LCO cathode mass, when the increasing rate of surface temperature approaches the top part of the curved surface in Fig. 3.6 (e), there will be a high risk of thermal runaway and effective cooling such as forced air cooling should be applied to control the electrode temperature and detrimental thermal gradient across the cell (Carter & Love, 2018). For similar increasing rate of surface temperature, batteries with lower electrode mass will be more prone to thermal hazards, and a cell capacity dependent safety temperature threshold can be determined based on external RTD measurement with the relation between internal and external RTD reading established. Besides, some fluctuation was observed in temperature measured by internal RTD during the short circuit event. It represented instability in local heat generation and transfer. The fluctuation originated from changes in LIB structure during short circuit, including lithium dendrite formation, current collector dissolution, electrode particle peel- off, gas generation, etc. Dendrite could reduce cell resistance and trigger internal shorting (Love et al., 2015), which could enhance the short circuit. Current collector

dissolution and gas generation influenced cell impedance and local heat transfer condition (Fear, Juarez-Robles, Jeevarajan, & Mukherjee, 2018; Q. Wang et al., 2012). Electrode particle could peel off during thermal runaway (Yokoshima et al., 2019), leading to abrupt drop in cell capacity and heat generation rate at the region of peel off. The local measurement capability of internal RTD captured these transient regional processes, and it was instructive for LIB thermal runaway detection and prevention.

For prevention of short circuit related thermal runaway, a thermal runaway risk assessing strategy is developed for CR2032 coin cell based on internal and external RTD measurements as well as established relations between the electrode and battery surface temperature from equation (3.6) and (3.7):

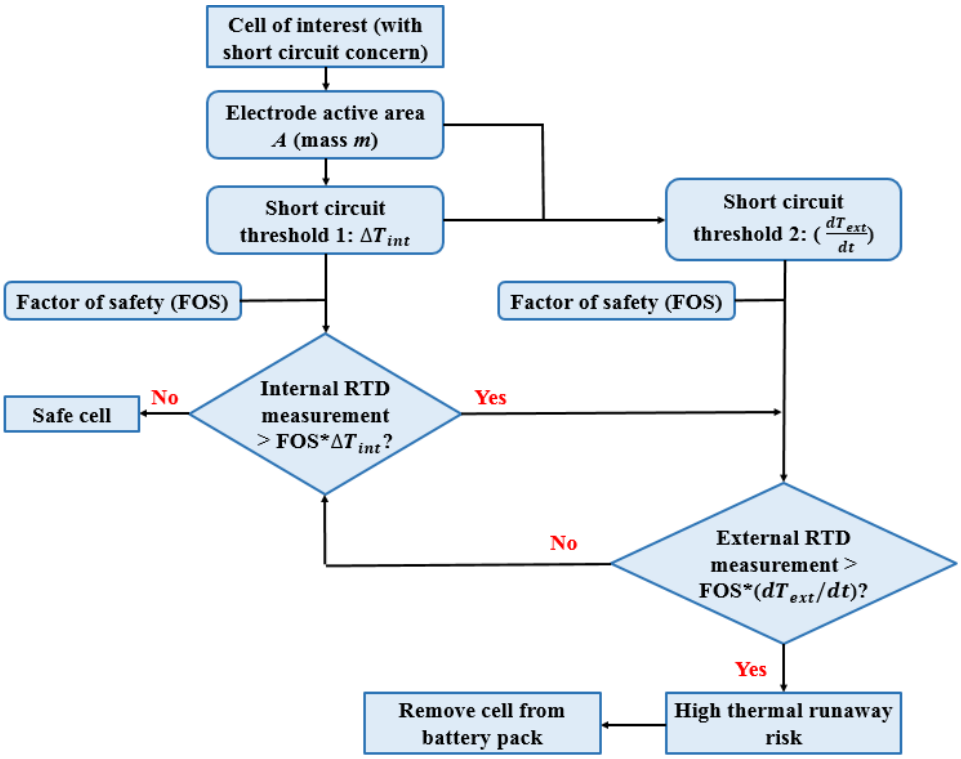

Figure 3.6. Strategy for protecting coin cell against short circuit related thermal runaway.

This thermal runaway prevention strategy consists of internal RTD and external RTD based protection. Due to the superior measuring efficiency, internal RTD measurement is critical when short circuit is of concern for a cell. Electrode temperature rise, ΔT_{int}, is used as the early signature

of thermal runaway and if the measured value excesses range for safe battery operation, the increasing rate of battery surface temperature will be calculated with the external RTD and employed for verification of assessment. If the battery surface temperature is rising in an unsafe manner based on equation (3.6) and (3.7), a high risk for thermal runaway is identified for the analyzed cell and it should be disconnected immediately. Scientific experimental efforts are underway to test multiple RTD sensors in pouch full-cell configurations for local heat generation mapping of the electrode.

3.4 Conclusion

In this study, a RTD sensor embedded PLA spacer was developed and incorporated inside the CR2032 coin cells for in-situ temperature monitoring. The customized cell presented reliable sensor-electrode contact and high structural robustness during cycling over continuous vibration, based on Navy standards. In the short circuit test, the internal RTD provided superior performance in measuring the electrode temperature compared to the external RTD. In addition, the internal RTD reported peak temperature 7-10 times faster than the external RTD, providing a better chance for battery hazard prevention. Electrode temperature measurement with an internal RTD was also employed for battery surface temperature prediction in short circuit, providing surface temperature evolution prediction with reduced error. Finally, the relation between internal RTD measurement, external RTD measurement and electrode mass was obtained for reliable short circuit detection and prediction based on battery surface temperature measurement.

4. IN-SITU DETECTION OF ELECTRODE TEMPERATURE DURING OVERCHARGE AND THERMAL RUNWAY OF HIGH CAPACITY POUCH CELLS

Bing Li [1], Mihit H. Parekh [2], Vilas G. Pol [2], Thomas E. Adams [3], James Fleetwood [4], Casey M. Jones [1], Vikas Tomar [1*]

[1] School of Aeronautics and Astronautics, Purdue University, West Lafayette, IN 47907, USA

[2] Davidson School of Chemical Engineering, Purdue University, West Lafayette, IN 47907, USA

[3] Naval Surface Warfare Center, Crane Division, Crane, IN 47522, USA

[4] Battery Innovation Center, Newberry, IN 47449, USA

*Corresponding author.

Manuscript under preparation.

Abstract

Lithium-ion battery (LIB) failure due to abusive cycling conditions can result in thermal runaway, which calls for reliable real-time battery thermal safety monitoring. In this work, an effective method for LIB thermal runaway detection using resistant temperature detector (RTD) is compared with conventional battery surface temperature measurement. A direct electrode temperature measurement technique based on additive manufacturing enabled application of RTDs for measurement of internal temperature within large capacity Li-ion pouch cells with multi-layer electrodes is used. The miniature RTDs were embedded in a customized electrochemically inactive polymeric substrate for real-time thermal safety monitoring during overcharge abuse. Electrode temperature profiles under different conditions of overcharge (at 1C and 5C rate, charged until battery explosion) were analyzed and mechanisms of heat generation in LIB during overcharge induced thermal runaway was investigated. The internal RTDs detected the onset temperature of solid electrolyte interface (SEI) decomposition ~10 s earlier than the sensors attached on the battery surface. A maximum temperature gradient of ~200 ºC was observed between the electrode and the battery surface during overcharge induced thermal runaway and LIB explosion. In the event of gas generation from solid electrolyte interface decomposition, only the internal RTD was capable of providing accurate electrode temperature reading. By maintaining tight contact with the electrodes, the internal RTDs also captured electrode temperature during the ignition of electrolyte

and flammable gases after the LIB explosion. The effects of cell voltage, charging rate, and battery structure on heat generation and thermal behavior of LIB during the thermal runaway process were studied based on the RTD measurements. It was found that overcharge related heat generation rate was strongly dependent on the current, while SEI decomposition started at certain onset temperature accelerated heat generation abruptly. The internal RTDs also eliminated the dilemma of sensor placement for capturing the maximum temperature within the LIBs.

Keywords: Li-ion batteries, resistance temperature detector, thermal runaway, overcharge, electrode temperature.

4.1 Introduction

Improvements in energy efficiency and reduction in environmental pollution are two major factors driving Li-ion battery (LIB) technology, which has also bolstered the boom of electric vehicles (EVs) (Xiong, Ma, Li, Sun, & Li, 2020). Nowadays, LIBs are widely applied in portable electronic devices, electric vehicles, aircraft, robotics, etc. (B. Li et al., 2019). However, use of LIBs is also invariably associated with safety hazards, including capacity fade (B. Li et al., 2018), dendrite formation (Adams et al., 2018), battery pack imbalance (Love, Virji, Rocheleau, & Swider-Lyons, 2014), etc. Among the LIB safety hazards, preventing thermal runaway is the key scientific challenge, which requires significant mechanistic elucidation. LIB thermal runaway follows a mechanism of chemical chain reactions, during which the heat balance within LIBs is violated and the rising temperature accelerates the exothermic reactions (Feng et al., 2018; Q. Wang et al., 2012). Due to irreversible nature of thermal runaway and associated heat generation (H. Yang, Bang, Amine, & Prakash, 2005), it is crucial to monitor and analyze the development of thermal runaway and related exothermic reactions. Efforts focusing on studying the thermal runaway process can be classified into two categories: theoretical modeling/numerical simulation based analyses (G.-H. Kim, Pesaran, & Spotnitz, 2007; Spotnitz & Franklin, 2003; Q. Wang et al., 2012) and experimental analyses (Leising, Palazzo, Takeuchi, & Takeuchi, 2001a; B. Li et al., 2019; Ohsaki et al., 2005; Saito, Takano, & Negishi, 2001; H. Yang et al., 2005). It is essential to link the models with experimental observations. Overcharge is one of the most critical thermal abuse loading related to the failure of LIBs, as it can result in drastic thermal runaway due to excessive energy stored in the thermally abused LIBs (Feng et al., 2018). There have been numerous analyses of LIB temperature during overcharge and thermal runaway, most of which were accomplished by measuring battery surface temperature (Belov & Yang, 2008; Kallfaß, Hoch, Hilger, & Manke, 2012; Larsson & Mellander, 2014; Leising et al., 2001a; Leising, Palazzo, Takeuchi, & Takeuchi, 2001b; Ye et al., 2016). Thermocouples were used for LIB temperature measurement in these studies. Thermocouples need to be placed on the battery surface (Belov & Yang, 2008; Kallfaß et al., 2012; Larsson & Mellander, 2014; Ye et al., 2016) or sealed with epoxy to be placed within the LIBs (Leising et al., 2001a, 2001b), as they cannot sustain the harsh chemical environment of LIBs. Combination of heat, local stress, and local grain boundary/second phase impurity particle assisted stresses can cause fracture (V. Tomar, 2008a; Vikas Tomar, 2008; V. Tomar, 2008b) leading to loss of efficiency and thermal runaway. Based on the review of

existing work, the current challenges regarding LIB temperature measurement based thermal runway prevention can be summarized as: (1) the temperature measurement method needs to be compatible for different types of LIBs and thermal abuse scenarios due to complex nature of LIB thermal runaway; (2) rapidness of the thermal runaway process requires the temperature sensor to measure electrode temperature in the closest vicinity possible; and (3) the temperature sensor should not interfere LIB operation during regular cycling and initiation of thermal runaway.

In our previous coin cell work, resistance temperature detectors (RTDs) have shown success in direct electrode temperature measurement during the short circuit of LIBs (B. Li et al., 2018; B. Li et al., 2019). In this work, by adjusting this technique for Li-ion pouch cells, RTDs were embedded in pouch cells for monitoring of electrode temperature evolution during overcharge and consequent thermal runaway. The spatial pattern of Li-ion pouch cell heat generation was analyzed with multi-sensor measurements on the battery surface, which verified that the internal RTD was placed at the hot spot on the electrode for optimized temperature monitoring. By comparing the temperature of LIBs overcharged at different charging rates, the effect of current on LIB heat generation was measured.

Mechanisms of heat generation in LIB during overcharge were also studied by analyzing electrode and battery surface temperature comprehensively. The internal RTD provided superior measurement reliability in the event of overcharge abuse of LIB, where rapid temperature change, gas generation, and cell explosion were involved. This technique enabled the monitoring of thermal runaway related safety hazards with improved efficiency and robustness, which remained reliable in LIB explosion.

4.2 Fabrication of RTD Embedded Li-ion Pouch Cells

In this work, the direct sensor-electrode contact ensured reliability of electrode temperature measurement regardless of the environmental vibration, impact, change in battery structure, etc. during LIB service. It also enabled the recoding of electrode temperature during the entire thermal runaway process, including the explosion and firing of the tested LIBs. The gas generation rate in LIB thermal runaway was estimated by monitoring the electrode-battery surface temperature gradient. This temperature-based estimation matched with the theoretical prediction of gas generation rate at different stages of LIB thermal runaway.

For direct temperature measurement of pouch cell electrodes, an RTD embedded substrate was prepared with additive manufacturing of polylactic acid (PLA). The geometry of the PLA substrate was designed according to the electrode dimensions to provide uniform support for the whole electrode surface and ensure the reliable sealing of the pouch cells. With the help of additive manufacturing, the RTD paired well with the PLA substrate and electrode, which ensured tight sensor-electrode contact for accurate temperature monitoring. The RTD was located close to the electrode tab on the PLA substrate (5mm from the edge of electrode material), as it has been shown in the literature that tabs of pouch cells experience the highest temperature during LIB cycling (Belov & Yang, 2008; Martiny, 2018). The structural stability and temperature measuring reliability of the RTD embedded PLA substrate in LIBs were analyzed in our previous coin cell study (B. Li et al., 2019). Details of sensor embedding and cell assembly are shown in Fig. 4.1 (a, b):

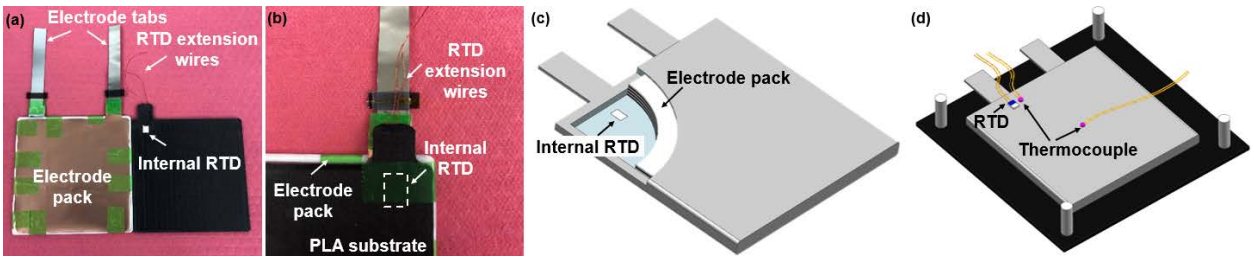

Figure 4.1. (a). Pouch cell electrode pack and RTD embedded substrate; (b). Assembly condition of electrode pack and RTD embedded substrate; (c). The layout of RTD embedded pouch cell and (d). Overcharge and temperature measurement system setup.

In this work, Polypropylene (PP) membrane with a thickness of 25 µm by Targray was selected as the separator material. Graphite anode (Superior Graphite) and $LiNi_{0.5}Co_{0.2}Mn_{0.3}O_2$ (NCM523) by BASF were selected as the active materials for the anode and cathode, respectively. The electrolyte 1M $LiPF_6$ in 3/7 EC/EMC (v/v) was used. Details on the electrodes are provided in Table 4.1:

Table 4.1. Electrode composition and properties.

	Anode	Cathode
Substrate	Cu, 10 μm thickness	Al, 12 μm thickness
Current conductor	Super C65 carbon black by C-Energy	Super C65 carbon black by C-Energy
Binder	HSV900 PVDF by Arkema	HSV900 PVDF by Arkema
Weight ratio (active material: current conductor: binder)	94: 2.5: 3.5 w/w	94: 2.5: 3.5 w/w
Average weight loading	11.5 mg/cm^2	18.1 mg/cm^2
Area with active material	6.8 cm*6.8 cm	6.6 cm*6.6 cm
Electrode thickness	80 μm	67 μm
Number of electrodes	4 double layers, 2 single layers	5 double layers

The RTD embedded substrate was placed beneath the electrode stack facing the current collector of the single side anode as shown in Fig. 4.1 (c). Such an arrangement allows local interface viscosity control and reduced the possibility of fracture significantly (D. Dubey & Tomar, 2008; D. K. Dubey & Tomar, 2009; Tao Qu, Devendra Verma, Milad Alucozai, & Vikas Tomar, 2015). Two pouch cells with internal RTDs were fabricated by sealing the electrode pack and RTD embedded substrate together with a pressure of 5 psi in a dry lab with controlled humidity of <1%. A pocket for excess volume was attached to the cells during fabrication to hold gas generated during the formation cycles. Three constant current-constant voltage (CC-CV) formation cycles were applied to allow for solid electrolyte interface (SEI) formation, as SEI decomposition is a main heat source in LIB thermal runaway (Feng et al., 2018). The formation was carried out in a 25 °C chamber, under 5 psi of stack pressure based on a 4-spring steel fixture visible in Fig. 4.1 and controlled via an Arbin test station. One of the cells (cell #1) had the pocket attached during the overcharge test, while the other cell (cell #2) had the pocket removed after formation cycles and was re-sealed before the overcharge test. Details on the formation cycles and pouch cell performance are provided in Table 4.2 and Fig. 4.2.

Table 4.2.Specification of formation cycle and preparation cycle for overcharge test.

Upper cut-off voltage	4.2 V	Charging rate, formation cycle 2	C/10
Lower cut-off voltage	2.5 V	Discharging rate, formation cycle 2	C/10
Intermediate rest period	2 min	Charging rate, formation cycle 3	C/10
Charging rate, formation cycle 1	C/20	Discharging rate, formation cycle 3	C/10
Discharging rate, formation cycle 1	C/20	Charging rate, preparation cycle	C/5

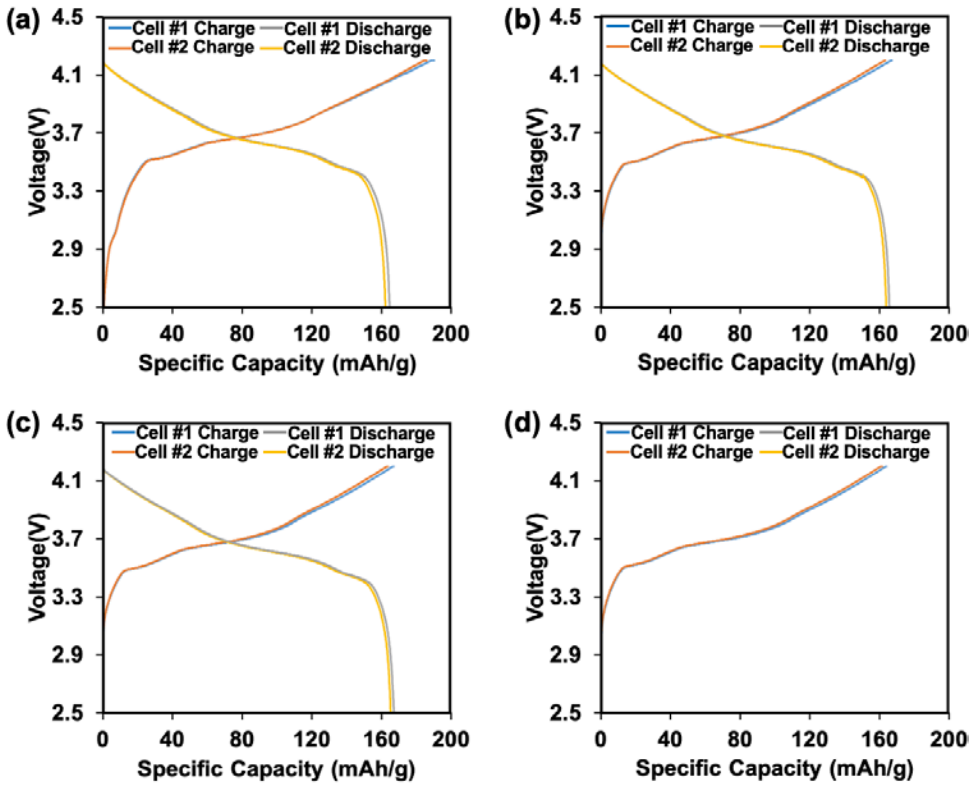

Figure 4.2. Performance of cell #1 and cell #2 in (a): Formation cycle 1; (b): Formation cycle 2; (c): Formation cycle 3 and (d): Preparation cycle for overcharge test.

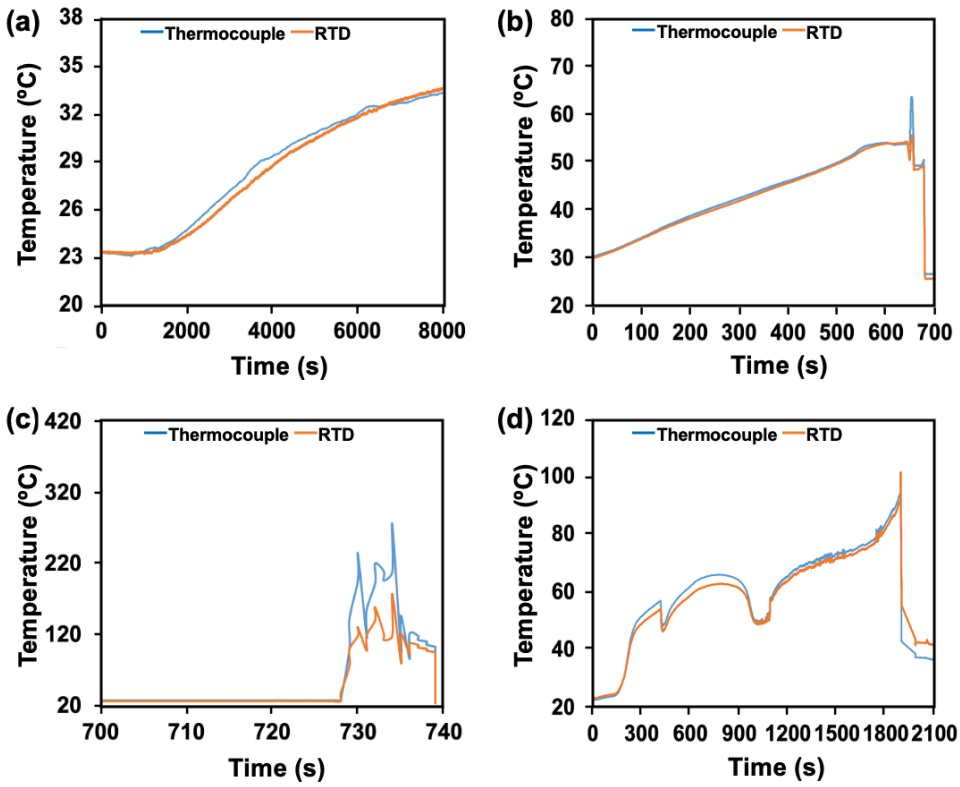

Figure 4.3. External thermocouple and RTD reading Comparison. (a-c): Cell #1 and (d): Cell #2.

4.3 Overcharge Test and Temperature Measurement

After the formation cycles, the two LIBs were CC charged at 5C rate to 4.2 V. The experiment was then carried out in a 1200 ft^2 reinforced concrete test cell equipped with isolated ventilation and fire control facilities to prevent potential safety threats. The overcharge test was monitored with a video camera and controlled remotely with custom LabVIEW-based monitoring and control software linked with an AeroVironment ABC-170 test station. To analyze the effect of charging rate on heat generation within the pouch cell, cell #1 was charged at 1C rate up to 5.4 V and was then charged at 5C rate until the explosion. Cell #2 was charged at 5C rate constantly until cell explosion. Two thermocouples and one RTD were attached to the surface of each pouch cell, and one RTD was embedded on the PLA substrate within the cells. One of the thermocouples was located at the center of the cell; the other thermocouple and the external RTD were placed near the battery tab (on the top of the internal RTD) as shown in Fig. 4.1 (c, d). The cells were then clamped between two rectangular stainless-steel plates for the overcharge test. Temperature measured by the external RTD and thermocouple attached to the battery tab were compared in Fig.

4.3 and the two sensors presented comparable measurements of battery surface temperature. Both cells experienced thermal runaway at the end of the overcharge test and the conditions of LIB leakage, smoking and firing were recorded by a video camera as shown in Fig. 4.4.

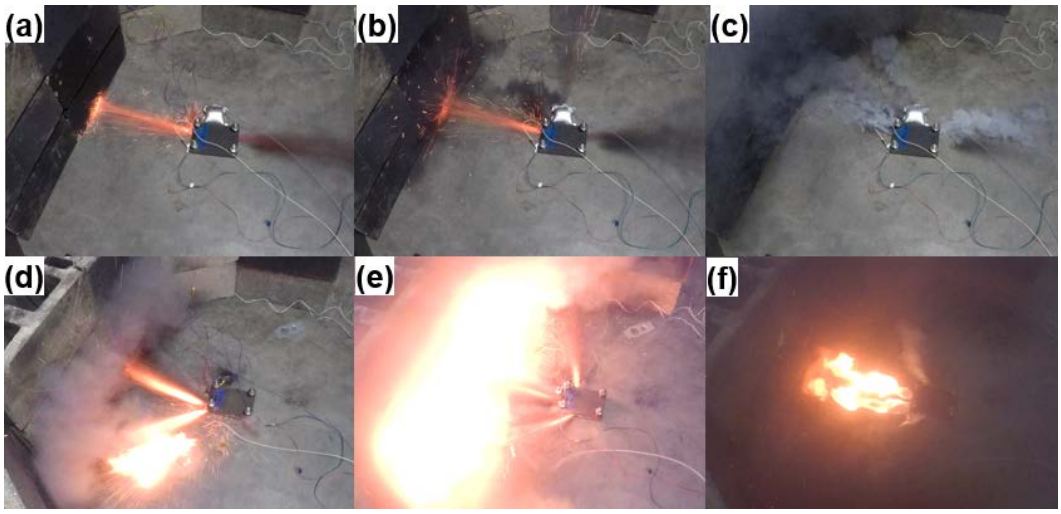

Figure 4.4. Cell #1: (a). Initiation of explosion: cell leaked and emitted sparks, (b). Development of explosion: sparks and smoke released from the cell, (c). Lateral stage of explosion: continuous smoking. Cell #2: (d). Initiation of explosion: cell leaked and jetted flames, (e). Development of explosion: jet flame developed, (f): Lateral stage of explosion: continuous burning.

4.4 Comparison of Battery Surface Temperature and Electrode Temperature

Cell voltage, battery surface temperature (measured by the external RTD attached on the tab), electrode temperature (measured by the internal RTD), and their changing rates for cell #1 in the overcharge test are shown in Fig. 4.5. The temperature changing rate was calculated with first order fitting of temperature data. For an overcharge at the 1C rate, the temperature increase rate was calculated for 5-minute intervals. For an overcharge at the 5C rate, the temperature increasing rate was calculated over every 10 s before the external RTD detected an abrupt temperature rise around t=728 s. After t=728 s, the temperature increasing rate was calculated every second to provide better resolution during periods of rapid temperature changes.

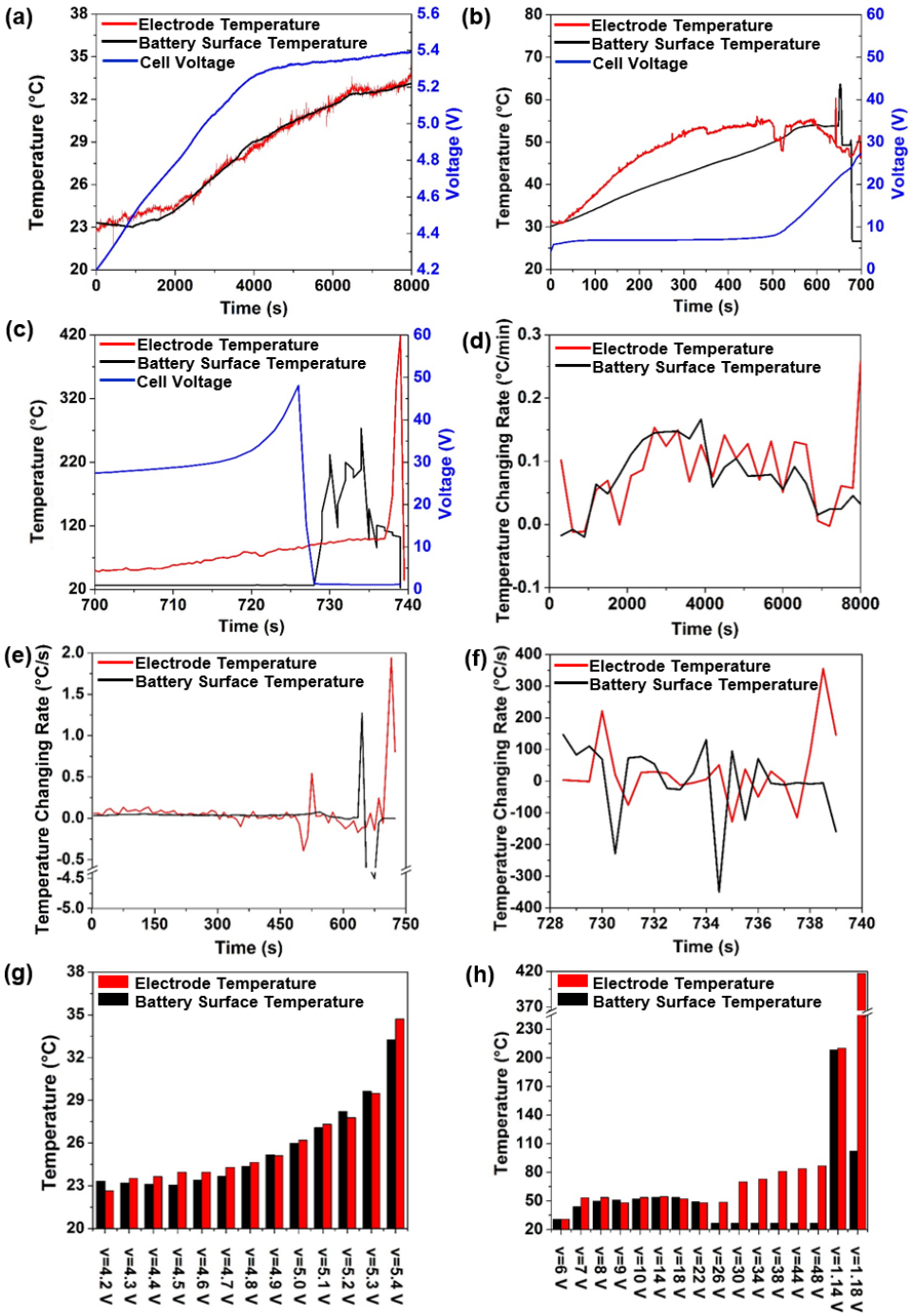

Figure 4.5. Temperature and voltage of cell #1 during (a). 1C rate overcharge up to 5.4 V, (b). 5C rate overcharge and (c). 5C rate overcharge before thermal runaway event. Temperature changing rate of cell #1 during (d). 1C rate overcharge up to 5.4 V, (e). 5C rate overcharge, and (f). 5C rate overcharge before the thermal runaway event. Comparison of battery surface and electrode temperature during: (g). 1C rate overcharge up to 5.4 V and (h). 5C rate overcharge until the thermal runaway event (V= 1.14 V and 1.18 V: after thermal runaway).

The test conditions were chosen to correspond to right statistical insights within the limits of the difficult thermal runaway experiments (Mejía-Rodríguez, Renaud, & Tomar, 2008). It can be observed that electrode and battery surface temperature of cell #1 followed the same trends when the battery was overcharged at the 1C rate to 5.4 V. The largest difference between the electrode and battery surface temperatures was minimal, only 0.95°C. Thus, the external RTD attached to the battery surface reported the electrode temperature reliably during this period except for failing to reflect some subtle and transient temperature changes. This indicates that heat generated at the electrodes could transfer to the battery surface effectively under mild overcharge abusing conditions. The low thermal resistance in the thickness direction of the cell was expected due to the pressure applied during cell fabrication to ensure tight contact between the electrode and laminate case. During regular operation and mild overcharge conditions of LIB where the ordinary insertion reaction is dominant, the most important heating effect is associated with Joule heating and electrode over potential; effects of mixing and phase change can be neglected (Rao & Newman, 1997; W. Wu et al., 2019). At low temperatures exhibited by LIBs during normal operation, no significant gas generation from electrode-electrolyte reaction or electrolyte decomposition was expected (Feng et al., 2018). Thus, the laminate film remains in contact with the electrodes and battery surface temperature can be used for electrode temperature estimation during regular cycling and mild overcharge abusing of LIBs.

When the charging rate was elevated to 5C, the difference between electrode and battery surface temperature started to build up slowly before the electrode temperature reached 60°C as shown in Fig. 4.5 (b, h). At this point, the heat generated within the cell could no longer be transferred effectively to the battery surface, which could originate from two aspects: (1) heat generation rate increased dramatically so that the effect of pouch cell thermal resistance could not be ignored; and (2) there were changes in pouch cell structure that caused the thermal resistance to increase. Leising et al. (Leising et al., 2001a) and Saito et al. (Saito et al., 2001) showed that Joule heat was one major heat source during overcharge, which rises dramatically with current increases. As for the thermal resistance, tight contact between the electrode and laminate film case was generated in the well-controlled LIB fabrication, which was also verified by the limited temperature difference between the electrode and battery surface during 1C rate overcharge as shown in Fig. 4.5 (a, g). Thus, high thermal resistance was only expected after gas accumulation within the cell that impaired the contact between the electrodes and laminate case. Gas generation

occurs from the decomposition of solid electrolyte interface (SEI) (Belov & Yang, 2008) on the graphitic anode surface as well as reactions between the electrolyte and overcharged electrodes (Ohsaki et al., 2005). The onset temperature for the decomposition of SEI on graphite anodes is typically around 57°C (Feng et al., 2018), while reactions between overcharged electrodes and electrolyte generally accelerate at 60°C (Ohsaki et al., 2005). The temperature of cell #1 was below 57°C at the beginning of 5C rate overcharge and rapid gas generation was not expected at this stage. Besides, the pocket of cell #1 would accommodate the extra volume at the initial stage of gas generation. Since the building-up temperature difference between the battery surface and electrode presented immediately after charging current was increased, the temperature gradient should be mostly contributed to the rapid Joule heat generation at this stage.

At the beginning of 5C rate overcharge of cell #1, the difference in temperature increasing rate of the electrode and battery surface remained limited as shown in Fig. 4.5 (e). Thus, the possibility of applying a correcting function to the battery surface temperature for electrode temperature estimation needs to be discussed. This correcting function needs to take account of the changes in electrode heat generating rate and battery structure throughout the overcharge process. LIB heat generation rate q can be written as (Rao & Newman, 1997):

$$q = I\left(V - \sum_{l} U_{l,avg}\right) + \sum_{l} I_l \cdot T^2 \cdot \left(d\frac{\frac{U_{l,avg}}{T}}{dT}\right) + MC_p^m\frac{dT}{dt} + q_{mix} + q_{phase} \qquad (4.1)$$

where I is the cell current, V is the cell potential, $U_{l,avg}$ is the open circuit potential of reaction l, T is the cell temperature, M is cell mass, C_p^m is mean heat capacity, q_{mix} is heat related with mixing and q_{phase} is heat related with phase change. C_p^m, q_{mix} and q_{phase} are difficult to keep track of during the overcharge process, especially for high voltage and high C rate overcharge where gas generation is involved. Also, since there are inevitable manufacturing differences among the cells, this correcting function is dependent on the assembly and cycling condition of individual cells, including their charging current, internal resistance, change of cell structure, etc. It has also been noticed that imbalance within the battery pack in terms of cell impedance, voltage, etc., is promoted over cycling and abusing such as overcharge (Carter, Huhman, Love, & Zenyuk, 2018; Love et al., 2014). This will further change the temperature correcting function over time. Thus, it is impractical to apply external temperature sensor-based measurement with correcting

function for electrode temperature monitoring in high C rate applications even before thermal runaway initiates.

After the electrode temperature reached the typical onset temperature of 57-60°C for SEI decomposition (Feng et al., 2018) and electrode-electrolyte reaction (Ohsaki et al., 2005), the thermal runaway process initiated in cell #1. Gas generation accelerated and impaired the contact between the electrode and laminate film case. This was followed by an abrupt decrease in battery surface temperature, which denoted a change in thermal resistance of cell #1. CT scanning of the abused LIBs has shown that gas generation could result in a local increase of gap distance between the electrodes and deformation in the central part of the electrodes (Bond, Zhou, & Cutler, 2017; Yufit et al., 2011). These structural changes lead to an increase of LIB thermal resistance, which explain the temperature gradient increase in the thickness direction of cell #1 after SEI decomposition and resultant gas generation. SEI decomposition and reaction between electrode and electrolyte generated a high concentration of H_2, CH_4, C_2H_6, and CO (Ohsaki et al., 2005). This mixture of flammable gases was observed to be stable within the cell initially as oxygen released by cathode decomposition could be insufficient for combustion (Feng et al., 2018). Around t=728 s the RTDs detected a sudden temperature increase of cell #1. This should be contributed to the accelerated decomposition of SEI, which is highly exothermic and expected to occur around 80-100°C (Richard & Dahn, 1999; Spotnitz & Franklin, 2003). An estimation of the SEI decomposition rate can be made with the Arrhenius equation (Hatchard, MacNeil, Basu, & Dahn, 2001):

$$\frac{d_{SEI}^{d}}{dt} = A_{SEI} \cdot c_{SEI} \cdot \exp\left(-\frac{E_{a,SEI}}{R \cdot T}\right), T > T_{SEI} \tag{4.2}$$

where $\frac{d_{SEI}^{d}}{dt}$ is the rate of SEI decomposition, A_{SEI} is the pre-exponential factor, c_{SEI} is the normalized concentration of the SEI, R is the ideal gas constant, $8.314\ J \cdot mol \cdot K^{-1}$, T is the electrode temperature and T_{SEI} is the onset temperature of SEI decomposition. An estimation of $E_{a,SEI}$ is provided as $1.3508 \cdot 10^5\ J \cdot mol^{-1}$ (G.-H. Kim et al., 2007). Since SEI decomposition is of limited rate before the cell reaching 80 ℃ (Feng et al., 2018), A_{SEI} and c_{SEI} are assumed to remain constant before reaching 80℃. A comparison of SEI decomposition rate at 57 ℃ and 80 ℃ can be obtained as:

$$\frac{d^{d}_{SEI,80℃}}{d^{d}_{SEI,57℃}} = \frac{\exp(-\frac{E_{a,SEI}}{R \cdot 353.15K})}{\exp(-\frac{E_{a,SEI}}{R \cdot 330.15K})} \approx 4.79 \quad (4.3)$$

Since the SEI decomposition rate at 80°C rose almost 5 times compared to 57°C, gas accumulation and heat generation rates related to SEI decomposition increased correspondingly. As a result, shortly after the cell reached 80 ℃, severe gas accumulation resulting in electrolyte leakage. Due to the high pressure from large amounts of gas generated, cell #1 ruptured and released ignited gases and electrolyte. Condition of leaking, mass ejection, and firing during the explosion of cell #1 is provided in Fig. 4.4 (a-c). The cell explosion ripped off the laminate case at the tab region causing the external RTD to miss temperature measurements during the peak of thermal runaway. Thus, temperature measurement by external temperature sensors are not reliable during the event of thermal runaway.

Voltage, surface temperature (RTD located externally on the tab), and electrode temperature (internal RTD), were measured and recorded for cell #2 and their changing rates during overcharge test at 5C rate are shown in Fig. 4.6. The temperature changing rate was calculated over every 10 s before an abrupt temperature rise was detected (around t=1885 s). The temperature changing rate was calculated at 1 s rate between t=1885 s and t=1895 s to better describe the dramatic temperature change.

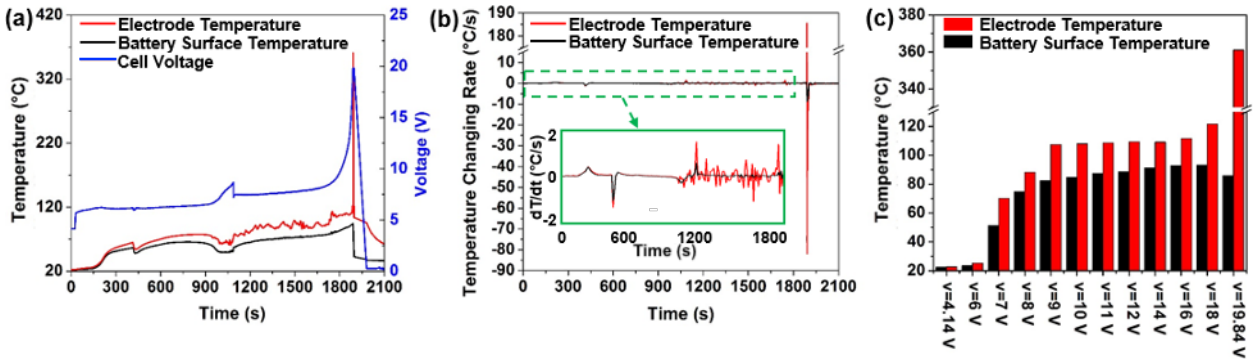

Figure 4.6. (a). Battery temperature and voltage of cell #2 under 5C rate charge until explosion, (b). Temperature changing rate of cell #2, and (c). Comparison of surface and electrode temperature of cell #2.

In comparison to the overcharge of cell #1 at the 1C rate, the temperature difference between the electrode and battery surface of cell #2 started to build up immediately regardless of the cell voltage. Since the initial temperature of cell #2 was much lower for SEI decomposition and reactions between electrode and electrolyte (Feng et al., 2018; Ohsaki et al., 2005), the temperature gradient should drive solely from the rapid Joule heat generation associated with the high charging current.

Similar to cell #1, the internal RTD in cell #2 captured the peak electrode temperature during the explosion caused by overcharge, while the external RTD did not. Since there was no free volume for internal gas to accumulate inside the cell #2, it exploded rapidly from SEI decomposition and gas generation. The amount of ejecta released was minimal due to low rupture pressure of the cell design. Ambient oxygen entered the cell resulting in combustion of electrolyte and electrode material as shown in Fig. 4.4 (e, f). On the contrary, cell #1 emitted smoke and vapor after the explosion as most of the electrolyte was consumed in the electrolyte decomposition and reactions with the electrode. The temperature profiles during overcharge of cell #1 (1C rate) and cell #2 (5C rate) differed in that there was no fluctuation in battery surface temperature in cell #2. This confirmed that the amount of gas generated in cell #2 was limited before cell explosion, and there was no significant change in the thermal resistance of cell #2 in its thickness direction. Although the laminate film case remained in good contact with the electrode, external temperature sensors still failed to measure during the thermal runaway event when the laminate case was detached from the electrode. Moreover, the amount of temperature difference between the electrode and battery surface was due to the high Joule heat generation rate before the explosion. Thus, surface temperature measurements are not reliable to safely monitor cell temperature when high current, high voltage, or gas generation is present during overcharge. Thus, it is necessary to monitor the electrode temperature internally with RTDs for optimum sensing and control. The use of multiple internal RTDs could provide measurements of the temperature contour of the electrode to detect hot spots and non-uniform thermal distributions to improve safety risks of LIBs. In this work, battery surface temperature was compared at the tab and inside the cell near the electrode. Detailed analysis of the electrode temperature at different locations is currently being studied and is not included in this manuscript.

4.5 Comparison of Battery Surface Temperature Measured at Different Locations

Although there have been numerous analyses on the thermal distribution and local areas of higher temperature LIBs during normal operation, very little information exists on the temperature distribution during electrical abuse such as overcharge that leads to thermal runaway. The temperature recorded by two thermocouples attached to the battery surface, one on the center of the cell and the other on the tab, are compared in Fig. 4.7. A comparison of thermocouple and RTD measurements is provided in Fig. 4.3.

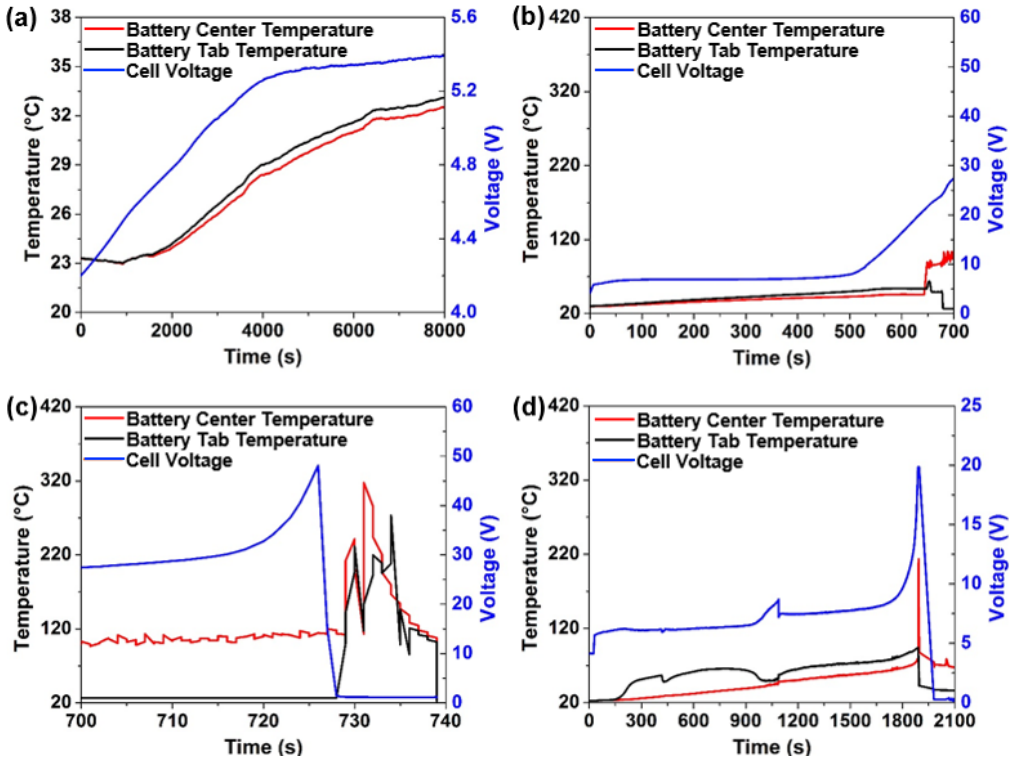

Figure 4.7. Voltage and battery surface temperature measured at the battery center and the tab during: (a). 1C rate overcharge of cell #1 up to 5.4 V; (b). 5C rate overcharge of cell #1; (c). 5C rate overcharge of cell #1 before the explosion; (d). 5C rate overcharge of cell #2 until the explosion.

From the overcharge event on cell #1, it can be found that the temperature of the tab was higher than the temperature of the cell center before severe gas accumulation. This difference can be attributed to high local current density at the tab region which is the preferred location when no

gas accumulation occurs (X. Zhang, Chang, Shen, & Xiang, 2017)., This indicates that the tab region is preferred for temperature monitoring of LIBs with no gas accumulation. When the gas accumulates from thermal runaway, the accuracy of battery surface temperature measurement at the tab of pouch cells was degraded, as the edges of the cells were less constrained by the clamp compared to the center of the cells. The alignment of temperature sensors and wires at the tabs could also influence the constraint of the clamps when gas accumulated in the cell. In this case, the temperature measured on the surface in the middle of the cell exhibited the most accurate readings. The same observation was made on cell #2, where the temperature measured at the tab was always higher than the center except at the onset of cell rupture. Therefore, when monitoring the surface temperature of pouch cells, the best location to sense the temperature is at the tab during normal operation and at the initial stage of thermal runaway. After the onset of thermal runaway, the external sensor located in the middle or center of the cell is the best choice for battery surface measurement due to expansion from gas generation and eventual explosion. This dilemma of sensor placement can be eliminated by employing an internal RTD for direct electrode temperature measurement. The internal RTD was capable of providing more stable monitoring of electrode temperature during the initial stage of LIB thermal runaway compared to the RTD and thermocouple placed on the battery surface. During the conclusion of the thermal runaway event when the cell exploded, the internal RTD remained in contact with the electrode and provided continuous temperature monitoring. Thus, the internal RTD embedded within the pouch cell with 3D printing can provide a complete solution for pouch cell temperature monitoring during regular operation, mild abuse of overcharge, and violent battery failure such as thermal runaway.

4.6 Conclusion

In this work, RTDs were embedded on a PLA substrate next to the electrode in Li-ion pouch cells to accurately measure electrode temperature during overcharge induced thermal runaway. Overcharging commonly occurs in batteries, especially aged ones, constructed in a combination of cells connected in series and/or parallel, but can also occur using improper charge settings outside the manufacturer specification values. Thermal behavior of Li-ion pouch cells under different conditions of overcharge were analyzed using two techniques, a conventional surface temperature measurements and a direct electrode temperature measurement with internal RTDs. The embedded RTD in the cell was able to capture the thermal behavior of the electrodes

from the onset to thermal runaway to the catastrophic ending. By comparing the performance of LIBs with and without pocket in the overcharge test, volume and pressure related effect on LIB behavior during thermal runaway was analyzed. The evolution of heat generation mechanism in LIBs during overcharge and thermal runaway was studied with theoretical analysis on the Joule heat generation rate and on SEI decomposition, and compared with measured surface and electrode temperature. The origin of the temperature difference between the electrode and battery surface under different charge cycle abuse conditions was analyzed. Such analyses helped to capture LIB structure and thermal resistance change. During battery surface temperature measurements, issue of effective sensor arrangements for efficient temperature monitoring can be resolved by applying internal sensors for direct electrode temperature monitoring. By applying the internal RTDs, effective monitoring of electrode temperature during regular cycling, overcharge as well as the explosion of LIBs can be achieved. The internal RTD detected the onset temperature of SEI decomposition ~10 s before the external RTD and reported a ~200 ℃ temperature difference between the electrode and battery during the thermal runaway event. RTDs can provide an early warning to thermal runaway onset and prevent thermal runaway in a reliable manner.

5. SENSOR BASED IN-OPERANDO LITHIUM-ION BATTERY MONITORING IN DYNAMIC SERVICE ENVIRONMENT

Bing Li [1], Casey M. Jones [1], Thomas E. Adams [2], Vikas Tomar [1,*]

[1] School of Aeronautics and Astronautics, Purdue University, West Lafayette, IN 47907, USA

[2] Naval Surface Warfare Center, Crane Division, Crane, IN 47522, USA

[*] Corresponding Author.

Manuscript under preparation.

Abstract

In this work, a dynamic testing platform to analyze lithium-ion battery (LIB) performance degradation and safety during in-service vibration and impacts is presented. The LIBs are cycled until end of life (EOL) under various dynamic conditions, providing in-operando battery performance examination. A sensor network constructed consisting of a resistance temperature detector (RTD), an accelerometer, an eddy current sensor and a shunt resistor is incorporated into the setup. Mechanisms of LIB capacity fade, temperature rise, and deformation from cycling in representative dynamic environments are analyzed and compared with results from theoretical analyses as well as with electrode structure evaluation. The sensor network identifies critical periods with high heat generation and stress accumulation rates. By comparing single cell and battery pack performances, complex effects of examined boundary conditions on LIB heat generation are analyzed. Using the sensor network, an approach to identify critical cell(s) with the highest risk of safety hazards without the need for electrochemical modeling is presented. Raman spectroscopy analyses, SEM imaging, and electrochemical impedance spectroscopy (EIS) analyses are also applied to support the observations.

Key words: lithium-ion battery, dynamic load, sensor network, temperature, stress, thermal runaway.

5.1 Introduction

Transition to renewable energy sources such as solar and wind mandates the use of energy storage technologies based on lithium-ion batteries (LIBs) for high demand periods and load leveling. Despite the technology maturity and high energy density offered by LIBs, safety hazards and catastrophic failure of LIBs continue to be the biggest challenge. Based on the statistics by Williard et al. (Nicholas Williard et al., 2013), seven battery failures occurred on Boeing 787 Dreamliners between December 2012 and January 2013, where one severe LIB-related fire incident resulted in a large investigation by the National Transportation Safety Board (National Transportation Safety Board, 2018a, 2018b). The probability of reliable LIB performance decreases over battery cycle-life. Williard et al. (Nick Williard, He, Osterman, & Pecht, 2012) analyzed the cycling performance of 16 commercial lithium-ion pouch cells where 12.5% of these cells exhibited capacity fade larger than 20% before reaching the typical service life of 500 cycles. Such a variation was associated with in-operando dynamic load associated electrode damage. This information has not been considered in current testing standards for LIBs. Many researchers argue that applying environmental dynamic loads, namely vibration and impact loading, can lead to damage of LIB electrodes and loss of battery structure integrity (Adams et al., 2018; Brand et al., 2015; Xia, Wierzbicki, Sahraei, & Zhang, 2014). Although environmental tests are required in numerous battery testing standards (Doughty, 2010; Naval Ordnance Safety and Security Activity, 2010), those are generally applied when batteries are not under operational conditions or being charged. It is, therefore, necessary to carry out in-operando battery performance analysis over extended cycling when in-operando dynamic loading conditions are imposed in order to determine the long-term effect of operational dynamic loads on LIBs.

Sensors provide valuable information in analyzing cell/battery performance. Zhang et al. (G. Zhang et al., 2015) embedded a T-type thermocouple inside an 18650 LIB to measure electrode temperature and provide reaction temperature sensing control. In a test with an intentional trigger short, the onset temperature of thermal runaway at 80 ºC was measured by an internal thermocouple and was used to stop the test. The corresponding skin temperature of the cell only reached 50 ºC. Therefore, the internal thermocouple provided an early warning detection (G. Zhang et al., 2015). In our previous work, internal resistance temperature detectors (RTDs) were applied for thermal runaway detection. The thermal runaway detecting efficiency of the RTDs was more than 10 times faster than surface temperature measurements such as infrared camera imaging

(B. Li et al., 2019). In this work, a resistance temperature detector, an accelerometer, an eddy current sensor, and a shunt resistor were used to form a sensor network to provide comprehensive monitoring of in-operando battery service conditions and their influence on LIB pack failure. Battery performance in a dynamic service environment, including capacity change, temperature rise, and deformation, were analyzed with sensor measurements as well as using conventional electrochemical methods. The analyses and comparison elucidate a possibility that by examining real-time battery performance with a sensor network such as that given in this work, battery failure leading to capacity loss, thermal runaway, and catastrophic failure can be detected efficiently.

5.2 Design of Dynamic Aging Test

Dynamic loads, including vibration and impact, are common in the transportation and service of LIBs (B. Li et al., 2018). The enduring vibrational input can result in reduced service life, or the occurrence of catastrophic failure of LIBs through fatigue cracking and work hardening of battery materials (J. Hooper et al., 2016). To address the concern over vibration related battery degradation and failure, vibrating tests are proposed in numerous LIB safety certification programs. These tests are listed in Table 5.1.

From the testing standard comparison in Table 5.1, it can be noticed that LIB vibration tests are typically accomplished with sinusoidal vibration cycling. The tests generally cover the frequency range of 10-200 Hz and acceleration range of 1-2 g. To verify the effectiveness of the vibration frequency used in LIB testing, Hooper et al. (J. M. Hooper & Marco, 2014) used an accelerometer to characterize the vibration profile experienced by LIB packs in electric vehicles during the vehicle operation under various road conditions. Their results indicated that most vibration energy peaks were concentrated within the frequency range of 7-40 Hz, which could be well captured by the standards listed in Table 5.1.

Table 5.1. Mechanical vibration tests in safety testing standards for Lithium-ion batteries.

Standard Name	Type of vibration	Frequency domain	Acceleration domain	Testing duration
UN 38.3 T4 (Europe, 2015)	Sinusoidal	7-200 Hz	1-8 g	3 h
SAND2005-3123 (Daniel H. Doughty, 2005)	Sinusoidal	10-190 Hz	0.75-3 g	12 h
SAE J2380 (International, 2013)	Sinusoidal	10-200 Hz	0.75 -1.9 g	13.6-92.6 h
NAVSEA 9310 (Naval Ordnance Safety and Security Activity, 2010) *	Sinusoidal	7-200 Hz	1-8 g	3 h

Note: All LIBs to be transported and used in naval application should comply with UN 38.3(Naval Ordnance Safety and Security Activity, 2010).

A vibration test setup to emulate in-operando LIB operation was developed based on the Naval standard NAVSEA 9310 (Naval Ordnance Safety and Security Activity, 2010). In the beginning, mid-range vibration frequency of 18 Hz and acceleration of 1 g were selected (J. Hooper et al., 2016). In most testing standards, including NAVSEA 9310 and UN 38.3 (Doughty, 2010; Naval Ordnance Safety and Security Activity, 2010), vibration is applied to electrically disconnected LIBs and the go/no-go examination is performed after the test. This contradicts the operating conditions of LIBs, where vibration is commonly experienced in-operando during battery service and can be one of the main origins of battery degradation (Brand et al., 2015). Testing the LIBs in-operando is a key advancement offered in this work. Details on the tested LIBs are provided in Table 5.2.

In this work, three pouch cells (by AA Portable Power Corp.) were cycled under NAVSEA 9310 standard based vibrational loads until their end of life (EOL) of 500 cycles. Two of these cells were connected in parallel to form a 2-cell pack. The LIBs were clamped onto an electromagnetic shaker (by The Modal Shop Inc.) with a cell holder prepared with additive manufacturing of polylactic acid (PLA). Acceleration of vibration was monitored by an accelerometer (by PCB Piezotronics). The manufacturer specified maximum allowable current of

170 mA was applied for continuous constant current LIB cycling. To evaluate the battery temperature rise and deformation over cycling in a vibrational environment, Pt-1000 RTDs (by Omega Engineering) and an eddy current sensor (by Lion Precision) were embedded onto the cell holder during the additive manufacturing process. The RTD can help to detect short circuit and thermal runaway based on our previous study [9]. LIB electrode temperature measurement has been shown to be related with accelerated electrode failure (J. Choi et al., 2014). The voltage and current of LIBs under test were monitored with battery management chips (by Quawin Electronics). Details of the vibration testing setup are provided in Fig. 5.1 (a). All wires connected to the LIBs were tied and attached to the ground for minimization of the payload generated by the wires. For the convenience of discussion, the graphite electrode is referred to as the anode and the $LiCoO_2$ electrode is referred to as the cathode in this work.

In this work, three pouch cells (by AA Portable Power Corp.) were cycled under NAVSEA 9310 standard based vibrational loads until their end of life (EOL) of 500 cycles. Two of these cells were connected in parallel to form a 2-cell pack. The LIBs were clamped onto an electromagnetic shaker (by The Modal Shop Inc.) with a cell holder prepared with additive manufacturing of polylactic acid (PLA). Acceleration of vibration was monitored by an accelerometer (by PCB Piezotronics). The manufacturer specified maximum allowable current of 170 mA was applied for continuous constant current LIB cycling. To evaluate the battery temperature rise and deformation over cycling in a vibrational environment, Pt-1000 RTDs (by Omega Engineering) and an eddy current sensor (by Lion Precision) were embedded onto the cell holder during the additive manufacturing process. The RTD can help to detect short circuit and thermal runaway based on our previous study (B. Li et al., 2018). LIB electrode temperature measurement has been shown to be related with accelerated electrode failure (J. Choi et al., 2014; Verma & Tomar, 2015). The voltage and current of LIBs under test were monitored with battery management chips (by Quawin Electronics). Details of the vibration testing setup are provided in Fig. 5.1 (a). All wires connected to the LIBs were tied and attached to the ground for minimization of the payload generated by the wires. For the convenience of discussion, the graphite electrode is referred to as the anode and the $LiCoO_2$ electrode is referred to as the cathode in this work.

Table 5.2.Specification of tested Lithium-ion battery.

Battery dimension	20.5 mm (l)*18.5 mm (w)*4.5 mm (h)	Separator material	Polypropylene
Battery weight	2.8 g	Separator dimension	570 mm (l)*21 mm (w)
Rated capacity (at 0.2C rate)	130 mAh	Separator thickness	25 μm
Anode active material	Graphite	Cathode active material	$LiCoO_2$
Anode current collector material	Copper	Cathode current collector material	Aluminum
Anode length	170 mm double sides, 41 mm single side	Cathode length	170 mm double sides, 40 mm single side
Anode width	19.5 mm	Cathode width	19 mm
Anode coating thickness (single side)	73 μm	Cathode coating thickness (single side)	54 μm
Anode current collector thickness	10 μm	Cathode current collector thickness	20 μm

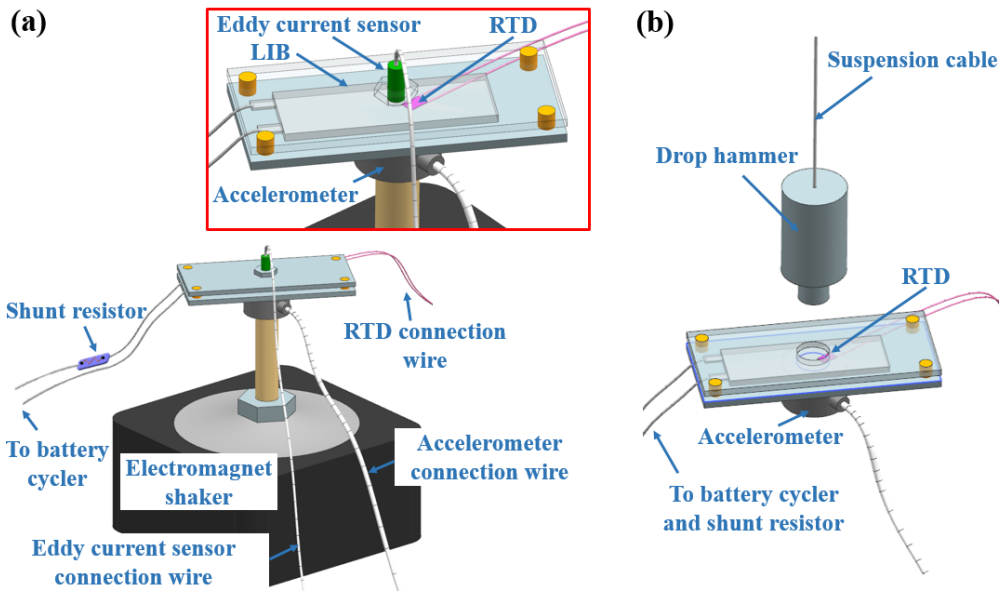

Figure 5.1. In-operando testing platform for LIBs, (a): Setup for in-operando vibration test, and (b): Setup for in-operando impact test analysis.

Impact is another typical dynamic load in LIB transportation and operation (Brand et al., 2015), and impact testing is proposed in each of the LIB safety standards listed in Table 5.1. The specifications of impact tests in these safety standards are listed in Table 5.3. In Table 5.3, the impact load for LIB testing can be defined by the peak acceleration, duration, and type of impact. The highest impact acceleration listed in Table 5.3 is 150 g in NAVSEA 9310 and UN 38.3 standards. Acceleration of 150 g is also the highest allowed peak acceleration of helmets for protection of warfighters against head injury (Slobodnik, 1979). Accordingly, the LIBs sustainable under impact with 150 g of acceleration are expected to be operational and immune to catastrophic failures under the condition when personal safety is secured. In this study, the impact acceleration of 150 g was adopted to analyze the robustness of LIBs under the most critical dynamic environment they may encounter. Since half-sinusoidal impact spectrums rarely occur, a random shock spectrum was used to represent the dynamic environment experienced by LIBs (B. Li et al., 2018). Random impact spectrums simulate what LIBs encounter in transportation and operation through land sea, and air, such as rough pavement, pot holes, wind pressure and turbulence, waves, etc. (Elbeheiry & Karnopp, 1996).

Table 5.3. Mechanical impact tests in Lithium-ion battery safety testing standards.

Standard	Application	Type of impact	Peak acceleration	Impact duration	Repetition
UN 38.3 T4 (Europe, 2015)	Transportation of LIBs	Half sinusoidal shock	150 g	6 ms	3
SAND2005-3123 (Daniel H. Doughty, 2005)	Electric hybrid vehicle	Half sinusoidal shock	25-35 g	30-60 ms	3
SAE J2380 (International, 2013)	Electric and hybrid electric vehicle	Half sinusoidal shock	25g	15ms	3
NAVSEA 9310 (Naval Ordnance Safety and Security Activity, 2010) *	LIBs for Navy and marine applications	Half sinusoidal shock	150 g	6 ms	3

Note: All LIBs to be transported and used in naval application should comply with UN 38.3(Naval Ordnance Safety and Security Activity, 2010).

In this study, an impact load with momentum equivalent to 150 g acceleration was applied with a drop hammer as shown in the setup in Fig. 5.1 (b) earlier. The impact was applied in a 12 mm-diameter region at the center of the LIB and LIB pack with a flat punch. The battery clamp was removed to allow the LIB to absorb the entire force. For the 2-cell battery pack, the impact was applied to the top cell and transmitted to the bottom cell. The impact was applied on the LIBs every 100 cycles, and continuous cycling under vibration was carried out after each impact. During the vibration loading, the current of the two LIBs in the pack was measured by shunt resistors with the resistance of 1 mΩ. After each impact, the tested LIBs were allowed to rest in open-circuit condition for one day to simulate the periodic safety inspection applied after major dynamic events. The LIB's internal resistance was analyzed before and after each impact with the pulse current

method (Waag, Käbitz, & Sauer, 2013) to detect changes and damage that occurred. The relationship to impact velocity and drop height of the hammer is given by:

$$P_i = m_b \cdot v_{b,max} = m_h \cdot v_h \quad (5.1)$$

where P_i (g·m/s) is the equivalent impact momentum, m_b (g) is the mass of LIB test asset, $v_{b,max}$ (m/s) is the maximum impact velocity specified in UN 38.3 (Europe, 2015) and NAVSEA 9310 (Command, 2010) standards, m_h (g) is the weight of the hammer, and v_h (m/s) is the hammer impacting velocity. The dropping height of the hammer can be determined after obtaining v_h. To better understand the effects of dynamic loadings, controls were established where a LIB was cycled with vibration only, and another LIB was cycled under ambient conditions where no dynamic load was involved. A summary of these experiments with the number of cells, environments and cycles are provided in Table 5.4.

Table 5.4. Summary of proposed dynamic aging testing conditions.

Cell No.	Connection type	Vibration	Impact	Cycling current	Charging/ discharging method	Total cycles
1, 2	Parallel connection	Sinusoidal wave, 18 Hz, 1g acceleration	150 g equivalent acceleration, after every 100 cycles	170 mA	Constant current	500
3	-	Sinusoidal wave, 18 Hz, 1g acceleration	150 g equivalent acceleration, after every 100 cycles	170 mA	Constant current	500
4	-	Sinusoidal wave, 18 Hz, 1g acceleration	-	170 mA	Constant current	500
5	-	-	-	170 mA	Constant current	500

In order to verify the capability of the dynamic aging testing platform and sensor network, another type of Li-ion pouch cell from a different manufacturer was selected to repeat the dynamic aging test and sensor based LIB aging analysis mentioned above. Details on the LIB, sensor measurement results and on comparison of the two types of LIBs are provided in chapter 5.7.

5.3 Design of Dynamic Aging Test

The capacity of the tested LIBs are found using the conventional ampere-hour (Ah) counting method (Piller, Perrin, & Jossen, 2001) where the state of charge (SOC) is related to the amount of current charged or discharged. In Fig. 5.2, LIB performance during cycling in various dynamic environments is presented. A slight capacity rise is exhibited by all LIBs over the first 100 cycles. This can be attributed to the electrode surface area increase associated with the lithiation–delithiation process during formation cycles, which leads to enhanced access of electrolyte to the electrode material (Manev, Naidenov, Puresheva, & Pistoia, 1995).

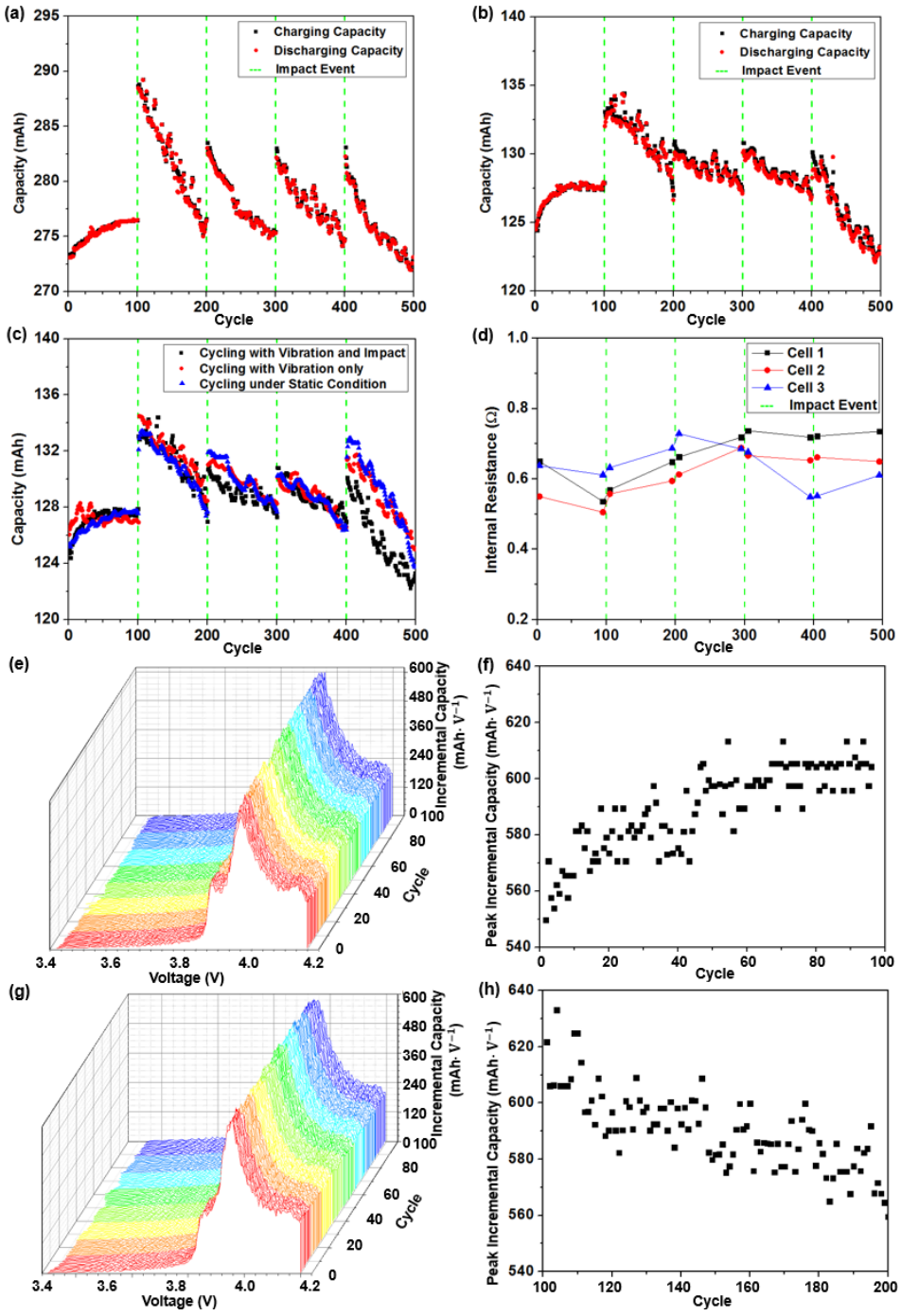

Figure 5.2. (a): Capacity of 2-cell pack (cell 1 and 2) under in-service vibration and impact; (b): Capacity of single cell (cell 3) under in-service vibration and impact; (c): Capacity comparison of single cell under different dynamic conditions; (d): Internal resistance of LIBs under in-service vibration and impact; (e): Incremental capacity of cell 3 in cycle 1-100; (f) Peak incremental capacity of cell 3 in cycle 1-100; (g) Incremental capacity of cell 3 in cycle 101-200; (h) Peak incremental capacity of cell 3 in cycle 101-200.

In order to understand the change in cell reaction kinetics and to explain the capacity rise, incremental capacity dQ/dV of cell 3 was calculated. The results for cycles 1-100 and 101-200 are shown in Fig. 5.2 (e-h). The peak value of incremental capacity increases over the first 100 cycles, then decreases over cycles 101-200. The work of Dubarry et al. (Dubarry, Truchot, & Liaw, 2014) has indicated that a decrease in the peak capacity value represented a loss of lithium inventory and active material. Since Coulombic efficiency remains relatively high (>99.5%) throughout the cycling, contribution of lithium inventory loss during the initial cycles is negligible. Thus, enhanced access to the active material from electrochemical milling is dominant and results in the observed capacity increase over the first 100 cycles (Dubarry et al., 2014). Though the applied impacts on the electrodes were intended to degrade the LIBs, observations show that the LIBs exhibit capacity retention immediately following the impacts, which could be attributed to the one-day rest period after applying the impact. As the LIBs are cycled, byproducts such as LiF and Li_2O form and build-up around the electrode that limits electrochemical reaction transport resulting in accelerated capacity fade (Zheng et al., 2014). By allowing the battery to rest after impact, the byproducts dissolve and dissipate into the electrolyte, which restores the available capacity for future cycles (Saha & Goebel, 2009). However, this capacity recovery is not sustainable over continuous cycling, as byproduct formation will continue.

Dynamic impact can also result in electrode particle fracture and delamination (Brand et al., 2015), which influences the residual stress, bonding strength and stress concentration condition of electrode materials (B. Li et al., 2018; Vikas Tomar, 2008). Impacts with limited momentum can release the intrinsic compressive stress within the electrodes [12], while high momentum impacts can cause severe cracking of electrode materials (Kermani & Sahraei, 2017; Kisters, Sahraei, & Wierzbicki, 2017). Since electrode materials are basically composites, interfaces of different constituents and variations in constituent properties, constituent concentration, and phase morphology can form a nonuniform stress field within electrode particles that makes the fracture inherently stochastic (V. Tomar, 2008a; Tomar & Zhou, 2005; K. Zhao, Pharr, Vlassak, & Suo, 2010) and can cause further capacity loss. As a result, cells 1, 2 and 3 exhibited rapid capacity loss in the continuous cycling after impacts, which is also reflected by the decreases in the peak value of incremental capacity. Thus, the capacity recovery following equipment inspection or maintenance should not be considered for long-term battery service planning. Starting from the first impact test at the 100th cycle, the capacity fading rate remained nearly constant for each group

of 100 cycles between two impacts, as can be seen in Fig. 5.2 (a, b). However, the average capacity fading rate of different groups of 100 cycles are different, which represents various rates of aging. The average cell capacity fading rates for each group of 100 cycles between two impact events are presented in Table 5.5:

Table 5.5. Average cell capacity fading rate over continuous cycling.

Cycle No.	Average Cell Capacity Fading Rate of 2-Cell Pack (cell 1 and 2, mAh per cycle)	Average Capacity Fading Rate of Cell 3 (mAh per cycle)
101-200	0.0609	0.0580
201-300	0.0369	0.0306
301-400	0.0380	0.0343
401-500	0.0545	0.0412

Based on Fig. 5.2 (a, b) and Table 5.5, for LIBs experiencing in-service vibration and impact, the loss of capacity from continuous cycling can be predicted with a first-order function. In this study, the continuous vibration and periodical impacts applied at the end of charge are unlikely to trigger catastrophic capacity fade or thermal runaway. However, from the capacity comparison in Fig. 5.2 (c), cell 3 presents higher capacity decay approaching EOL compared to cell 4 and 5. This indicates that dynamic loading such as vibration and impact may not affect the LIB immediately, but repeated and continuous environmental stress can affect the battery over its operating life. It is then necessary to monitor dynamic shocks and vibration level over the whole LIB service life.

Although electrochemical analysis provides a reliable estimation of LIB state of health (SOH), there are significant drawbacks: a complete cycle needs to be conducted prior to electrochemical analysis, complex and time-consuming calculations need to be performed, and the battery cycling must be periodically interrupted for measurements such as internal resistance. These limitations affect the performance, efficiency, and applicability of electrochemical analysis for in-operando battery safety and performance monitoring and management.

5.4 Sensor-based Analysis of Li-ion Battery Performance under in-operando Dynamic Loading

The temperature of cells 1-3 are continuously monitored by RTDs during continuous constant current cycling, environmental vibration and impact as shown in Fig. 5.3. The cycling profiles are provided in Table. 5.4. The temperature decreases initially during charge and then begins to increase at the 40% SOC point until fully charged. During discharge, the temperature decreases before approximately 10% of the charge is removed and then rapidly increases, especially after 80% of the charge has been removed. The endothermic reactions at the beginning of charging and discharging are due to the effective entropic potential of these periods (G. Liu et al., 2014). From Fig. 5.3, it can be found that the battery temperature peaks are located precisely at the end of the charge and discharge cycles. The rate of temperature change (ºC/minute) of cell 3 is provided in Fig. 5.3 (b). Two peaks with high temperature increasing rate can be noticed at the end of charge and discharge, indicating that in continuous cycling, abrupt temperature rise is expected when the LIB is to be fully charged or discharged. As a result, the LIB is most susceptible to thermal runaway at the end of a full discharge. Temperature monitoring of these periods is most informational for thermal runway prevention of LIBs during operation. Thus, the most critical point to measure LIB temperature is at the end of charge and discharge, and it is not necessary to monitor the battery temperature continuously. However, disconnected fully discharged cells rarely experience thermal runaway, which is why UN, DOT and DOD require shipping batteries with a SOC of 30% or less. As a result, different safety management strategies should be applied for disconnected and in-service LIBs, which further confirms the value of in-operando LIB abusing tests.

From the deformation measurement using the eddy current sensor, the thickness of cell 3 increases with charge as expected, reaching a maximum thickness at the end of charge, then decreases during discharge. This phenomenon occurs from the lithiation and delithiation process as Li ions are shuttled between the anode and cathode. If the cell is constrained by battery holders, or in the case of an 18650 cell or a sealed prismatic cell, stress would accumulate from material expansion during charge. Therefore, the most critical point to measure deformation is at the end of a charge cycle where the electrodes are the most reactive and under the highest stress. To mitigate this condition, the charge cutoff voltage can be reduced. This is a technique that has been used in applications where safety is an issue, such as manned vehicles.

A strategy to prevent thermal runaway and catastrophic failure does not require continuous monitoring and data storage throughout the entire charge/discharge cycle. Temperature monitoring should begin near the end of discharge, and deformation monitoring should begin near the end of charge. Individual cells in high voltage battery pack of series connection need to be monitored to avoid cell overcharge and overdischarge.

When cycling two cells in parallel, the ratio of the cycling current of I_1/I_2 is used as an indicator of how well the cells are balanced. As illustrated in Fig. 5.3 (a), the largest imbalance occurs at the beginning of charge and the end of discharge. Particular attention should be made at the end of discharge where the current varies the greatest. This cell imbalance could become problematic over repeated charge and discharge cycles, especially in batteries with multiple cells in parallel and series configurations where both suspect cells and other good cells get worse by overcharging and overdischarging (Love et al., 2014). This explains the difference in capacity fading rates observed in Table 5.5 for the single cell and the two parallel cells battery pack. With all three batteries subjected to the same environmental conditions, the cell imbalance accelerates the aging of the two-cell pack. Thus, for a LIB pack with many cells, sensors to monitor cell balance are essential for detecting suspect cells and improving capacity retention.

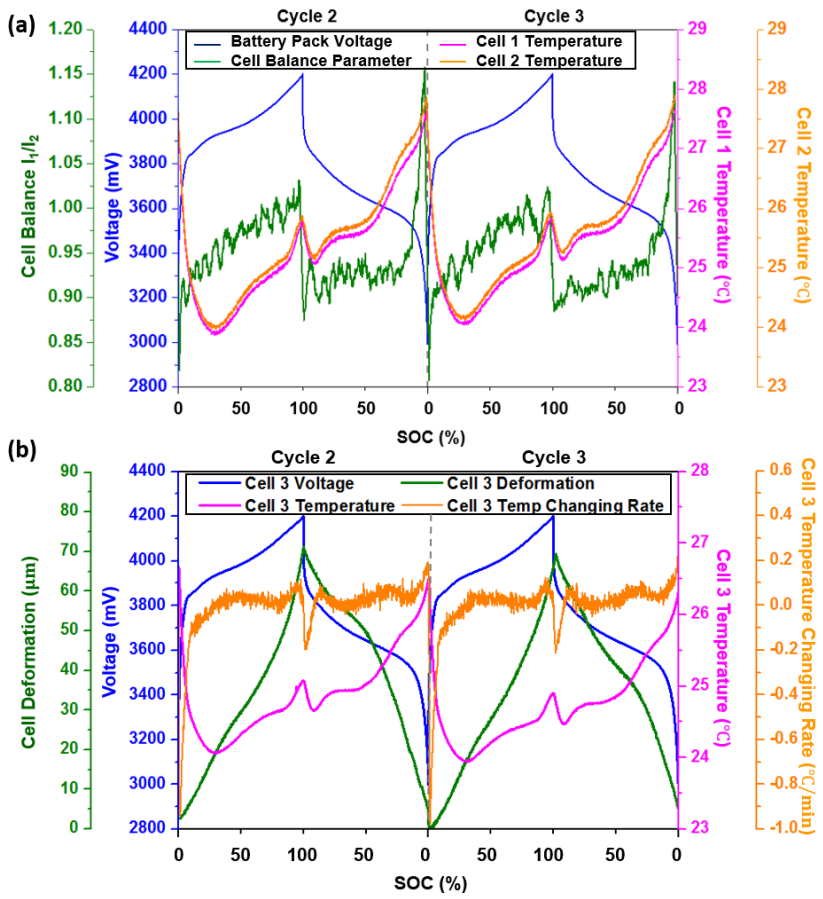

Figure 5.3. Voltage, temperature, temperature changing rate, deformation and cell balance parameter I_1/I_2 in two consecutive cycles of (a): 2-cell pack (cell 1 and 2), (b): single cell (cell 3).

To prevent the onset of a cell going into thermal runaway, the temperature of individual cells must be monitored, especially at the end of charge and discharge. However, real-time temperature measurement of every cell is not always feasible due to the cost, volume, and weight by adding sensors, wiring, data acquisition, processing, storage and user interface. Adding a complete cell monitoring system could parasitically drain cells if installed incorrectly. Thus, a simple indirect method that can reliably estimate the cell's maximum temperature, such as battery capacity measurement, is preferred.

Both experimental analysis and theoretical modeling suggest that heat generation rate varies significantly within each cycle during LIB cycling (Taheri & Bahrami, 2012; M.-S. Wu, Liu, Wang, & Wan, 2002). It is also observed in Fig. 5.3 that the relation between the cell's temperature and SOC was nonlinear. There are two regions where rapid temperature rises correlate

well with SOC, when 100% SOC is approached during charge and 0% SOC is approached during discharge. While peak temperature can be predicted by SOC using a linear relation, significant deviation can occur in the predicted relation over extended battery usage (X. Wu, Lv, & Chen, 2017). Moreover, the irreversible reactions in LIB operation and subtle defects in a cell can also influence these high rate heat generation periods. Loss of active lithium ions can make $LiCoO_2$ cathode less intercalated at the end of charge and graphite anode less delithiated at the end of discharge, which results in change of electrode SOC over battery cycling (Q. Zhang & White, 2008). As a result, these periods of rapid heat generation diminish gradually over a LIB's cycle life. Therefore, another characteristic that accurately estimates peak temperature over the operational life is needed, such as an energy balance-based relation.

If phase-change related heat generation can be neglected, a general energy balance of a lithium-ion cell can be described as (Bernardi, Pawlikowski, & Newman, 1985):

$$q - MC\frac{dT}{dt} = I(V - U_{ocv}) + IT\frac{\partial U_{OCV}}{\partial T} \tag{5.2}$$

where q (W) is the rate of heat transfer, M (g) is the battery mass, C ($J \cdot g^{-1} \cdot K^{-1}$) is the mean heat capacity, T (K) is the battery temperature, I (A) is the current, V is the terminal voltage (V) and U_{OCV} is the open circuit voltage (V). In this relation, if the temperature within the cell can be assumed uniform (S. Wang et al., 2017), and the top and bottom surfaces of the battery holder are assumed to be at room temperature, then q can be expressed as:

$$\mathbf{q} = -h_{conv}A_{conv}(T - T_{air}) - \frac{(T - T_{air})}{\frac{1}{h_{cond}A_{cond}} + \frac{d}{k_{pla}A_{cond}}} = \not{f} * (T - T_{air}) = \not{f} * \Delta T \tag{5.3}$$

where A_{cond} (mm^2) is the area of thermal conduction, A_{conv} (mm^2) is the area of thermal convection, d (mm) is the thickness of battery holder, h_{cond} ($W \cdot mm^{-2} \cdot K^{-1}$) is the contact conductance of the pouch cell-battery holder contacting surface, h_{conv} ($W \cdot mm^{-2} \cdot K^{-1}$) is the thermal convective coefficient of air, k_{pla} ($W \cdot mm^{-1} \cdot K^{-1}$) is the thermal conductivity of PLA, and T_{air} (K) is the air temperature. The relation between q and $(T - T_{air})$ can be expressed with a first-order relation with a heat dissipation coefficient $\not{f}$. The coefficients in (3) are considered to be independent of temperature within the range of analysis, and $\not{f}$ becomes a negative constant. Combining equations (5.2) and (5.3) gives:

$$\not{f} * \Delta T - MC\frac{dT}{dt} = \not{g}(T, \dot{T}) = I(V - U_{ocv}) + IT\frac{\partial U_{OCV}}{\partial T} \quad (5.4)$$

Here $I(V - U_{ocv})$ represents Joule heating, which mostly originates from internal resistance as indicated by voltage drops (Jeon & Baek, 2011). The analysis of Han et al. on internal resistance of aged LIBs shows negligible changes over 600 cycles (X. Han et al., 2014), which agrees with our observation in Fig. 5.2 (d). Thus, the change in Joule heating over cycling can be neglected. The reaction heat $IT\frac{\partial U_{OCV}}{\partial T}$ is determined by the effective entropic potential $T\frac{\partial U_{OCV}}{\partial T}$ for constant current cycling. Liu et al. (G. Liu et al., 2014) analyzed 300 cycles of LIBs and their results indicate that $T\frac{\partial U_{OCV}}{\partial T}$ is not dependent on temperature and varies little over cycle life, except when the cell's SOC falls in the range of 62.5% to 87.5% where the electrochemical reactions are endothermic. Since the cell's behavior during discharge is overall exothermic, the difference in effective entropic potential within the endothermic range contributes little to the overall heat generation, and can be neglected. Wu et al. (X. Wu et al., 2017) also confirmed that $\frac{\partial U_{OCV}}{\partial T}$ is of limited magnitude and variation within the endothermic range. Thus, an invariable relation between effective entropic potential, SOC and temperature makes it possible to predict temperature as the cells age.

Second-order fitting of effective entropic potential and temperature reported by Liu et al. (G. Liu et al., 2014) gives:

$$T\frac{\partial U_{OCV}}{\partial T} = a * SOC^2 + b * SOC + c = -0.254 * SOC^2 + 0.3388 * SOC - 0.092\ (V) \quad (5.5)$$

Solving equation (5.4) for the discharging cycle with the above assumptions, when the battery is fully discharged (t=cap/I), the equation is given by:

$$\Delta T = C_0 \cdot \exp\left(\frac{\not{f}}{MCI} \cdot cap\right) + \frac{1}{\not{f}}\left[2a \cdot \left(\frac{MCI}{cap \cdot \not{f}}\right)^2 - b \cdot \frac{MCI}{cap \cdot \not{f}} + (c - I^2 r)\right] \quad (5.6)$$

where cap $(A \cdot s)$ is the battery capacity and C_0 is the constant of integration. In a study by Murashko et al. and Bryden et al., pouch format cells with low capacity exhibited specific heat capacities of 1.012- 1.067 $J \cdot g^{-1} \cdot °C^{-1}$ (Bryden et al., 2018; Murashko, Mityakov, Pyrhönen, Mityakov, & Sapozhnikov, 2014). Work by Murashko et al. showed that SOC has a negligible effect on LIB's heat capacity (Murashko et al., 2014) and can be represented by a constant value in thermal modeling. Therefore, a specific heat capacity of 1 $J \cdot g^{-1} \cdot °C^{-1}$ for LIBs was adopted.

In Fig. 5.4 (a-c), the relation between ΔT and capacity is fitted with a mixed exponential-polynomial function given by equation (5.5), from which C_0 and $\not{f}$ are obtained. This model accounts for heat generation from Joule heating and reactions as well as heat losses, and it describes how the LIB's temperature changes over long-term cycling.

For example, a comparison of the temperature profiles of cell 1 and 2 in Fig. 5.3 (a) show that cell 2 operates at a higher temperature than cell 1, especially at the end of discharge. Heat dissipation conditions of these two cells are similar since they are clamped together as a battery pack, which is also verified by their comparable values of heat dissipation coefficient $\not{f}$. Therefore, cell 2 is generating more heat. Since Joule heating is based on cell impedance that remains constant in the contribution to total LIB heat generation in high-rate cycling operation (B. Wu et al., 2013), the difference in temperature rise should be attributed to the reaction heat generation. The different reaction heat of cell 1 and 2 can be correlated with the cells' overpotential and difference in open circuit voltage (OCV). As cell 1 has higher discharging current when SOC approaches 0, it possesses higher overpotential towards the end of the discharging cycles. Since both LIBs had the same terminal voltage from parallel connection, cell 1 possesses higher OCV and SOC when the discharging cycle ends. Considering the region of SOC approaching 0% is when high-rate reaction heat generation occurs, the heat generated in cell 1 is lower than cell 2 resulting in a larger temperature difference as shown in Fig. 5.3 (a). The temperature difference exists throughout the cycle but is not as pronounced because the reaction heat generation is lower. This observation further confirms the importance of individual cell temperature monitoring in a battery pack, and now can be achieved indirectly using the capacity measurements in the relation discussed above for accurately estimating temperature rise without using temperature sensors.

With the temperature rise-capacity relation established, an indirect analysis of LIB temperature can be achieved with capacity measurement. Large LIBs will benefit from this indirect approach in temperature prediction where adding dedicated temperature monitoring is not possible or cost effective. In a battery that uses many cells in a tightly packed configuration, the temperature of a cell is not solely dependent on its capacity, but also on adjacent cells. This has been reported in several experimental and numerical analyses works on LIBs where adjacent cells share similar temperature profiles (Kizilel, Sabbah, Selman, & Al-Hallaj, 2009; Liao, Ma, Peng, Garg, & Bao, 2019; W. Liu, Jia, Luo, Xie, & Deng, 2019; Saw, Tay, & Zhang, 2015). Thus, for

indirect analysis of peak temperature of cells in a tightly packed battery, which is common, capacity values and temperature rise of the adjacent cells must be considered.

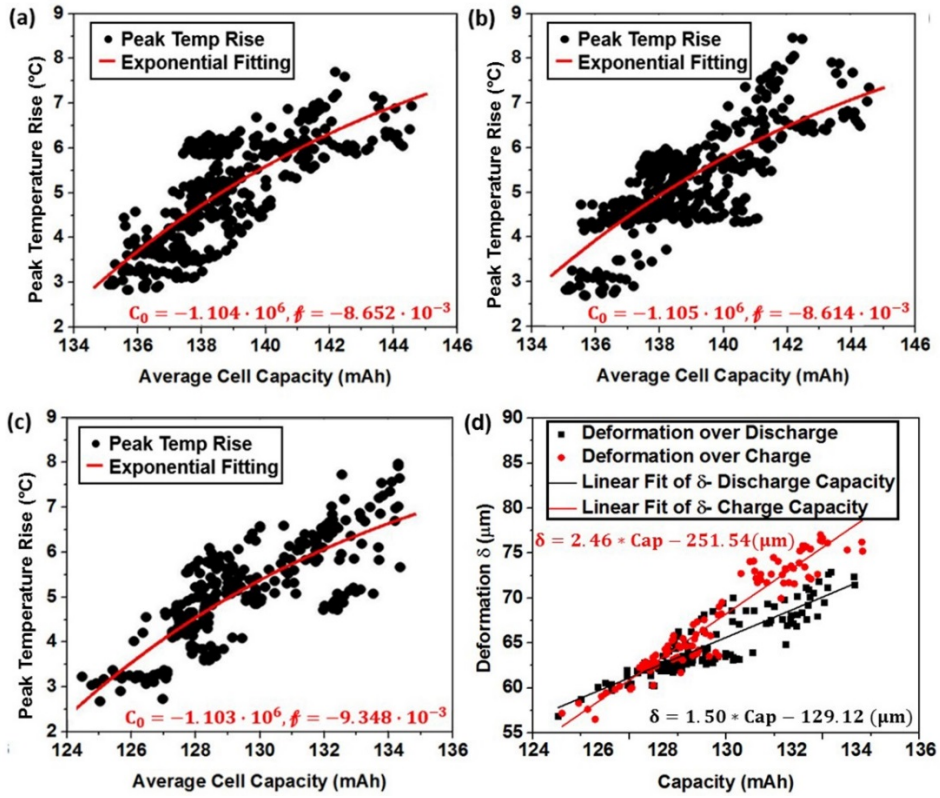

Figure 5.4. Relation between maximum temperature increase and capacity of (a): cell 1, (b): cell 2 and (c): cell 3. (d): Relation between maximum deformation and capacity of cell 3.

Stress accumulation in LIBs during cycling magnifies the dendrite growth related safety risk, which can lead to internal short circuit and thermal runaway. The stress level in LIBs can be monitored with deformation measurements using an eddy current sensor. As the cell's volume changes in proportion to electrode thickness changes during lithiation (charge) and delithiation (discharge), thickness change of LIBs can be described by equation (5.7) (Fu, Xiao, & Choe, 2013):

$$\Delta h_{max} = 3h_0 \frac{\Delta R_{s,max}}{R_{s0}} = h_0 \cdot \bar{c}_{s,max} \cdot \Omega \tag{5.7}$$

where $\bar{c}_s$ (mol$\cdot$ mm^{-3}) is the average ion concentration in the solid phase of the electrode, h (mm) is the electrode thickness, R_s (mm) is the radius of spherical electrode particle, and Ω (mm$^3 \cdot$ mol^{-1}) is the theoretical partial molar volume of lithium ion. If Ω is assumed to be constant (Fu et

al., 2013), a linear relation can be expressed between cell deformation and capacity. The relation between cell deformation and capacity observed in the cycling of cell 3 in the dynamic environment is shown below in Fig. 5.4 (d).

Fig. 5.4 (d) shows that more deformation occurs during charge than in discharge, causing the cell to gradually swell over cycle life. This net deformation growth can be attributed to (1) gas generation, (2) SEI growth, (3) micro-level fracture and cavitation developed during high rate charging-discharging cycles, (4) Poisson's effect induced deformation associated with the in-plane compression between the graphite electrode particles, and (5) release of intrinsic compressive stress within the electrode material from the calendering process. Reasons (2-5) are related to the electrode thickness change. The average thickness of a single layer graphite electrode after 500 cycles is 155.61 μm, which is 420 nm thicker than the pristine electrode with the average thickness of 155.19 μm. There is no obvious change in the thickness of LCO electrode. The total thickness change of electrodes in the LIB is lower than the deformation change observed in Fig. 5.4 (d). Thus, gas formation is the key factor leading to the deformation. The other factors are also discussed below.

Under the proper operation of a good LIB, gas generation is caused by electrolyte decomposition over the operating life (S. S. Zhang, 2014), which agrees with our observation that the swelling of LIB is not limited to the initial few cycles of SEI formation. Electrolyte at the SEI breaks down and releases gas from chemical and redox decomposition. Alkali metal carbonates, such as Li_2CO_3, can serve as a catalyst or directly participate in gas generation. Some typical reactions for gas generation in $LiCoO_2$-graphite cell are listed in equations (5.8-12) (Q. Yang, Wang, Ding, Yang, & Wang, 2015; S. S. Zhang, 2014):

$$R_1O-\overset{\overset{O}{||}}{C}-OR_2 \xrightarrow{\text{catalyst}} R_1O-C-OR_2 + CO_2 \tag{5.8}$$

$$CO_2 + 2LiC_6 \rightarrow Li_2O + C_6 + CO \tag{5.9}$$

$$CO_2 + 2Li^+ + 2e^- \rightarrow Li_2O + CO \tag{5.10}$$

$$R_1O-\overset{\overset{O}{||}}{C}-OR_2 + Li_2CO_3 \xrightarrow{\text{catalyst}} R_1OLi + R_2OLi + 2CO_2 \tag{5.11}$$

$$Li_2CO_3 + LiPF_6 \rightarrow 2LiF + LiPOF_4 + CO_2 \tag{5.12}$$

In reference to equation (5.7), if no gas generation is involved, a linear relation is expected between the LIB deformation and lithium ion concentration in the electrode, and there should be no accumulated deformation over the charge/discharge cycles. Fig. 5.3 (b) shows that the rate of LIB deformation for SOC < 80% remains nearly constant. At SOC > 80%, the rate of shrinking is lowest under discharging, and the rate of swelling is highest under charging. Hence, the gas generation rate is highest at SOC > 80%. Electrode potential-SOC relation shows that the potential of graphite anode is relatively flat at around 0.25 V vs. Li/Li^+, while that of $LiCoO_2$ cathode changes linearly with SOC (S. S. Zhang, Xu, & Jow, 2006). This suggests that the oxidization of electrolyte on the cathode results in the increased gassing above 80% SOC (S. S. Zhang, 2014). Thus, gas generation is one of the reasons for the deformation behavior observed in eddy current sensor measurements. LIBs are most prone to failure due to gas accumulation when fully charged, which is the same point where the highest temperature occurs during charge. Thus it is important to evaluate the LIB state of health comprehensively in terms of stress accumulation and temperature increase with the RTD and eddy current sensor when the LIB is of high SOC.

The SEI thickness of a few nanometers develops during the first few cycles, or commonly known as formation cycles (Smith, Burns, & Dahn, 2010). However, the measured LIB deformation is much higher than the typical SEI thickness, revealing that SEI formation is not the key factor in electrode thickness change. SEM images of pristine electrodes and electrodes after 500 cycles are shown in Fig. 5.5. The electrodes are pre-cleaned with dimethyl carbonate to remove the electrolyte salt residuals (S.-H. Lee et al., 2014). The SEI film on the aged graphite electrode from cell 3 is slightly more condense than that on the aged graphite electrode from cell 5, since vibration promotes the formation of SEI as shown by the X-ray photoelectron spectroscopy analysis by Somerville et al. (Somerville et al., 2017). The SEI thickness in both cell 3 and cell 5 are very limited, which is negligible for the LIB swelling. No obvious electrode particle cracking, peel-off or change in the electrode surface profile could be observed as shown in Fig. 5.5. However, this does not exclude the possibility of micro-level fracture within the electrode material or cavitation with the particles, as SEM imaging was limited to the electrode surface.

Although it is not observed in SEM images, there is the possibility for micro-level fracture on particle- binder interface and cavitation in the particles. Numerical simulation shows stress concentration at the center and edge of electrode particles from LIB charging and the first principle stress is at the level of 10^7-10^8 Pa (Iqbal & Lee, 2018). Lithium diffusion gradient due to high rate

cycling also generates deformation gradient and stress concentration in LIB electrodes (Iqbal & Lee, 2018; Zuo & Zhao, 2016). When the stress exceeds the strength of particle- binder interface or graphite, the formation of crack and cavity should be expected (Rahani & Shenoy, 2013), which can result in swelling of the cell.

Since the electrode thickness is relatively large compared to the average diameter of the electrode particles, deformation gradient in the thickness direction of the electrode should be considered. In-situ tensile tests and SEM imaging of LIB electrodes show that particles at the bottom are passively fixed to the current collector, while the particles at the top are less constrained by the current collector (Zhu, Zhang, Luo, & Sahraei, 2018). Graphite particles experience volume expansion due to lithium insertion during the charging of LIBs and a 13.2% volume change is expected when graphite is fully lithiated to LiC_6 (Schweidler et al., 2018). For the particles fixed on the current collector and in direct contact with those adjacent, this 13.2% volume expansion is sufficient to generate plastic deformation in the particle compression considering the compressive behavior of graphite (Jones, 1977; Yokoyama, Nakai, & Futakawa, 2008). Similar behavior has been seen in other polymer-particle based material systems, (T Qu, D Verma, M Alucozai, & V Tomar, 2015; Verma & Tomar, 2015). This in-plane compressive stress can increase the electrode's thickness and contribute to the deformation observed.

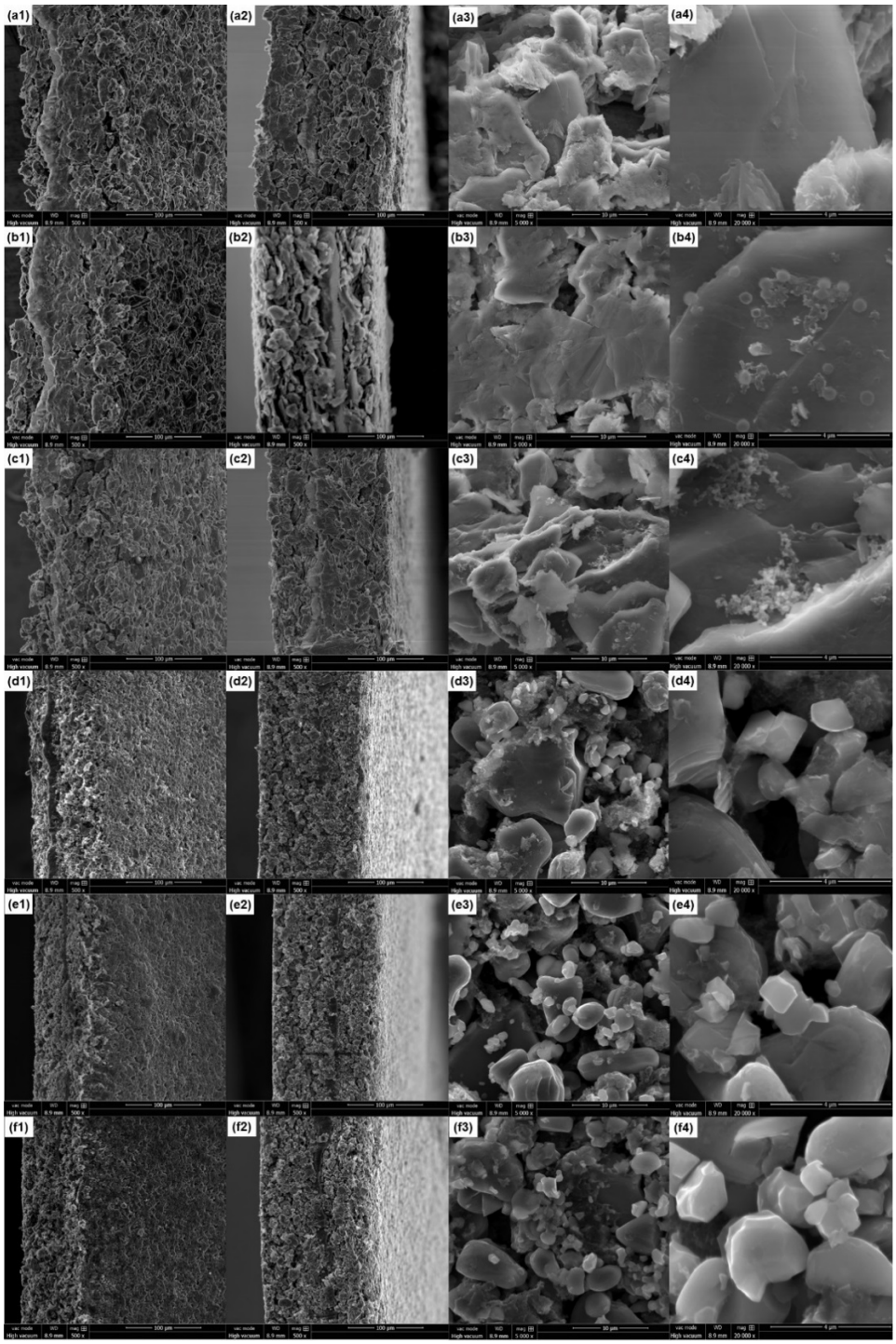

Figure 5.5. SEM images of graphite electrode (a1-a4, b1-b4 and c1-c4) and LCO electrode (d1-d4, e1-e4 and f1-f4). (a1-a4 and d1-d4): electrodes from fresh LIB; (b1-b4 and e1-e4): electrodes from LIB after 500 cycles with no vibration (cell 5); (c1-c4 and f1-f4): electrodes from LIB after 500 cycles with vibration and impact (cell 3). Imaging orientation: (a1-f1): 45º, (a2-f2): 90º, (a3-f3 and a4-f4): 0º.

Another type of electrode deformation that has been long neglected is the deformation from residual compressive stress release in electrodes. The calendering process generates compressive stress within the electrodes and has been verified by both numerical simulation (H. Kim, 2009) and experimental measurement (D. Liu et al., 2013). To analyze the change in residual stress during the cycling and vibration of LIBs, Raman spectroscopy analysis is applied to pristine and aged electrode, which are collected from a fresh LIB and an aged LIB (cell 3) at the open circuit voltage of 3.0 V. Representative Raman spectra are shown in Fig. 5.6 (a3, b3, c3 and d3).

G band in the Raman spectrum of graphite electrode (~1582 cm^{-1}) comes from the E_{1g} vibration mode of graphite (Reich & Thomsen, 2004) and is the most widely used characteristic Raman peak for graphite. The shape and position of G band change when the mechanical stress level or lithium intercalation state of graphite changes (del Corro, de la Roza, Taravillo, & Baonza, 2012; Frank et al., 2011; Inaba et al., 1995; Sole, Drewett, & Hardwick, 2014). After fitting with Lorentz function (Sakata, Dresselhaus, Dresselhaus, & Endo, 1988), the average G band position for the pristine graphite electrode is determined as 1586.03 cm^{-1}, which is higher than 1582 cm^{-1}. This observation is similar to that of Liu et al., where the graphite electrode presented a positive Raman shift after calendering (D. Liu et al., 2013). This result verifies the existence of residual compressive stress in the graphite electrode after calendaring as G band of graphite presents a positive shift upon the application of compressive stress (del Corro et al., 2012). The magnitude of this positive shift in G band position decreases after the 500 cycles under vibration: the average G band Raman shift of the aged graphite electrode is 1585.22 cm^{-1}. As there is no double peak feature in the G band of aged graphite electrodes, there is no residual intercalated lithium content (Inaba et al., 1995; Sole et al., 2014). Thus the difference in the G band position comes from change in the stress level of graphite electrode and it reflects release of the residual compressive stress (del Corro et al., 2012). This corresponds with the result of our previous research: dynamic loads with small magnitude impair the bonding between electrode particles and release the residual compressive stress (B. Li et al., 2018). Some of the compressive deformation from the calendering process is released after the decrease of residual compressive stress, and this can cause an increase in the graphite electrode thickness.

Another characteristic feature in the Raman spectrum of graphite is the intensity ratio of D band and G band (I_D/I_G). The I_D/I_G value is inversely proportional to the lattice size of graphite (Pimenta et al., 2007):

$$L_a = \frac{560}{E^4} \cdot \left(\frac{I_D}{I_G}\right)^{-1} \quad (5.13)$$

where L_a is the lattice size in nm and E is the excitation laser energy in eV. The average I_D/I_G ratio of pristine graphite electrode is 0.46 and that of aged graphite electrode is 0.49. The lithiation-delithiation process in continuous cycling of LIBs can induce disorder and dislocation within the graphite material (Sethuraman, Hardwick, Srinivasan, & Kostecki, 2010) and cracking of graphite particles (Pimenta et al., 2007), which can be reflected by the value of L_a. For the graphite electrode from cell 3 analyzed here, its lattice size decreases slightly compared to the fresh LIB. Thus, there is some dislocation and crack formation in the graphite electrode over the 500 cycle period, but it is not significant to be considered as the main reason of LIB volume change and performance degradation.

For the LCO electrode, the position of A_{1g} peak reflects the mechanical stress and composition of the electrode material. When lithium is extracted from LCO, position of the A_{1g} peak moves to the negative direction rapidly and the shift is -12 cm^{-1} when the LIB reaches 100% SOC (Snyder, Apblett, Grillet, Beechem, & Duquette, 2016). Similar to graphite, the A_{1g} peak of LCO presents a positive shift when tensile stress is applied and the A_{1g} peak is fitted with Lorentz function (Inaba, Iriyama, Ogumi, Todzuka, & Tasaka, 1997). The average A_{1g} peak position is 595.86 cm^{-1} for the pristine LCO electrode and 595.81 cm^{-1} for the aged LCO electrode. This negative Raman shift has a limited magnitude and mostly originates from the loss of lithium content due to SEI formation. Release of the residual compressive stress is also a reason for this negative shift (B. Li et al., 2018; X. Wang et al., 2005). Since the magnitude of the A_{1g} peak position change is limited, the structure change in the LCO electrode of cell 3 is negligible. Thickness measurement of pristine and aged LCO electrodes also verify this.

To conclude, most swelling observed in the tested LIB appears to be caused by gas generation in this work, while thickness change of the graphite electrode from the release of residual compressive stress is another reason. There are some other factors that can also cause the LIB thickness to increase, which are discussed above. However, their contribution are limited.

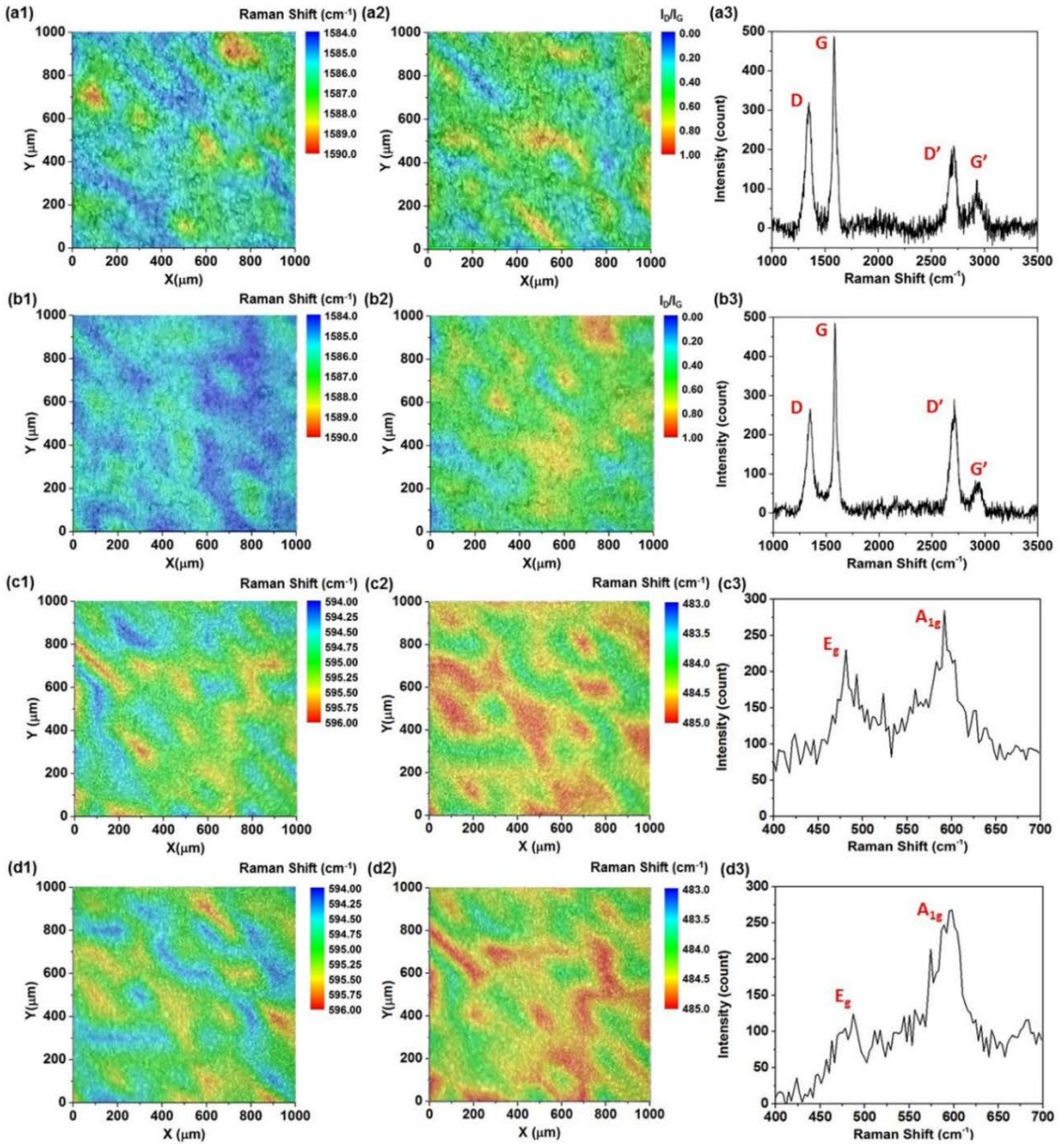

Figure 5.6. (a1) G band Raman shift contour of pristine graphite electrode, (a2): D, G band intensity ratio (I_D/I_G) contour of pristine graphite electrode, (a3): representative Raman spectrum of pristine graphite electrode; (b1): G band Raman shift contour of aged graphite electrode, (b2): D, G band intensity ratio (I_D/I_G) contour of aged graphite electrode, (b3): representative Raman spectrum of aged graphite electrode, (c1) A_{1g} band Raman shift contour of pristine LCO electrode, (c2) E_g band Raman shift contour of pristine LCO electrode, (c3): representative Raman spectrum of pristine LCO electrode; (d1): A_{1g} band Raman shift contour of aged LCO electrode, (d2) E_g band Raman shift contour of pristine LCO electrode, (d3): representative Raman spectrum of aged LCO electrode.

5.5 Comparison of Sensor Measurement Reliability for Indirect Battery Performance Evaluation

With the temperature-capacity and deformation-capacity relation established for LIBs, RTD and eddy current sensor can both be used to indirectly measure capacity. Based on Fig. 5.4, the sensors can help to identify LIB capacity fade without the need of continuous measurement as in coulomb counting. The conventional coulomb counting for SOC and capacity measurement also suffers from cumulative errors due to the initial SOC and measurement uncertainties due to integration over time errors (Baccouche, Jemmali, Mlayah, Manai, & Amara, 2018).

As both RTD and eddy current sensor can indirectly measure the LIB capacity, their reliabilities are compared to identify the better sensor for detection of LIB capacity decay. Information entropy H(X) is employed for the comparison, which can be described as (Ho & Yeung, 2010):

$$\mathrm{H(X)} = -\sum_{\mathrm{i=1}}^{\mathrm{n}} \mathrm{p_i} \cdot \log(\mathrm{p_i}) \tag{5.14}$$

where $\mathrm{p_i}$ is the probability of the variable X taking the value of i, and n is the total number of discrete data points for variable X. Accordingly, conditional entropy is defined as:

$$\mathrm{H(D|A)} = -\sum_{\mathrm{i=1}}^{\mathrm{n}} \mathrm{p_i H(Y|A = a_i)} \tag{5.15}$$

where $\mathrm{H(D|A)}$ is the information entropy under the condition that a second variable, A, is taking a known value of $\mathrm{a_i}$. Information divergence is then provided as:

$$\mathrm{g(D, A)} = \mathrm{H(D)} - \mathrm{H(D|A)} \tag{5.16}$$

Information divergence has been widely used as a measurement of how the distribution of one variable can reduce the randomness of the system (Białynicki-Birula & Mycielski, 1975; Ho & Yeung, 2010; Mejia-Rodriguez, Renaud, & Tomar, 2008; G.-y. Wang, Yu, & Yang, 2002). Here cell deformation and peak temperature are compared in terms of information divergence to evaluate their capability to identify battery capacity fade. The variable providing higher information divergence can predict battery capacity more reliably. A 5% capacity fade is set as the detecting threshold, and the two variables are employed to locate cycles with more than 5% capacity fade. The value of 5% was selected considering the difference between the maximum and minimum capacity observed in cells 1-3 was around 7% in the experiment. Temperature and

deformation data are discretized into groups of 2, 3 and 5, and analysis with different numbers of groups can indicate the better variable under scenarios with different database sizes. Information divergence for capacity fade identified by RTD and eddy current sensors is calculated and compared in Fig. 5.7:

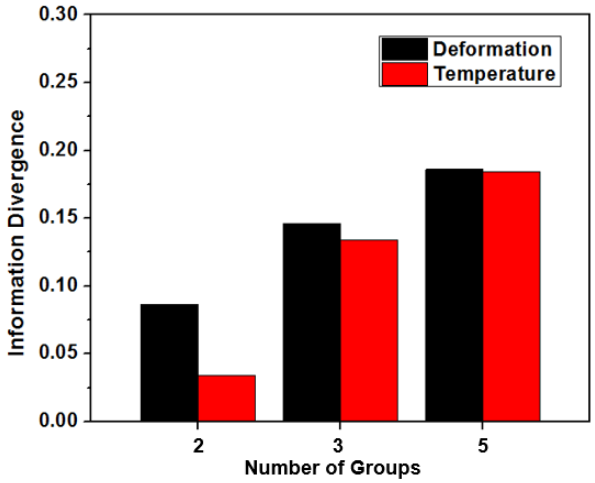

Figure 5.7. Comparison of information divergence obtained with battery deformation and peak temperature for capacity fade detection.

From the comparison on information divergence, deformation measurements detect capacity fade better than temperature, especially when the amount of data is limited to discretize data into many groups. When a large amount of data is available, the reliability of capacity fade detection by temperature and deformation measurements are equally comparable.

5.6 Electrochemical Impedance Spectroscopy Analysis of Li-ion Battery Performance Degradation

As a support for the measurement with the sensor network, electrochemical impedance spectroscopy (EIS) analysis is applied to cell 1-5 and the spectrums are compared to those acquired before the cycling test. The EIS result comparison is shown in Fig. 5.8 (a-e) and the equivalent circuit is provided in Fig. 5.8 (f), which is developed based on a commonly used equivalent circuit model (W. Choi, Shin, Kim, Choi, & Yoon, 2020; Song & Bazant, 2012).

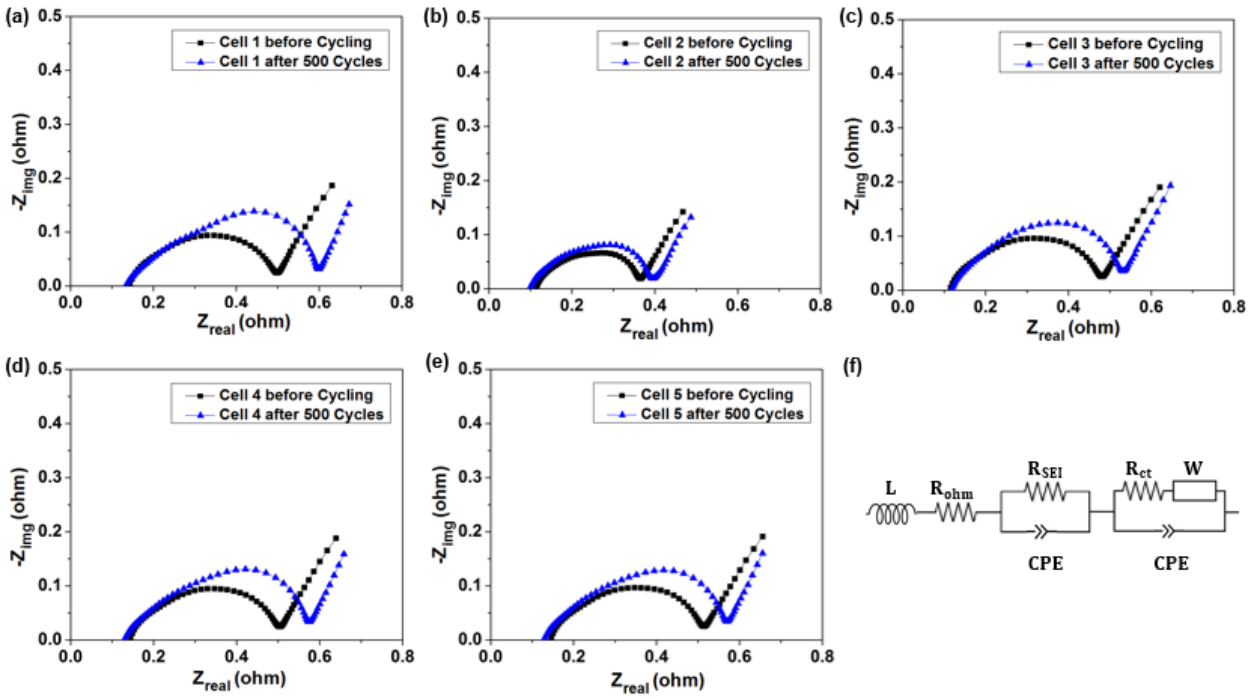

Figure 5.8. Comparison of electrochemical impedance spectra of lithium ion batteries before and after 500 cycles, (a): cell 1, (b): cell 2, (c): cell 3, (d): cell 4, (e): cell 5.

In the Nyquist plots, the intersection on the Z_{real} axis represents the ohmic resistance R_{ohm}. The first semicircle in the high frequency domain represents the surface film resistance R_{SEI} and the second semicircle in the low frequency domain represents the charge transfer resistance R_{ct} (Shim, Nam, Kim, Kim, & Moon, 2007; Song & Bazant, 2012). It can be found from Fig. 5.8 that R_{ohm} remains almost as constant for all five LIBs. Thus there is no obvious degradation in the components that are only related with the DC process in EIS analysis, including current collector, connection tab, etc. (W. Choi et al., 2020). The diameter of both semicircles increase over cycling, especially for the second semicircle at the low frequency domain. This indicates that both R_{ct} and R_{SEI} increase over cycling, especially R_{ct}. One of the possible reasons for the R_{ct} increase is cobalt dissolution and formation of Co_3O_4 from the aging of LIBs (Nara et al., 2016). This is also reflected in the Raman spectroscopy analysis. In Fig. 5.6 (d3), there is evidence of a Raman peak at around 690 cm^{-1}, which is related with Co_3O_4 (Hadjiev, Iliev, & Vergilov, 1988). Co_3O_4 is commonly observed in LIBs with polyvinylidene fluoride binder (Markevich, Salitra, & Aurbach, 2005) and the aging of LIBs promotes the cobalt dissolution and generation of Co_3O_4 on the surface of the LCO electrode (Nara et al., 2016). Further discussion on the aging mechanism requires quantitative

comparison of EIS results from LIBs with different dynamic and cycling history as well as detailed electrode structure evaluation, which is not in the scope of this work.

5.7 Supplementary Tests with the Dynamic Aging Testing Platform and Sensor Network

To verify the measuring capability of the dynamic aging testing platform and the sensor network, similar testing procedure was applied to another type of soft pack Li-ion pouch cell manufactured by Ranata Batteries. Details on the LIBs used for the supplementary tests are provided in Table 5.6.

Table 5.6. Specification of Lithium-ion batteries used in the supplementary tests.

Battery dimension	42.5 mm (l)*25.7 mm (w)*6.5 mm (h)	Separator material	Polypropylene
Battery weight	10.0 g	Separator dimension	780 mm (l)*35 mm (w)
Rated capacity (at 0.2C rate)	500 mAh	Separator thickness	15 μm
Anode active material	Graphite	Cathode active material	$LiCoO_2$
Anode current collector material	Copper	Cathode current collector material	Aluminum
Anode length	347 mm double sides	Cathode length	317 mm double sides
Anode width	33 mm	Cathode width	32 mm
Anode coating thickness (single side)	85 μm	Cathode coating thickness (single side)	65 μm
Anode current collector thickness	20 μm	Cathode current collector thickness	20 μm

In the supplementary tests, three LIBs (cell S1, S2 and S3) were analyzed. Two cells (cell S1 and S2) were connected in parallel to form a 2-cell pack. Same experimental setup, sensor network configuration and data acquisition system arrangement mentioned in the method section were adopted. Cell S1, S2 and S3 completed 200 cycles under continuous vibration specified in the NAVSEA 9310 standard, and the manufacturer specified maximum allowable current of 600 mA was applied for the constant current cycling. One impact test was applied between the first and second group of 100 cycles and the impacting velocity was calculated using equation (5.1). A summary of these experiments with the number of cells, environments and cycles is provided in Table 5.7.

Table 5.7. Summary of proposed dynamic aging testing conditions in the supplementary tests.

Cell No.	Connection type	Vibration	Impact	Cycling current	Charging/ discharging method	Total cycles
S1 and S2	Parallel connection	Sinusoidal wave, 18 Hz, 1g acceleration	150 g equivalent acceleration, after 100 cycles	600 mA	Constant current	200
S3	-	Sinusoidal wave, 18 Hz, 1g acceleration	150 g equivalent acceleration, after 100 cycles	600 mA	Constant current	200

In Fig. 5.9, the capacity of LIBs analyzed in the supplementary tests are presented. The observation is similar as for cell 1-5, except that there is no capacity increase over the first 100 cycles for cell S1, S2 and S3, which might be related with the factory cycling tests applied to this type of LIBs.

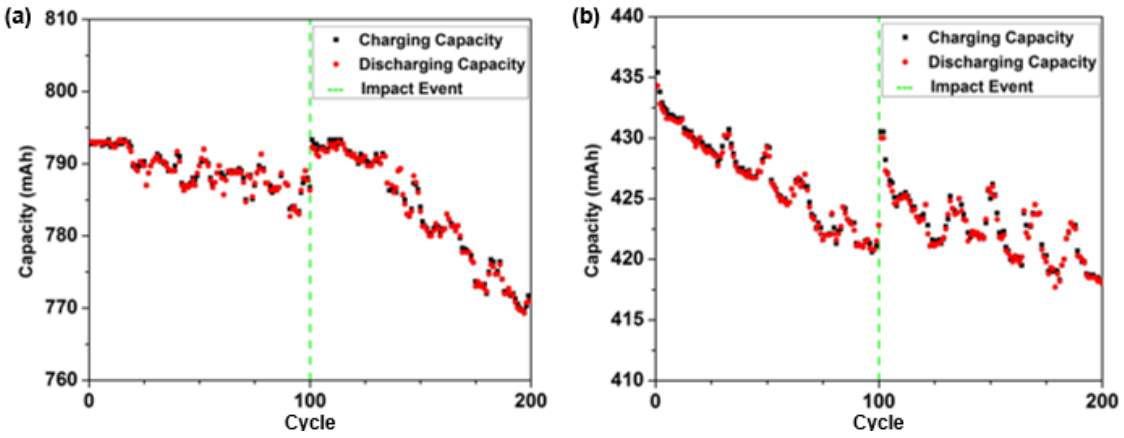

Figure 5.9. (a): Capacity of a two-cell pack (cell S1 and S2) under in-service vibration and impact; (b): Capacity of a single cell (cell S3) under in-service vibration and impact.

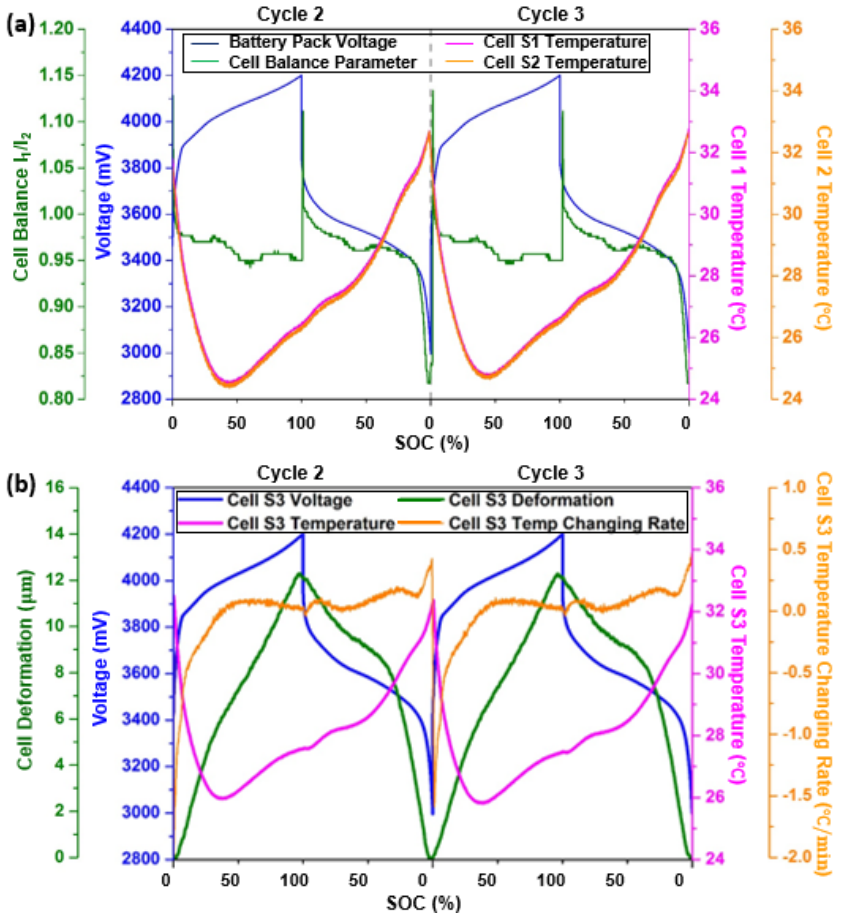

Figure 5.10. Voltage, temperature, temperature changing rate, deformation and cell balance parameter (I_1/I_2) in two consecutive cycles of (a): 2-cell pack (cell S1 and S2), (b): single cell (cell S3).

Similar to cell 1-5, cell S1-S3 present maximum temperature at the end of discharge and peak in cell deformation at the end of charge. Thus it can be concluded that for soft pack LIBs with LCO and graphite electrodes, the risk of temperature rise related failure is highest at the end of discharge, while the risk of stress accumulation related failure is highest at the end of charge.

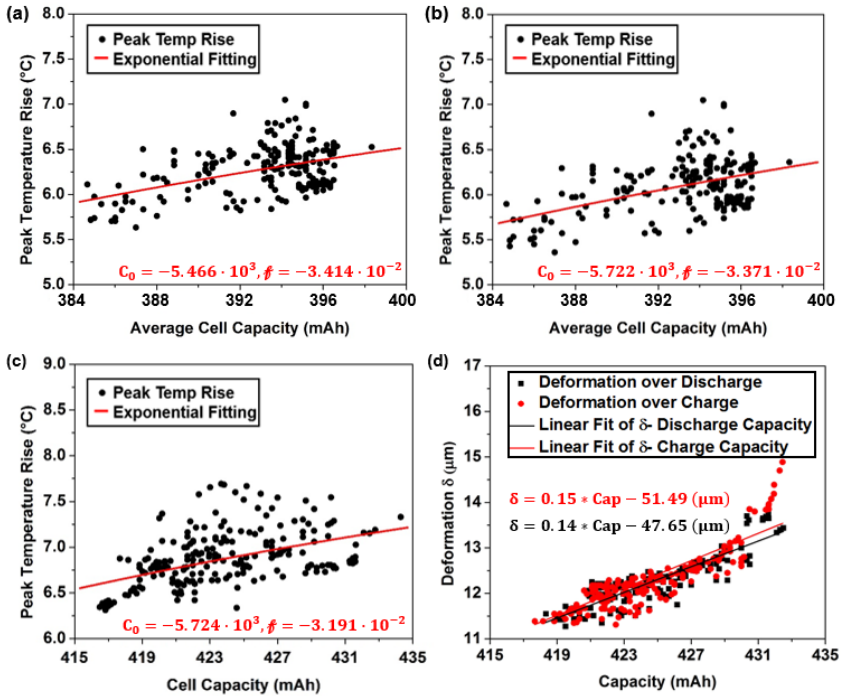

Figure 5.11. Relation between maximum temperature increase and capacity of (a): cell S1, (b): cell S2 and (c): cell S3. (d): Relation between maximum deformation and capacity of cell S3.

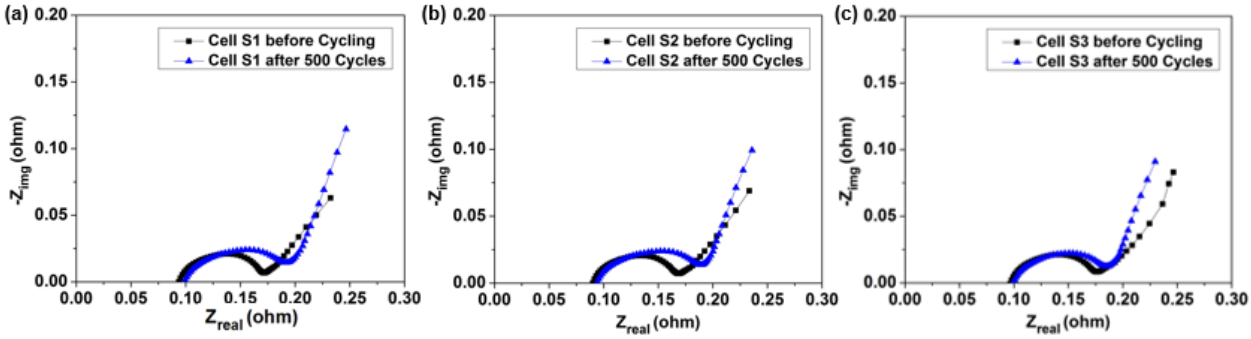

Figure 5.12. Comparison of electrochemical impedance spectra of lithium ion batteries in supplementary test before and after 200 cycles, (a): cell S1, (b): cell S2, (c): cell S3.

From Fig. 5.11 it can be found that equation (5.6) and (5.7) can be used for the description of the temperature increase and cell deformation of both types of LIBs analyzed in this work as they have the same electrode material.The observation in EIS comparison of cell S1-S3 before and after the dynamic aging test is similar to that of cell 1-5. There is no obvious increase in R_{ohm}, while R_{ct} and R_{SEI} both increased. A comparison of the measurements on cell 3 and cell S3 with the sensor network is presented in Table 5.8.

Table 5.8. Comparison of sensor network measurements on cell 3 and cell S3.

	Cell 3	Cell S3
Maximum capacity Cap_{max}	134.21 mAh	434.31 mAh
Ratio of capacity decrease at cycle 200 (with respect to Cap_{max})	5.64 %	3.76 %
Ratio of capacity recovery during first rest period at cycle 100 (with respect to Cap_{max})	3.12 %	1.66 %
Average capacity fading rate over cycle 101-200	0.058 mAh $cycle^{-1}$	0.120 mAh $cycle^{-1}$
Average temperature increasing rate over discharging cycles	0.04 °C min^{-1}	0.11 °C min^{-1}
Average thickness increasing rate over charging cycles	1.34 μm min^{-1}	0.28 μm min^{-1}

5.8 Conclusion

In this work, a sensor network consisting of a piezoelectric accelerometer, RTD, eddy current sensor, and shunt resistor was developed for in-operando LIB performance and safety monitoring in dynamic loading environments. LIB cycling was carried out with in-operando vibration and impact loads until reaching battery EOL. Battery performance analyses were

accomplished with conventional electrochemical methods and sensor measurements. The sensor measurements provided a complete characterization of battery performance during degradation from continuous dynamic loads. The changing trends of battery capacity, temperature rise, and deformation relations were established, which could be used to estimate the risks of LIB thermal failure and explosion over their service life under various vibrational loads. The sensor network also identified the critical periods of LIB thermal runaway and explosion, which could reduce system resources required for in-service LIB safety monitoring. With the relations between the LIB service cycle, battery capacity, temperature rise, and deformation established, the sensor network can be used for indirect analysis of LIB capacity based on service cycle, temperature, or deformation. As continuous electrochemical measurement is not required for this method, the integration related errors in LIB capacity can be avoided. This indirect capacity measurement method can also eliminate the need of continuous monitoring of the current of individual LIBs, which is challenging for large battery packs.

Performance of a LIB pack and single cells under in-service dynamic loads were compared. The effect of internal resistance and current difference on the battery temperature distribution was analyzed. It was found that heat generation of cells in a battery pack depends on both current distribution and SOC imbalance due to overpotential difference. It is challenging to locate a cell with the highest temperature rise in a battery pack during cycling with conventional electrochemical analysis. In this case, the RTDs can directly identify the critical cell that exhibits potential thermal hazard. In order to better analyze the temperature rise of individual cells in a battery pack, an energy balance based relation between LIB temperature and capacity based on RTD and shunt resistor measurements was established. This relation can provide an accurate description of temperature profile and help in evaluating the risk of thermal hazards throughout LIB service life.

By comparing the LIB deformation and theoretical thickness change from electrode deformation, the contribution of gas generation and electrode thickness change to LIB deformation was analyzed. It was noticed that gas accumulation and anode thickness increase were dominant for LIB deformation, which continued over the whole cycling life of LIBs. Theoretical gas generation analyses and eddy current sensor measurements helped to identify the critical periods with high gas generation rate. This information benefited the prevention of LIB explosion from stress accumulation. In order to support the observation in thickness change of the cell, Raman

spectroscopy analyses, SEM imaging and EIS analyses were performed. No severe damage to the electrodes was observed. Some changes in the Raman spectra reflected release of compressive residual stress in the graphite electrode and trace of Co_3O_4 in the LCO electrode.

With the temperature-capacity and deformation-capacity relations established, both battery temperature and deformation can be used for indirect analysis of LIB capacity and detection of critical capacity decrease. The effectiveness of RTD and eddy current sensor measurements for capacity degradation detection were compared in terms of information divergence. It was found that eddy current sensor measurements were more informational with limited groups of data. The RTD measurements became more informational when the number of cycles increased. As a result, sensors used to detect LIB capacity decrease should be switched during LIB service, and a sensor network with both sensors should be used for optimized results.

In summary, with the relations between parameters such as battery capacity, temperature rise, and deformation established, LIB performance and safety can be monitored using the presented sensor network measurements. The in-operando sensor measurements help to understand the aging mechanisms and origin of safety risks of LIBs. By applying the sensor network to LIBs in dynamic service environments, real-time detection and early warning of LIB thermal runaway is possible. In addition, the limitations in existing go/no go tests can be relaxed. Measurement of the effect of dynamic loading history on LIB performance degradation can improve the LIB safety monitoring significantly, especially for applications where environmental dynamic loadings are major safety concerns, such as electric vehicle, aircraft and portable energy storage systems, etc.

6. FUTURE WORK

The presented research has brought forth a better understanding of the dynamic aging and thermal runaway mechanisms of LIBs. A practical experiment approach was established to evaluate the effects of in-service dynamic loads on the performance of LIBs. By relating the electrode structure damage with the capacity decrease, temperature increase and deformation of the abused LIBs, an accurate description of the dynamic load related effects on the electrodes can be obtained. Some proposed future work in this area is summarized below:

(1). Obtain a comprehensive evaluation of the SOH of LIBs that experience combined in-service abuse conditions such as vibration and overcharge, impact and output power pulse, etc.

(2). Develop an effective numeric model to describe the electrode damage development under different in-service abusing conditions. Accurate real-time prediction of LIB performance degradation can be achieved with the application of this model and continuous monitoring of the battery service environment with the sensor network.

(3). Establish the accurate relation between the electrode temperature and battery surface temperature for different types of LIBs. Obtain the relation under various abusing conditions until reaching the EOL of LIBs. This can help to get a more accurate description of the electrode SOH with conventional temperature measurement of the battery surface (external sensor measurement).

(4). As the next step for proposed future work (3), combine the information collected by different sensors in the sensor network and further improve the efficacy and accuracy of the external sensor measurements. Achieve a reliable in-situ multidisciplinary LIB thermal runaway prediction and early prevention.

REFERENCES

Abaza, A., Ferrari, S., Wong, H. K., Lyness, C., Moore, A., Weaving, J., . . . Bhagat, R. (2018). Experimental study of internal and external short circuits of commercial automotive pouch lithium-ion cells. *Journal of Energy Storage, 16*, 211-217.

Abraham, K., & Jiang, Z. (1996). A polymer electrolyte-based rechargeable lithium/oxygen battery. *Journal of the Electrochemical Society, 143*(1), 1.

Adams, R. A., Li, B., Kazmi, J., Adams, T. E., Tomar, V., & Pol, V. G. (2018). Dynamic impact of LiCoO2 electrodes for Li-ion battery aging evaluation. *Electrochimica Acta, 292*, 586-593.

Adams, R. A., Syu, J.-M., Zhao, Y., Lo, C.-T., Varma, A., & Pol, V. G. (2017). Binder-free N-and O-rich carbon nanofiber anodes for long cycle life K-ion batteries. *ACS applied materials & interfaces, 9*(21), 17872-17881.

Ahmed, R., & Reifsnider, K. (2011). Study of influence of electrode geometry on impedance spectroscopy. *Int. J. Electrochem. Sci, 6*, 1159-1174.

Amatucci, G., Tarascon, J., & Klein, L. (1996). Cobalt dissolution in LiCoO2-based non-aqueous rechargeable batteries. *Solid State Ionics, 83*(1-2), 167-173.

Anastassakis, E., Pinczuk, A., Burstein, E., Pollak, F., & Cardona, M. (1993). Effect of static uniaxial stress on the Raman spectrum of silicon. *Solid State Communications, 88*(11-12), 1053-1058.

Aris, A. M., & Shabani, B. (2017). An Experimental Study of a Lithium Ion Cell Operation at Low Temperature Conditions. *Energy Procedia, 110*, 128-135.

Baccouche, I., Jemmali, S., Mlayah, A., Manai, B., & Amara, N. E. B. (2018). Implementation of an Improved Coulomb-Counting Algorithm Based on a Piecewise SOC-OCV Relationship for SOC Estimation of Li-IonBattery. *arXiv preprint arXiv:1803.10654*.

Baddour-Hadjean, R., & Pereira-Ramos, J.-P. (2010). Raman microspectrometry applied to the study of electrode materials for lithium batteries. *Chemical reviews, 110*(3), 1278-1319.

Balakrishnan, P., Ramesh, R., & Kumar, T. P. (2006). Safety mechanisms in lithium-ion batteries. *Journal of Power Sources, 155*(2), 401-414.

Bandhauer, T. M., Garimella, S., & Fuller, T. F. (2011). A critical review of thermal issues in lithium-ion batteries. *Journal of the Electrochemical Society, 158*(3), R1-R25.

Belov, D., & Yang, M.-H. (2008). Failure mechanism of Li-ion battery at overcharge conditions. *Journal of Solid State Electrochemistry, 12*(7-8), 885-894.

Bernardi, D., Pawlikowski, E., & Newman, J. (1985). A general energy balance for battery systems. *Journal of the electrochemical society, 132*(1), 5-12.

Białynicki-Birula, I., & Mycielski, J. (1975). Uncertainty relations for information entropy in wave mechanics. *Communications in Mathematical Physics, 44*(2), 129-132.

Birkl, C. R., Roberts, M. R., McTurk, E., Bruce, P. G., & Howey, D. A. (2017). Degradation diagnostics for lithium ion cells. *Journal of Power Sources, 341*, 373-386.

Bond, T., Zhou, J., & Cutler, J. (2017). Electrode stack geometry changes during gas evolution in pouch-cell-type lithium ion batteries. *Journal of The Electrochemical Society, 164*(1), A6158-A6162.

Boulet-Roblin, L., Borel, P., Sheptyakov, D., Tessier, C., Novak, P., & Villevieille, C. (2016). Operando neutron powder diffraction using cylindrical cell design: the case of LiNi0. 5Mn1. 5O4 vs graphite. *The Journal of Physical Chemistry C, 120*(31), 17268-17273.

Brand, M. J., Schuster, S. F., Bach, T., Fleder, E., Stelz, M., Gläser, S., . . . Jossen, A. (2015). Effects of vibrations and shocks on lithium-ion cells. *Journal of Power Sources, 288*, 62-69.

Bruen, T., Hooper, J. M., Marco, J., Gama, M., & Chouchelamane, G. H. (2016). Analysis of a battery management system (BMS) control strategy for vibration aged nickel manganese cobalt oxide (NMC) lithium-ion 18650 battery cells. *Energies, 9*(4), 255.

Bryden, T. S., Dimitrov, B., Hilton, G., de León, C. P., Bugryniec, P., Brown, S., . . . Cruden, A. (2018). Methodology to determine the heat capacity of lithium-ion cells. *Journal of Power Sources, 395*, 369-378.

Carter, R., Huhman, B., Love, C. T., & Zenyuk, I. V. (2018). X-ray computed tomography comparison of individual and parallel assembled commercial lithium iron phosphate batteries at end of life after high rate cycling. *Journal of Power Sources, 381*, 46-55.

Carter, R., & Love, C. T. (2018). Modulation of Lithium Plating in Li-Ion Batteries with External Thermal Gradient. *ACS applied materials & interfaces, 10*(31), 26328-26334.

Chen, S., Wan, C., & Wang, Y. (2005). Thermal analysis of lithium-ion batteries. *Journal of Power Sources, 140*(1), 111-124.

Chen, Z., Xiong, R., Lu, J., & Li, X. (2018). Temperature rise prediction of lithium-ion battery suffering external short circuit for all-climate electric vehicles application. *Applied Energy, 213*, 375-383.

Choi, J., Ryou, M.-H., Son, B., Song, J., Park, J.-K., Cho, K. Y., & Lee, Y. M. (2014). Improved high-temperature performance of lithium-ion batteries through use of a thermally stable co-polyimide-based cathode binder. *Journal of Power Sources, 252*, 138-143.

Choi, W., Shin, H.-C., Kim, J. M., Choi, J.-Y., & Yoon, W.-S. (2020). Modeling and Applications of Electrochemical Impedance Spectroscopy (EIS) for Lithium-ion Batteries. *Journal of Electrochemical Science and Technology, 11*(1), 1-13.

Command, N. S. S. (2010). Technical Manual for Navy Lithium Battery Safety Program Responsibilities and Procedures. Retrieved Oct 1st, 2019, from https://www.public.navy.mil/NAVSAFECEN/Documents/afloat/Surface/CS/Lithium_Batteries_Info/LithBatt_NAVSEA_TMS9310.pdf

Daniel H. Doughty, C. C. C. (2005). Electrical Energy Storage System Abuse Test Manual for Electric and Hybrid Electric Vehicle Applications Retrieved Oct 1st, 2019, from https://prod-ng.sandia.gov/techlib-noauth/access-control.cgi/2005/053123.pdf

del Corro, E., de la Roza, A. O., Taravillo, M., & Baonza, V. G. (2012). Raman modes and Grüneisen parameters of graphite under compressive biaxial stress. *Carbon, 50*(12), 4600-4606.

Doughty, D. H. (2010). SAE J2464 “EV & HEV rechargeable energy storage system (RESS) safety and abuse testing procedure”: SAE Technical Paper.

Dubarry, M., Truchot, C., & Liaw, B. Y. (2014). Cell degradation in commercial LiFePO4 cells with high-power and high-energy designs. *Journal of Power Sources, 258*, 408-419.

Dubey, D., & Tomar, V. (2008). Microstructure dependent dynamic fracture analyses of trabecular bone based on nascent bone atomistic simulations. *Mechanics Research Communications, 35*(1-2), 24-31.

Dubey, D. K., & Tomar, V. (2009). The effect of tensile and compressive loading on the hierarchical strength of idealized tropocollagen–hydroxyapatite biomaterials as a function of the chemical environment. *Journal of Physics: Condensed Matter, 21*(20), 205103.

Duh, Y.-S., Lin, K. H., & Kao, C.-S. (2018). Experimental investigation and visualization on thermal runaway of hard prismatic lithium-ion batteries used in smart phones. *Journal of thermal analysis and calorimetry, 132*(3), 1677-1692.

Elbeheiry, E., & Karnopp, D. (1996). Optimal control of vehicle random vibration with constrained suspension deflection. *Journal of sound and vibration, 189*(5), 547-564.

Ellis, L., Buteau, S., Hames, S. G., Thompson, L., Hall, D., & Dahn, J. (2018). A New Method for Determining the Concentration of Electrolyte Components in Lithium-Ion Cells, Using Fourier Transform Infrared Spectroscopy and Machine Learning. *Journal of the Electrochemical Society, 165*(2), A256-A262.

Europe, U. N. E. C. f. (2015). UN 38.3 Recommandations on the Transport of Dangerous Goods, Manual of Tests and Criteria. 6th edition. Retrieved Oct 1st, 2019, from https://www.unece.org/fileadmin/DAM/trans/danger/ST_SG_AC.10_11_Rev6_E_WEB_-With_corrections_from_Corr.1.pdf

Fear, C., Juarez-Robles, D., Jeevarajan, J. A., & Mukherjee, P. P. (2018). Elucidating Copper Dissolution Phenomenon in Li-Ion Cells under Overdischarge Extremes. *Journal of the Electrochemical Society, 165*(9), A1639-A1647.

Feng, X., Ouyang, M., Liu, X., Lu, L., Xia, Y., & He, X. (2018). Thermal runaway mechanism of lithium ion battery for electric vehicles: A review. *Energy Storage Materials, 10*, 246-267.

Finegan, D. P., Darcy, E., Keyser, M., Tjaden, B., Heenan, T. M., Jervis, R., . . . Magdysyuk, O. V. (2017). Characterising thermal runaway within lithium-ion cells by inducing and monitoring internal short circuits. *Energy & Environmental Science, 10*(6), 1377-1388.

Forgez, C., Do, D. V., Friedrich, G., Morcrette, M., & Delacourt, C. (2010). Thermal modeling of a cylindrical LiFePO4/graphite lithium-ion battery. *Journal of Power Sources, 195*(9), 2961-2968.

Frank, O., Tsoukleri, G., Riaz, I., Papagelis, K., Parthenios, J., Ferrari, A. C., . . . Galiotis, C. (2011). Development of a universal stress sensor for graphene and carbon fibres. *Nature communications, 2*(1), 1-7.

Fu, R., Xiao, M., & Choe, S.-Y. (2013). Modeling, validation and analysis of mechanical stress generation and dimension changes of a pouch type high power Li-ion battery. *Journal of Power Sources, 224*, 211-224.

Gan, M., & Tomar, V. (2014). An in situ platform for the investigation of Raman shift in micro-scale silicon structures as a function of mechanical stress and temperature increase. *Review of Scientific Instruments, 85*(1), 013902.

Gross, T., Giebeler, L., & Hess, C. (2013). Novel in situ cell for Raman diagnostics of lithium-ion batteries. *Review of Scientific Instruments, 84*(7), 073109.

Guo, R., Lu, L., Ouyang, M., & Feng, X. (2016). Mechanism of the entire overdischarge process and overdischarge-induced internal short circuit in lithium-ion batteries. *Scientific reports, 6*, 30248.

Hadjiev, V., Iliev, M., & Vergilov, I. (1988). The raman spectra of Co3O4. *Journal of Physics C: Solid State Physics, 21*(7), L199.

Han, F., Westover, A. S., Yue, J., Fan, X., Wang, F., Chi, M., . . . Wang, C. (2019). High electronic conductivity as the origin of lithium dendrite formation within solid electrolytes. *Nature Energy*, 1.

Han, X., Ouyang, M., Lu, L., Li, J., Zheng, Y., & Li, Z. (2014). A comparative study of commercial lithium ion battery cycle life in electrical vehicle: Aging mechanism identification. *Journal of Power Sources, 251*, 38-54.

Hatchard, T., MacNeil, D., Basu, A., & Dahn, J. (2001). Thermal model of cylindrical and prismatic lithium-ion cells. *Journal of the Electrochemical Society, 148*(7), A755-A761.

Hausbrand, R., Cherkashinin, G., Ehrenberg, H., Gröting, M., Albe, K., Hess, C., & Jaegermann, W. (2015). Fundamental degradation mechanisms of layered oxide Li-ion battery cathode materials: Methodology, insights and novel approaches. *Materials Science and Engineering: B, 192*, 3-25.

Ho, S.-W., & Yeung, R. W. (2010). On information divergence measures and a unified typicality. *IEEE Transactions on Information Theory, 56*(12), 5893-5905.

Hong, J. S., Maleki, H., Al Hallaj, S., Redey, L., & Selman, J. (1998). Electrochemical-calorimetric studies of lithium-ion cells. *Journal of the Electrochemical Society, 145*(5), 1489.

Hooper, J., Marco, J., Chouchelamane, G., & Lyness, C. (2016). Vibration durability testing of nickel manganese cobalt oxide (NMC) lithium-ion 18,650 battery cells. *Energies, 9*(1), 52.

Hooper, J. M., & Marco, J. (2014). Characterising the in-vehicle vibration inputs to the high voltage battery of an electric vehicle. *Journal of Power Sources, 245*, 510-519.

Inaba, M., Iriyama, Y., Ogumi, Z., Todzuka, Y., & Tasaka, A. (1997). Raman study of layered rock-salt LiCoO2 and its electrochemical lithium deintercalation. *Journal of Raman spectroscopy, 28*(8), 613-617.

Inaba, M., Yoshida, H., Ogumi, Z., Abe, T., Mizutani, Y., & Asano, M. (1995). In situ Raman study on electrochemical Li intercalation into graphite. *Journal of the Electrochemical Society, 142*(1), 20.

International, S. o. A. E. (2013). SAE J2380 Vibration Testing of Electric Vehicle Batteries. from https://www.sae.org/standards/content/j2380_200903/

Iqbal, N., & Lee, S. (2018). Mechanical failure analysis of graphite anode particles with PVDF binders in Li-ion batteries. *Journal of the Electrochemical Society, 165*(9), A1961.

Jeon, D. H., & Baek, S. M. (2011). Thermal modeling of cylindrical lithium ion battery during discharge cycle. *Energy Conversion and Management, 52*(8-9), 2973-2981.

Jones, R. M. (1977). Stress-strain relations for materials with different moduli in tension and compression. *AIAA Journal, 15*(1), 16-23.

Juarez-Robles, D., Chen, C.-F., Barsukov, Y., & Mukherjee, P. P. (2017). Impedance evolution characteristics in lithium-ion batteries. *Journal of the Electrochemical Society, 164*(4), A837-A847.

Jurng, S., Brown, Z. L., Kim, J., & Lucht, B. L. (2018). Effect of electrolyte on the nanostructure of the solid electrolyte interphase (SEI) and performance of lithium metal anodes. *Energy & Environmental Science, 11*(9), 2600-2608.

Kallfaß, C., Hoch, C., Hilger, A., & Manke, I. (2012). *Short-circuit and overcharge behaviour of some lithium ion batteries.* Paper presented at the International Multi-Conference on Systems, Signals & Devices.

Kang, Y., Qiu, Y., Lei, Z., & Hu, M. (2005). An application of Raman spectroscopy on the measurement of residual stress in porous silicon. *Optics and lasers in engineering, 43*(8), 847-855.

Kawaji, H., Takematsu, M., Tojo, T., Atake, T., Hirano, A., & Kanno, R. (2002). Low temperature heat capacity and thermodynamic functions of LiCoO 2. *Journal of thermal analysis and calorimetry, 68*(3), 833-839.

Keil, P., Rumpf, K., & Jossen, A. (2013). *Thermal impedance spectroscopy for Li-ion batteries with an IR temperature sensor system.* Paper presented at the 2013 World Electric Vehicle Symposium and Exhibition (EVS27).

Kermani, G., & Sahraei, E. (2017). Characterization and modeling of the mechanical properties of lithium-ion batteries. *Energies, 10*(11), 1730.

Ketterer, B., Vasilchina, H., Ulrich, S., Stueber, M., Leiste, H., Adelhelm, C., . . . Schimmel, T. (2009). Magnetron Sputtered Thin Film Cathode Materials For Lithium-Ion Batteries In The System Li–Co–O *Nanostructured Materials for Advanced Technological Applications* (pp. 405-409): Springer.

Kim, G.-H., Pesaran, A., & Spotnitz, R. (2007). A three-dimensional thermal abuse model for lithium-ion cells. *Journal of Power Sources, 170*(2), 476-489.

Kim, H. (2009). *Effects of Mechanical Stresses on Lithium Ion Batteries.*

Kim, Y. J., Cho, J., Kim, T.-J., & Park, B. (2003). Suppression of cobalt dissolution from the LiCoO2 cathodes with various metal-oxide coatings. *Journal of the Electrochemical Society, 150*(12), A1723.

Kisters, T., Sahraei, E., & Wierzbicki, T. (2017). Dynamic impact tests on lithium-ion cells. *International Journal of Impact Engineering, 108*, 205-216.

Kitagawa, T., Yabuki, K., & Young, R. (2001). An investigation into the relationship between processing, structure and properties for high-modulus PBO fibres. Part 1. Raman band shifts and broadening in tension and compression. *Polymer, 42*(5), 2101-2112.

Kizilel, R., Sabbah, R., Selman, J. R., & Al-Hallaj, S. (2009). An alternative cooling system to enhance the safety of Li-ion battery packs. *Journal of Power Sources, 194*(2), 1105-1112.

Kolly, J. M., Panagiotou, J., & Czech, B. (2013). The investigation of a lithium-ion battery fire onboard a Boeing 787 by the US National Transportation safety board. *Safety Research Corporation of America: Dothan, AL, USA*, 1-18.

Kumai, K., Miyashiro, H., Kobayashi, Y., Takei, K., & Ishikawa, R. (1999). Gas generation mechanism due to electrolyte decomposition in commercial lithium-ion cell. *Journal of Power Sources, 81*, 715-719.

Lagadec, M. F., Zahn, R., & Wood, V. (2018). Characterization and performance evaluation of lithium-ion battery separators. *Nature Energy*, 1.

Larsson, F., & Mellander, B.-E. (2014). Abuse by external heating, overcharge and short circuiting of commercial lithium-ion battery cells. *Journal of the Electrochemical Society, 161*(10), A1611.

Lee, B. H., & Kim, S. W. (2002). Development of battery management system for nickel–metal hydride batteries in electric vehicle applications. *Journal of Power Sources, 109*(1), 1-10.

Lee, J., Urban, A., Li, X., Su, D., Hautier, G., & Ceder, G. (2014). Unlocking the potential of cation-disordered oxides for rechargeable lithium batteries. *Science, 343*(6170), 519-522.

Lee, S.-H., You, H.-G., Han, K.-S., Kim, J., Jung, I.-H., & Song, J.-H. (2014). A new approach to surface properties of solid electrolyte interphase on a graphite negative electrode. *Journal of Power Sources, 247*, 307-313.

Lee, S.-M., Kim, J.-Y., & Byeon, J.-W. (2018). Failure Analysis of Short-Circuited Lithium-Ion Battery with Nickel-Manganese-Cobalt/Graphite Electrode. *Journal of nanoscience and nanotechnology, 18*(9), 6427-6430.

Leising, R. A., Palazzo, M. J., Takeuchi, E. S., & Takeuchi, K. J. (2001a). Abuse testing of lithium-ion batteries: Characterization of the overcharge reaction of licoo2/graphite cells. *Journal of the Electrochemical Society, 148*(8), A838-A844.

Leising, R. A., Palazzo, M. J., Takeuchi, E. S., & Takeuchi, K. J. (2001b). A study of the overcharge reaction of lithium-ion batteries. *Journal of Power Sources, 97*, 681-683.

Li, B., Adams, R. A., Kazmi, J., Dhiman, A., Adams, T. E., Pol, V. G., & Tomar, V. (2018). Investigation of Response of LiCoO 2 Cathode to Dynamic Impact Using Raman Imaging-Based Analyses. *JOM, 70*(8), 1423-1429.

Li, B., Parekh, M. H., Adams, R. A., Adams, T. E., Love, C. T., Pol, V. G., & Tomar, V. (2019). Lithium-ion Battery thermal Safety by early internal Detection, prediction and prevention. *Scientific reports, 9*(1), 1-11.

Li, W., Reimers, J., & Dahn, J. (1994). Lattice-gas-model approach to understanding the structures of lithium transition-metal oxides LiM O 2. *Physical Review B, 49*(2), 826.

Liao, X., Ma, C., Peng, X., Garg, A., & Bao, N. (2019). Temperature Distribution Optimization of an Air-Cooling Lithium-Ion Battery Pack in Electric Vehicles Based on the Response Surface Method. *Journal of Electrochemical Energy Conversion and Storage, 16*(4).

Lide, D. R. (1995). *CRC handbook of chemistry and physics: a ready-reference book of chemical and physical data*. Boca Raton, FL: CRC press.

Lin, X., Wang, W., Li, B., Miao, J., & Liu, Y. (2017). *Research into Thermal Response Time Fault Diagnosis of Temperature Sensor in High-Speed EMU.* Paper presented at the International Conference on Electrical and Information Technologies for Rail Transportation.

Liu, B., Jia, Y., Li, J., Yin, S., Yuan, C., Hu, Z., . . . Xu, J. (2018). Safety issues caused by internal short circuits in lithium-ion batteries. *Journal of Materials Chemistry A, 6*(43), 21475-21484.

Liu, B., Yin, S., & Xu, J. (2016). Integrated computation model of lithium-ion battery subject to nail penetration. *Applied Energy, 183*, 278-289.

Liu, D., Wang, Y., Xie, Y., He, L., Chen, J., Wu, K., . . . Gao, Y. (2013). On the stress characteristics of graphite anode in commercial pouch lithium-ion battery. *Journal of Power Sources, 232*, 29-33.

Liu, G., Ouyang, M., Lu, L., Li, J., & Han, X. (2014). Analysis of the heat generation of lithium-ion battery during charging and discharging considering different influencing factors. *Journal of thermal analysis and calorimetry, 116*(2), 1001-1010.

Liu, W., Jia, Z., Luo, Y., Xie, W., & Deng, T. (2019). Experimental investigation on thermal management of cylindrical Li-ion battery pack based on vapor chamber combined with fin structure. *Applied Thermal Engineering, 162*, 114272.

Logan, E., Tonita, E. M., Gering, K., Li, J., Ma, X., Beaulieu, L., & Dahn, J. (2018). A study of the physical properties of Li-Ion battery electrolytes containing esters. *Journal of the Electrochemical Society, 165*(2), A21-A30.

Love, C. T., Baturina, O. A., & Swider-Lyons, K. E. (2015). Observation of lithium dendrites at ambient temperature and below. *ECS Electrochemistry Letters, 4*(2), A24-A27.

Love, C. T., Virji, M. B., Rocheleau, R. E., & Swider-Lyons, K. E. (2014). State-of-health monitoring of 18650 4S packs with a single-point impedance diagnostic. *Journal of Power Sources, 266*, 512-519.

Mahajan, S. R., & Rajopadhye, R. D. (2013). Transportation noise and vibration sources, prediction, and control. *International Journal of Soft Computing and Engineering, 3*(5), 2231-2307.

Manev, V., Naidenov, I., Puresheva, B., & Pistoia, G. (1995). Effect of electrode porosity on the performance of natural Brazilian graphite electrodes. *Journal of Power Sources, 57*(1-2), 133-136.

Markevich, E., Salitra, G., & Aurbach, D. (2005). Influence of the PVdF binder on the stability of LiCoO2 electrodes. *Electrochemistry communications, 7*(12), 1298-1304.

Martiny, N. (2018). *Temperature Inhomogeneity in Lithium Ion Pouch Cells.* Technische Universität München.

Mejia-Rodriguez, G., Renaud, J. E., & Tomar, V. (2008). A variable fidelity model management framework for designing multiphase materials. *Journal of Mechanical Design, 130*(9), 091702 (091713 pages).

Mejía-Rodríguez, G., Renaud, J. E., & Tomar, V. (2008). A Variable Fidelity Model Management Framework for Designing Multiphase Materials. *Journal of Mechanical Design, 130*(9). doi: 10.1115/1.2965361

Mistry, A. N., Palle, H. R., & Mukherjee, P. P. (2019). In operando thermal signature probe for lithium-ion batteries. *Applied Physics Letters, 114*(2), 023901.

Murashko, K. A., Mityakov, A. V., Pyrhönen, J., Mityakov, V. Y., & Sapozhnikov, S. (2014). Thermal parameters determination of battery cells by local heat flux measurements. *Journal of Power Sources, 271*, 48-54.

Nara, H., Morita, K., Yokoshima, T., Mukoyama, D., Momma, T., & Osaka, T. (2016). Electrochemical impedance spectroscopy analysis with a symmetric cell for LiCoO2 cathode degradation correlated with Co dissolution. *AIMS Materials Science, 3*(2), 448-459.

National Transportation Safety Board. (2018a). Car with Automated Vehicle Controls Crashes into Roadway Barrier. Retrieved August 10, 2018, from https://www.ntsb.gov/investigations/Pages/HWY18FH011.aspx

National Transportation Safety Board. (2018b). Collision with Postcrash Fire Involving an Electric Passenger Vehicle. Retrieved August 10, 2018, from https://www.ntsb.gov/investigations/Pages/HWY18FH013.aspx

Naval Ordnance Safety and Security Activity. (2010). NAVSEA S9310-AQ-SAF-010 Technical Manual for Navy Lithium Battery Safety Program Responsibilities and Procedures, 2nd Revision. Retrieved April 10, 2018, from http://www.public.navy.mil/NAVSAFECEN/Documents/afloat/Surface/CS/Lithium_Batteries_Info/LithBatt_NAVSEA_TMS9310.pdf. Accessed 10 April 2017

Novais, S., Nascimento, M., Grande, L., Domingues, M., Antunes, P., Alberto, N., . . . Kim, G. (2016). Internal and external temperature monitoring of a Li-ion battery with fiber Bragg grating sensors. *Sensors, 16*(9), 1394.

Ohsaki, T., Kishi, T., Kuboki, T., Takami, N., Shimura, N., Sato, Y., . . . Satoh, A. (2005). Overcharge reaction of lithium-ion batteries. *Journal of Power Sources, 146*(1-2), 97-100.

Orendorff, C. J., Roth, E. P., & Nagasubramanian, G. (2011). Experimental triggers for internal short circuits in lithium-ion cells. *Journal of Power Sources, 196*(15), 6554-6558.

Peng, P., & Jiang, F. (2016). Thermal safety of lithium-ion batteries with various cathode materials: A numerical study. *International Journal of Heat and Mass Transfer, 103*, 1008-1016.

Piller, S., Perrin, M., & Jossen, A. (2001). Methods for state-of-charge determination and their applications. *Journal of Power Sources, 96*(1), 113-120.

Pimenta, M., Dresselhaus, G., Dresselhaus, M. S., Cancado, L., Jorio, A., & Saito, R. (2007). Studying disorder in graphite-based systems by Raman spectroscopy. *Physical chemistry chemical physics, 9*(11), 1276-1290.

Ploehn, H. J., Ramadass, P., & White, R. E. (2004). Solvent diffusion model for aging of lithium-ion battery cells. *Journal of the Electrochemical Society, 151*(3), A456.

Prakash, C., Gunduz, I. E., Oskay, C., & Tomar, V. (2018). Effect of interface chemistry and strain rate on particle-matrix delamination in an energetic material. *Engineering Fracture Mechanics, 191*, 46-64.

Qu, T., Verma, D., Alucozai, M., & Tomar, V. (2015). Influence of interfacial interactions on deformation mechanism and interface viscosity in α-chitin–calcite interfaces. *Acta Biomaterialia, 25*, 325-338. doi: https://doi.org/10.1016/j.actbio.2015.06.034

Qu, T., Verma, D., Alucozai, M., & Tomar, V. (2015). Influence of interfacial interactions on deformation mechanism and interface viscosity in α-chitin–calcite interfaces. *Acta biomaterialia, 25*(325-338).

Rahani, E. K., & Shenoy, V. B. (2013). Role of plastic deformation of binder on stress evolution during charging and discharging in lithium-ion battery negative electrodes. *Journal of the Electrochemical Society, 160*(8), A1153.

Rao, L., & Newman, J. (1997). Heat-generation rate and general energy balance for insertion battery systems. *Journal of the Electrochemical Society, 144*(8), 2697-2704.

Reich, S., & Thomsen, C. (2004). Raman spectroscopy of graphite. *Philosophical Transactions of the Royal Society of London. Series A: Mathematical, Physical and Engineering Sciences, 362*(1824), 2271-2288.

Richard, M., & Dahn, J. (1999). Accelerating rate calorimetry study on the thermal stability of lithium intercalated graphite in electrolyte. I. Experimental. *Journal of the Electrochemical Society, 146*(6), 2068-2077.

Rodrigues, M.-T. F., Sayed, F. N., Gullapalli, H., & Ajayan, P. M. (2018). High-temperature solid electrolyte interphases (SEI) in graphite electrodes. *Journal of Power Sources, 381*, 107-115.

Saha, B., & Goebel, K. (2009). *Modeling Li-ion battery capacity depletion in a particle filtering framework.* Paper presented at the Proceedings of the annual conference of the prognostics and health management society.

Saito, Y., Takano, K., & Negishi, A. (2001). Thermal behaviors of lithium-ion cells during overcharge. *Journal of Power Sources, 97*, 693-696.

Sakata, H., Dresselhaus, G., Dresselhaus, M., & Endo, M. (1988). Effect of uniaxial stress on the Raman spectra of graphite fibers. *Journal of applied physics, 63*(8), 2769-2772.

Saw, L., Tay, A., & Zhang, L. W. (2015). *Thermal management of lithium-ion battery pack with liquid cooling.* Paper presented at the 2015 31st Thermal Measurement, Modeling & Management Symposium (SEMI-THERM).

Schweidler, S., de Biasi, L., Schiele, A., Hartmann, P., Brezesinski, T., & Janek, J. r. (2018). Volume changes of graphite anodes revisited: a combined operando X-ray diffraction and in situ pressure analysis study. *The Journal of Physical Chemistry C, 122*(16), 8829-8835.

Sethuraman, V. A., Hardwick, L. J., Srinivasan, V., & Kostecki, R. (2010). Surface structural disordering in graphite upon lithium intercalation/deintercalation. *Journal of Power Sources, 195*(11), 3655-3660.

Shim, E.-G., Nam, T.-H., Kim, J.-G., Kim, H.-S., & Moon, S.-I. (2007). Effect of vinyl acetate plus vinylene carbonate and vinyl ethylene carbonate plus biphenyl as electrolyte additives

on the electrochemical performance of Li-ion batteries. *Electrochimica acta, 53*(2), 650-656.
Slobodnik, B. A. (1979). SPH-4 helmet damage and head injury correlation. *Aerospace Medicine and Human Performance, 50*(2), 139-146.
Smith, A., Burns, J., & Dahn, J. (2010). A high precision study of the Coulombic efficiency of Li-ion batteries. *Electrochemical and Solid-State Letters, 13*(12), A177-A179.
Snyder, C., Apblett, C., Grillet, A., Beechem, T., & Duquette, D. (2016). Measuring Li+ inventory losses in LiCoO2/graphite cells using raman microscopy. *Journal of the Electrochemical Society, 163*(6), A1036.
Sole, C., Drewett, N. E., & Hardwick, L. J. (2014). In situ Raman study of lithium-ion intercalation into microcrystalline graphite. *Faraday Discussions, 172*, 223-237.
Somerville, L., Hooper, J. M., Marco, J., McGordon, A., Lyness, C., Walker, M., & Jennings, P. (2017). Impact of vibration on the surface film of lithium-ion cells. *Energies, 10*(6), 741.
Song, J., & Bazant, M. Z. (2012). Effects of nanoparticle geometry and size distribution on diffusion impedance of battery electrodes. *Journal of the Electrochemical Society, 160*(1), A15.
Spotnitz, R., & Franklin, J. (2003). Abuse behavior of high-power, lithium-ion cells. *Journal of Power Sources, 113*(1), 81-100.
Taheri, P., & Bahrami, M. (2012). Temperature rise in prismatic polymer lithium-ion batteries: An analytic approach. *SAE International Journal of Passenger Cars-Electronic and Electrical Systems, 5*(2012-01-0334), 164-176.
Thomas, K. E., & Newman, J. (2003). Thermal modeling of porous insertion electrodes. *Journal of the Electrochemical Society, 150*(2), A176.
Tintignac, S., Baddour-Hadjean, R., Pereira-Ramos, J.-P., & Salot, R. (2012). High performance sputtered LiCoO2 thin films obtained at a moderate annealing treatment combined to a bias effect. *Electrochimica acta, 60*, 121-129.
Tomar, V. (2008a). Analyses of the role of grain boundaries in mesoscale dynamic fracture resistance of SiC–Si_3N_4 intergranular nanocomposites. *Engineering Fracture Mechanics, 75*(15), 4501-4512.
Tomar, V. (2008). Analyses of the role of the second phase SiC particles in microstructure dependent fracture resistance variation of SiC-Si3N4 nanocomposites. *Modelling and Simulation in Materials Science and Engineering, 16*(3), 035001. doi: https://doi.org/10.1016/j.engfracmech.2008.12.013
Tomar, V. (2008b). Modeling of dynamic fracture and damage in two-dimensional trabecular bone microstructures using the cohesive finite element method. *J Biomech Eng, 130*(2), 021021. doi: 10.1115/1.2903434
Tomar, V. (2009). Insights into the effects of tensile and compressive loadings on microstructure dependent fracture of trabecular bone. *Engineering Fracture Mechanics, 76*(7), 884-897.
Tomar, V., Gan, M., & Kim, H. S. (2010). Atomistic analyses of the effect of temperature and morphology on mechanical strength of Si–C–N and Si–C–O nanocomposites. *Journal of the European Ceramic Society, 30*(11), 2223-2237.
Tomar, V., & Zhou, M. (2005). Deterministic and stochastic analyses of fracture processes in a brittle microstructure system. *Engineering fracture mechanics, 72*(12), 1920-1941.
Verma, D., & Tomar, V. (2015). An investigation into mechanical strength of exoskeleton of hydrothermal vent shrimp (Rimicaris exoculata) and shallow water shrimp (Pandalus platyceros) at elevated temperatures. *Materials Science and Engineering: C, 49*, 243-250.

Viswanathan, V. V., Choi, D., Wang, D., Xu, W., Towne, S., Williford, R. E., . . . Yang, Z. (2010). Effect of entropy change of lithium intercalation in cathodes and anodes on Li-ion battery thermal management. *Journal of Power Sources, 195*(11), 3720-3729.

Waag, W., Käbitz, S., & Sauer, D. U. (2013). Experimental investigation of the lithium-ion battery impedance characteristic at various conditions and aging states and its influence on the application. *Applied Energy, 102*, 885-897.

Wang, C.-Y., Zhang, G., Ge, S., Xu, T., Ji, Y., Yang, X.-G., & Leng, Y. (2016). Lithium-ion battery structure that self-heats at low temperatures. *Nature, 529*(7587), 515.

Wang, G.-y., Yu, H., & Yang, D. (2002). Decision table reduction based on conditional information entropy. *CHINESE JOURNAL OF COMPUTERS-CHINESE EDITION-, 25*(7), 759-766.

Wang, P., Zhang, X., Yang, L., Zhang, X., Yang, M., Chen, H., & Fang, D. (2016). Real-time monitoring of internal temperature evolution of the lithium-ion coin cell battery during the charge and discharge process. *Extreme Mechanics Letters, 9*, 459-466.

Wang, Q., Ping, P., Zhao, X., Chu, G., Sun, J., & Chen, C. (2012). Thermal runaway caused fire and explosion of lithium ion battery. *Journal of Power Sources, 208*, 210-224.

Wang, Q., Sun, J., Yao, X., & Chen, C. (2005). Thermal stability of LiPF6/EC+ DEC electrolyte with charged electrodes for lithium ion batteries. *Thermochimica Acta, 437*(1-2), 12-16.

Wang, S., Li, Y., Li, Y.-Z., Mao, Y., Zhang, Y., Guo, W., & Zhong, M. (2017). A forced gas cooling circle packaging with liquid cooling plate for the thermal management of Li-ion batteries under space environment. *Applied Thermal Engineering, 123*, 929-939.

Wang, X., Loa, I., Kunc, K., Syassen, K., & Amboage, M. (2005). Effect of pressure on the structural properties and Raman modes of LiCoO 2. *Physical Review B, 72*(22), 224102.

Williard, N., He, W., Hendricks, C., & Pecht, M. (2013). Lessons learned from the 787 Dreamliner issue on lithium-ion battery reliability. *Energies, 6*(9), 4682-4695.

Williard, N., He, W., Osterman, M., & Pecht, M. (2012). *Reliability and failure analysis of Lithium Ion batteries for electronic systems.* Paper presented at the 2012 13th International Conference on Electronic Packaging Technology & High Density Packaging.

Wu, B., Yufit, V., Marinescu, M., Offer, G. J., Martinez-Botas, R. F., & Brandon, N. P. (2013). Coupled thermal–electrochemical modelling of uneven heat generation in lithium-ion battery packs. *Journal of Power Sources, 243*, 544-554.

Wu, H., Zhuo, D., Kong, D., & Cui, Y. (2014). Improving battery safety by early detection of internal shorting with a bifunctional separator. *Nature communications, 5*, 5193.

Wu, L., & Zhang, J. (2015). Ab initio study of anisotropic mechanical properties of LiCoO2 during lithium intercalation and deintercalation process. *Journal of applied physics, 118*(22), 225101.

Wu, M.-S., Chiang, P.-C. J., Lin, J.-C., & Jan, Y.-S. (2004). Correlation between electrochemical characteristics and thermal stability of advanced lithium-ion batteries in abuse tests—short-circuit tests. *Electrochimica acta, 49*(11), 1803-1812.

Wu, M.-S., Liu, K., Wang, Y.-Y., & Wan, C.-C. (2002). Heat dissipation design for lithium-ion batteries. *Journal of Power Sources, 109*(1), 160-166.

Wu, W., Wang, S., Wu, W., Chen, K., Hong, S., & Lai, Y. (2019). A critical review of battery thermal performance and liquid based battery thermal management. *Energy conversion and management, 182*, 262-281.

Wu, X., Lv, S., & Chen, J. (2017). Determination of the optimum heat transfer coefficient and temperature rise analysis for a lithium-ion battery under the conditions of Harbin city bus driving cycles. *Energies, 10*(11), 1723.

Xia, Y., Wierzbicki, T., Sahraei, E., & Zhang, X. (2014). Damage of cells and battery packs due to ground impact. *Journal of Power Sources, 267*, 78-97.

Xiong, R., Ma, S., Li, H., Sun, F., & Li, J. (2020). Towards a Safer Battery Management System: A Critical Review on Diagnosis and Prognosis of Battery Short Circuit. *Iscience*, 101010.

Yang, H., Bang, H., Amine, K., & Prakash, J. (2004). Investigations of the exothermic reactions of natural graphite anode for Li-ion batteries during thermal runaway. *Journal of the Electrochemical Society, 152*(1), A73.

Yang, H., Bang, H., Amine, K., & Prakash, J. (2005). Investigations of the exothermic reactions of natural graphite anode for Li-ion batteries during thermal runaway. *Journal of the Electrochemical Society, 152*(1), A73-A79.

Yang, Q., Wang, H., Ding, X., Yang, X., & Wang, Y. (2015). One-pot synthesis of dimethyl carbonate from carbon dioxide, cyclohexene oxide, and methanol. *Research on Chemical Intermediates, 41*(7), 4101-4111.

Ye, J., Chen, H., Wang, Q., Huang, P., Sun, J., & Lo, S. (2016). Thermal behavior and failure mechanism of lithium ion cells during overcharge under adiabatic conditions. *Applied Energy, 182*, 464-474.

Yi, J., Kim, U. S., Shin, C. B., Han, T., & Park, S. (2013). Three-dimensional thermal modeling of a lithium-ion battery considering the combined effects of the electrical and thermal contact resistances between current collecting tab and lead wire. *Journal of the Electrochemical Society, 160*(3), A437-A443.

Yokoshima, T., Mukoyama, D., Maeda, F., Osaka, T., Takazawa, K., & Egusa, S. (2019). Operando Analysis of Thermal Runaway in Lithium Ion Battery during Nail-Penetration Test Using an X-ray Inspection System. *Journal of the Electrochemical Society, 166*(6), A1243-A1250.

Yokoyama, T., Nakai, K., & Futakawa, M. (2008). Compressive Stress-Strain Characteristics of Nuclear-Grade Graphite IG-11 Effects of Specimen Size and Strain Rate. *Transactions of the Atomic Energy Society of Japan, 7*(1), 66-73.

Yufit, V., Shearing, P., Hamilton, R., Lee, P., Wu, M., & Brandon, N. (2011). Investigation of lithium-ion polymer battery cell failure using X-ray computed tomography. *Electrochemistry Communications, 13*(6), 608-610.

Zhang, G., Cao, L., Ge, S., Wang, C.-Y., Shaffer, C. E., & Rahn, C. D. (2015). Reaction temperature sensing (RTS)-based control for Li-ion battery safety. *Scientific reports, 5*, 18237.

Zhang, M., Du, J., Liu, L., Stefanopoulou, A., Siegel, J., Lu, L., . . . Ouyang, M. (2017). Internal short circuit trigger method for lithium-ion battery based on shape memory alloy. *Journal of the Electrochemical Society, 164*(13), A3038-A3044.

Zhang, Q., & White, R. E. (2008). Capacity fade analysis of a lithium ion cell. *Journal of Power Sources, 179*(2), 793-798.

Zhang, S. S. (2014). Insight into the gassing problem of Li-ion battery. *Frontiers in Energy Research, 2*, 59.

Zhang, S. S., Xu, K., & Jow, T. (2006). Study of the charging process of a LiCoO2-based Li-ion battery. *Journal of Power Sources, 160*(2), 1349-1354.

Zhang, X., Chang, X., Shen, Y., & Xiang, Y. (2017). Electrochemical-electrical-thermal modeling of a pouch-type lithium ion battery: an application to optimize temperature distribution. *Journal of Energy Storage, 11*, 249-257.

Zhao, K., Pharr, M., Vlassak, J. J., & Suo, Z. (2010). Fracture of electrodes in lithium-ion batteries caused by fast charging. *Journal of Applied Physics, 108*(7), 073517.

Zhao, R., Liu, J., & Gu, J. (2016). Simulation and experimental study on lithium ion battery short circuit. *Applied Energy, 173*, 29-39.

Zheng, J., Xiao, J., Gu, M., Zuo, P., Wang, C., & Zhang, J.-G. (2014). Interface modifications by anion receptors for high energy lithium ion batteries. *Journal of Power Sources, 250*, 313-318.

Zhu, J., Zhang, X., Luo, H., & Sahraei, E. (2018). Investigation of the deformation mechanisms of lithium-ion battery components using in-situ micro tests. *Applied Energy, 224*, 251-266.

Zuo, P., & Zhao, Y.-P. (2016). Phase field modeling of lithium diffusion, finite deformation, stress evolution and crack propagation in lithium ion battery. *Extreme Mechanics Letters, 9*, 467-479.